

# Image contrast in mirror and low energy electron microscopy

---

Shane M Kennedy  
BA/BSc(Hons)



School of Physics, Monash University

16 September 2010

---

# Contents

<b>Contents</b>	<b>i</b>
<b>Abstract</b>	<b>v</b>
<b>General Declaration</b>	<b>vii</b>
<b>Acknowledgements</b>	<b>ix</b>
<b>1 Introduction and overview</b>	<b>1</b>
1.1 MEM, LEEM and PEEM	1
1.2 General research aim of the thesis	5
1.3 Understanding MEM image contrast	6
1.4 Understanding LEEM image contrast	8
1.5 Wave optical treatment of MEM image contrast	10
1.6 Application to PEEM image contrast	12
1.7 Overview of the thesis	12
<b>2 Laplacian image contrast in MEM</b>	<b>13</b>
2.1 Addendum for chromatic aberration, the inclusion of the magnetic objective lens effect	32
2.2 Addendum for parallel illumination	33
<b>3 Caustic imaging of gallium droplets using MEM</b>	<b>37</b>
<b>4 Wave optical treatment of surface step contrast in LEEM</b>	<b>65</b>
<b>5 Phase retrieval low energy electron microscopy</b>	<b>85</b>
5.1 Addendum for phase retrieval with unknown aberration coefficients	107
5.2 Addendum for the uniqueness of phase retrieval of step transitions	107
<b>6 Transition between short and long wavelength limits in quantum mechanical reflection from a linear potential</b>	<b>109</b>
<b>7 Phase sensitivity of slow electrons to interactions with weak potentials</b>	<b>125</b>

7.1 Addendum for spatial coherence and the sensitivity to a finite electron energy spread	136
<b>8 Conclusions and future work</b>	<b>137</b>
<b>Bibliography</b>	<b>139</b>

**Notice 1**

Under the Copyright Act 1968, this thesis must be used only under the normal conditions of scholarly fair dealing. In particular no results or conclusions should be extracted from it, nor should it be copied or closely paraphrased in whole or in part without the written consent of the author. Proper written acknowledgement should be made for any assistance obtained from this thesis.

**Notice 2**

I certify that I have made all reasonable efforts to secure copyright permissions for third-party content included in this thesis and have not knowingly added copyright content to my work without the owner's permission.



---

## Abstract

We develop several approaches to understand and interpret image contrast in mirror electron microscopy (MEM) and low energy electron microscopy (LEEM), with potential applications to photoemission electron microscopy (PEEM). We treat both the forward problem, of how surface features and properties create image contrast, and the inverse problem, of how we may infer quantitative information about surface features and properties from experimental MEM, LEEM and PEEM images.

The thesis begins with the development of the Laplacian imaging theory of MEM, whereby image contrast is understood as the second derivative of the surface topography, blurred slightly to account for the interaction of the electron beam with the electric field above the specimen, rather than the specimen surface itself. This intuitive method includes the effects of lens aberrations and can be rapidly inverted to recover the surface topography from experimental MEM images. For specimen surface variations that are outside the regime of the Laplacian imaging theory and other models, we develop a caustic imaging theory for MEM. This involves solving the electric field above the specimen and tracing a family or envelope of rays through the immersion lens. Where initially adjacent rays cross, caustics are created, and these strong image features may be used to recover three dimensional surface topography. Both the Laplacian imaging theory and the caustic imaging theory are successfully applied to experimental MEM data to obtain the surface topography.

As a complement to this ray-based treatment, we then develop a wave optical treatment of LEEM image contrast, adopting the complex transfer function methodology from transmission electron microscopy. This method includes spherical and chromatic aberration, and may be extended to include higher order aberrations for use in aberration corrected LEEM instruments. With knowledge of the complex transfer function, we then apply phase retrieval methods to simulated LEEM images, recovering the electron wave function and surface topography for a series of step terraces.

Finally, we consider a wave optical treatment of MEM, investigating the be-

haviour of the electron wave in the vicinity of the turn around region. This is extended to explore the application of MEM beyond specimen surfaces, and the feasibility of imaging very weak potentials, such as the ponderomotive potential experienced by an electron in a light field.

---

# General Declaration

## **Declaration for thesis based or partially based on jointly published or unpublished work**

In accordance with Monash University Doctorate Regulation 17/ Doctor of Philosophy and Master of Philosophy (MPhil) regulations the following declarations are made:

I hereby declare that this thesis contains no material which has been accepted for the award of any other degree or diploma at any university or equivalent institution and that, to the best of my knowledge and belief, this thesis contains no material previously published or written by another person, except where due reference is made in the text of the thesis.

This thesis includes five original papers published in peer reviewed journals and one as-yet unpublished manuscript accepted for publication. Five of the six full-length papers have myself as the first author. The core of the thesis is understanding and modelling image contrast in mirror electron microscopy and low energy electron microscopy. The ideas, development and writing up of all the papers in the thesis were the principal responsibility of myself, the candidate, my supervisors David Jesson and David Paganin, and the co-authors of the respective papers. The inclusion of co-authors reflects the fact that the work came from active collaboration between researchers and acknowledges input into team-based research. Each paper includes a specific declaration describing the relative contribution of each author. I have renumbered sections of submitted and published papers in order to generate a consistent presentation within the thesis.

In the case of chapters 2–7 my contribution was the following:

<b>Ch.</b>	<b>Publication title, publication status</b>	<b>Nature and extent of candidate's contribution</b>
2	Laplacian image contrast in mirror electron microscopy <i>Published</i>	Developed the model used in the paper, performed the image simulations, co-wrote the paper

<b>Ch.</b>	<b>Publication title, publication status</b>	<b>Nature and extent of candidate's contribution</b>
3	Caustic imaging of gallium droplets using mirror electron microscopy <i>Accepted</i>	Developed the model used in the paper, performed the image simulations, co-wrote the paper
4	Wave optical treatment of surface step contrast in low-energy electron microscopy <i>Published</i>	Significantly extended the initial model, performed the simulations and produced the images of the paper, co-wrote the paper
5	Phase retrieval low energy electron microscopy <i>Published</i>	Provided the parameters and model (i.e. the complex transfer function) for the forward problem, co-wrote and provided technical expertise
6	Transition between short and long wavelength limits in quantum mechanical reflection from a linear potential <i>Published</i>	Developed the model used in the paper, performed the image simulations, co-wrote the paper
7	Phase sensitivity of slow electrons to interactions with weak potentials <i>Published</i>	Developed the model used in the paper, performed the image simulations, co-wrote the paper

---

Shane M Kennedy

---

## Acknowledgements

I gratefully acknowledge the support and assistance of my supervisors David Jesson and David Paganin, whose patience, wisdom and inspiration have guided me throughout this research project and, I trust, beyond.

I acknowledge the assistance of Changxi Zheng and Wen-Xin Tang for their excellent experimental work and many useful discussions.

I acknowledge the work of Michael Morgan, Naomi Schofield, Andrew Smith and Peter Barker, who contributed to the articles comprising this thesis.

I acknowledge my fellow postgraduate students, in particular Gary Ruben and Shekhar Chandra, for their advice, expertise and sense of humour. I acknowledge the use of Gary Ruben's thesis template, thanks for the time saver Gary!

I acknowledge the support of the administration staff in the School of Physics, Faculty of Science and the Monash Research Graduate School, in particular Jean Pettigrew, who steered me through the minefield of paperwork.

I acknowledge financial assistance from the J. L. William Bequest and an Australian Postgraduate Award from the Australian Research Council.

Finally, I acknowledge the support and patience of my family, whose encouragement and love have made this project possible.

---

# Introduction and overview

## 1.1 MEM, LEEM and PEEM

Mirror electron microscopy (MEM), low energy electron microscopy (LEEM) and photoemission electron microscopy (PEEM) are a set of related techniques that investigate surface properties and phenomena. As indicated in Fig. 1.1, an electron beam is directed through an objective lens and focused onto a specimen surface. The specimen (typically a semiconductor wafer) forms the cathode of the electrostatic component of the objective lens (Bauer, 1962, 1985, 1994; Barnett and Nixon, 1967b; Luk'yanov et al., 1974; Bok, 1978), and is held at a negative potential so that the incident electrons lose kinetic energy as they approach the sample. In MEM, the specimen potential is slightly more negative than the electron source, so that the electron beam turns around just above the cathode surface. In LEEM, electrons interact with and are reflected from the specimen with very low energy (typically 1–100 eV). In PEEM, photoelectrons are instead emitted from the surface by illuminating the specimen with sufficiently high energy photons.

In the region close to the cathode, the electrons have very low energy and are highly sensitive to surface features and/or the electric field produced by the specimen (Bauer, 1994). Therefore LEEM and related techniques are capable of probing near-surface structure, surface properties and phenomena in the first few monolayers of a specimen, with an interaction depth of several nanometres (Bauer, 1994, 2007; Altman, 2010).

After interacting with the specimen surface and/or the electric field above the sample, the electron beam is re-accelerated away from the specimen and exits the objective lens. The beam is then magnetically deflected and refocused onto an imaging screen. A LEEM may combine a number of spec-

troscopic techniques, and can display the diffraction pattern or a direct image of the specimen.

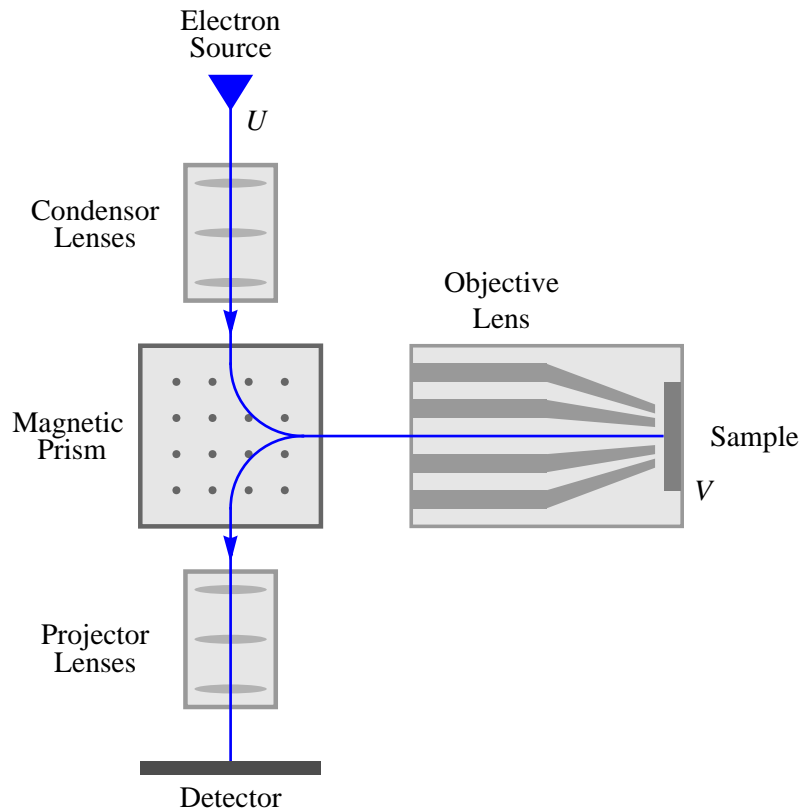


Figure 1.1: Schematic of a low energy electron microscope. Electrons are emitted from the source with energy  $U$  and directed towards the sample which comprises part of the objective lens. The returning electron beam is directed through the imaging system to a detector. Based on Bauer (1994); Phaneuf and Schmid (2003); Tromp et al. (2010).

One significant advantage of LEEM and associated techniques is that they offer a fast imaging rate and large field of view which make them suitable for studying dynamical effects in real time (Tromp and Reuter, 1993; Bauer, 1994; Phaneuf and Schmid, 2003; Bauer, 2007; Altman, 2010). Additionally, studies of surfaces often require an ultra high vacuum (UHV), which is practical to

achieve in LEEM (Bauer, 1994, 2007; Altman, 2010). LEEM images may be obtained from surfaces under a variety of conditions, such as in the presence of atom or ion flux and over a wide range of temperatures (Phaneuf and Schmid, 2003).

A LEEM instrument was first proposed by Bauer in the early 1960s (Bauer, 1962; Turner and Bauer, 1966). Godehardt (1995) discusses a brief history of mirror mode microscopy from early optics work in Germany in the 1930s. In the period after Bauer's first proposal MEM was actively studied and applied for some time (Barnett and Nixon, 1967b; Luk'yanov et al., 1974; Bok, 1978; Dupuy et al., 1984; Godehardt, 1995). Following the development of a new LEEM instrument by Telieps and Bauer (Bauer, 1985; Telieps and Bauer, 1985), the use of LEEM and related techniques has flourished, in tandem with advancements in instrumental design (Tromp and Reuter, 1991; Veneklasen, 1991; Bauer, 1994; Fink et al., 1997; Rempfer et al., 1997; Tromp et al., 1998; Wichtendahl et al., 1998; Schmidt et al., 2002; Schönhense and Spiecker, 2002; Hartel et al., 2003; Wan et al., 2004; Könenkamp et al., 2008; Schmidt et al., 2010; Tromp et al., 2010). A typical instrument includes the capabilities of LEEM, low energy electron diffraction (LEED), PEEM, and MEM, and allows MEM to work in a focused imaging mode rather than projecting onto a distant screen (Godehardt, 1995).

LEEM has been applied to studies of surfaces including mass-transport, evaporation, nucleation processes (Griffith and Engel, 1991; Bauer, 1994; Tanaka et al., 1997; McCarty et al., 2001; Yasue et al., 2001; Tromp and Hannon, 2002; Watanabe et al., 2004; Hibino and Watanabe, 2005; Kellogg and Bartelt, 2005; Bauer, 2007; Man et al., 2007b; Altman, 2010), the growth of nanostructures (Plass et al., 2001; Hannon et al., 2006; Man et al., 2006), understanding epitaxial growth (Bauer, 1991; Świąch et al., 1993; Theis et al., 1995), surface thermodynamics (Bartelt et al., 1994; Plass et al., 2001; Tromp and Hannon, 2002), phase transitions (Bauer, 1994; Hannon et al., 2001), morphological evolution (Altman et al., 1995; Tanaka et al., 1997; Ross et al., 1999; Kellogg and Bartelt, 2005), band structure (Altman, 2005, 2010) and the properties of thin films and surface features including facets (Telieps and Bauer, 1985; Telieps et al., 1987; Telieps and Bauer, 1988; Bauer, 1991; Altman et al., 2001; Tang et al., 2002; Yasue et al., 2002; Chung et al., 2003; Man et al., 2004, 2006; Bauer, 2007; Altman, 2010). Imaging magnetic phenomena is also possible by utilising a spin-polarized beam of electrons in spin-polarized LEEM or SPLEEM (Bauer, 1998; Duden and Bauer, 1998; Poppa et al., 2002; Phaneuf and Schmid, 2003; Bauer, 2007; Altman, 2010; Rougemaille and Schmid, 2010). LEED is routinely used to complement LEEM imaging inves-

tigations (Thayer et al., 2005; de la Figuera et al., 2006; Hannon et al., 2006; Man et al., 2007a; Sadowski et al., 2007), providing complementary reciprocal space information.

MEM has been applied to studying electric field contrast (Luk'yanov et al., 1974; Bok, 1978; Dupuy et al., 1984; Slezák et al., 2000; Shimakura et al., 2008; Nepijko and Schönhense, 2010), droplet surface dynamics (Hilner et al., 2009; Tersoff et al., 2009, 2010), surface magnetic fields (Barnett and Nixon, 1967b), and chemical processes at solid surfaces (Świąch et al., 1993; Ko and Joy, 2002). It has been used to measure electric field variations above the specimen surface caused by the surface topography (Tromp and Reuter, 1993; Bauer, 1998; Nepijko et al., 2001b; Speake and Trenkel, 2003) and/or variations in the electric potential of the specimen, which includes contact potentials, surface charges and varying conductivity (Barnett and Nixon, 1967a,b; Luk'yanov et al., 1974; Bok, 1978; Dupuy et al., 1984; Świąch et al., 1993; Nepijko and Schönhense, 2010).

Although PEEM is a useful and distinct technique in its own right (Griffith and Engel, 1991; Tromp and Reuter, 1993), we consider it here only in so far as many of the techniques discussed may be extended to understand PEEM image contrast. PEEM has been used to image chemical and surface potential contrast (Nepijko et al., 2001a; Günther et al., 2002; Smith et al., 2003; Morin et al., 2004; Tang et al., 2009), study droplet nucleation and morphology (Jesson et al., 2007; Tang et al., 2009) and element contrast (Rockenberger et al., 2002) along with magnetic applications (Wu et al., 2004; Finazzi et al., 2006; Nepijko et al., 2007).

LEEM and related techniques continue to develop and are being applied to new areas of research, including energy filtering, surface plasmons, band structure mapping and  $k$ -space imaging (Chelaru and Meyer zu Heringdorf, 2007; Krömker et al., 2008; Barrett et al., 2009; Meyer zu Heringdorf and Buckanie, 2010).

## 1.2 General research aim of the thesis

Along with the experimental development and application of MEM, LEEM and PEEM, there have been many attempts to explain how image contrast is produced. Particular emphasis has been placed on understanding the factors controlling the spatial resolution of the instrument (Shao and Crewe, 1989; Rempfer and Griffith, 1992; Rempfer, 1992; Bauer, 1994; Schmidt et al., 2010; Tromp et al., 2010).

The general aim of this research was to address the question of ‘how might we better understand the mechanisms that directly relate image contrast to surface features and properties?’, with a specific focus on MEM and LEEM. Answering this question involved two broad stages. The first was in understanding and quantifying the *forward problem*, whereby surface features and properties create image contrast in MEM and LEEM instruments. Emphasis was placed on developing image contrast models that produce qualitatively and quantitatively accurate simulations of experimental MEM and LEEM images from known surface specimens, whilst remaining as intuitive and accessible as possible, in order to facilitate rapid and practical interpretation and understanding of image contrast features.

The second stage was enabled by the first, in that understanding the forward problem allowed a meaningful investigation of the *inverse problem*, whereby surface features and properties may be inferred both qualitatively and quantitatively from experimental MEM and LEEM images. Beyond improving the understanding and interpretation of MEM and LEEM images via a firm grasp of the forward problem, developing the inverse problem empowers surface scientists to directly obtain information on the topography, potential and properties of a specimen surface from experimental images.

The remainder of the introduction establishes the context of the proceeding chapters, discussing the models and methods used to understand both the forward and inverse problems in MEM and LEEM.

### 1.3 Understanding MEM image contrast

In mirror electron microscopy, the electron beam interacts with the electric field above the specimen surface, and is sensitive to spatial and/or temporal variations in the electric field close to the surface. Such field variations result from the surface topography (Bauer, 1998; Nepijko et al., 2001b; Speake and Trenkel, 2003) and/or variations in the electric potential of the specimen, including contact potentials, surface charges and varying conductivity (Barnett and Nixon, 1967a,b; Luk'yanov et al., 1974; Bok, 1978; Świąch et al., 1993). The returning electron beam therefore contains information concerning the near-surface electric field, which has stimulated significant effort to interpret MEM image contrast and extract quantitative information of the field, and the underlying surface properties creating it. Although a variety of approaches have been employed, including some based on wave mechanics (Hermans and Petterson, 1970; Kennedy et al., 2006), most have been based on geometrical ray tracing techniques (Barnett and Nixon, 1967a; Sedov, 1970; Luk'yanov et al., 1974; Someya and Kobayashi, 1974; Bok, 1978; Rempfer and Griffith, 1992; Rempfer, 1992; Świąch et al., 1993; Godehardt, 1995). Building on this latter work, a geometrical theory has been developed which views MEM contrast as a transverse redistribution of electron current density on an imaging screen. This redistribution is due to shifts in electron trajectories following interaction with the electric field just above the specimen surface (Sedov, 1970; Dyukov et al., 1991; Nepijko and Sedov, 1997). This work, which has been used extensively to simulate MEM and PEEM contrast in a variety of situations (Nepijko et al., 2001a,b, 2003, 2007; Jesson et al., 2007; Tang et al., 2009; Nepijko and Schönhense, 2010), is here referred to as the geometrical theory of MEM contrast.

#### 1.3.1 Laplacian imaging theory (Paper 1)

An advantage of the geometrical theory of MEM contrast is that, for special geometries, the electron shifts can be calculated analytically which provides important insight into the mechanisms of contrast (Nepijko and Sedov, 1997; Nepijko et al., 2001a). However, there remained no simple and direct way of intuitively interpreting MEM contrast from a given general specimen. This is addressed in chapter 2, where we approximate the geometrical theory for slowly varying surface features and/or small objective lens defocus, which is applicable to a wide range of practical imaging situations. The resulting Laplacian imaging theory presents the intensity  $I$  as a function of defocus

$\Delta f$  and the transverse Laplacian of the surface topography  $\nabla_{\perp}^2 H$ ,

$$I \approx 1 - \Delta f \nabla_{\perp}^2 H \otimes B/4L_M, \quad (1.1)$$

which is blurred by convolving with the point-spread function  $B/4L_M$  that depends on  $x, y$  and turning distance  $\delta$ . Equation (1.1) gives an intuitive connection between surface features and image contrast, and can be used to rapidly interpret experimental images and recover the surface topography of the specimen. As an example, we have recovered the surface height profile of a trail in a GaAs surface left by a moving Ga droplet. A strong parallel exists between the Laplacian imaging theory and wave optical ‘out of focus’ contrast in transmission electron microscopy (TEM) (Cowley, 1995; Spence, 2003). This allows a number of extensions to be made to the intuitive method, such as including the effects of spherical and chromatic aberration as outlined in chapter 2.

### 1.3.2 Caustic imaging theory (Paper 2)

Laplacian imaging theory (chapter 2) can intuitively and rapidly interpret MEM image contrast for specimens with small and/or slowly varying surface features. Larger surface features and/or stronger variations, however, are capable of deflecting the electron trajectories so much that very strong image contrast is created, including caustic features (Berry, 1981; Nye, 1999). Such deflections typically violate the assumptions underlying previous approaches (Someya and Kobayashi, 1974; Godehardt, 1995; Nepijko and Sedov, 1997; Nepijko et al., 2001b; Kennedy et al., 2010; Nepijko and Schönhense, 2010), i.e. that the perturbed electron paths closely match the unperturbed paths. Other approaches such as Nepijko and Sedov (1997) and Nepijko et al. (2001a) may only be solved in specific analytical cases. Chapter 3 presents a general ray-based method of interpreting MEM image contrast, using a family or envelope of incident electron rays traced through a numerically solved electric field close to the specimen surface. Where initially adjacent ray trajectories cross a caustic feature is observed, which can be directly related to variations in the field above the surface. This allows for the understanding and interpretation of MEM image contrast in the presence of stronger field variations than has previously been possible.

The inverse problem, whereby specimen information is recovered directly from experimental images, is also facilitated by a caustic imaging theory. Chapter 3 discusses using key caustic features to recover three dimensional surface information. As an example, the dark central region produced in MEM images of Ga droplets at negative defocus is used to determine the

droplet contact angle. In the caustic imaging theory there is no single equation relating intensity and surface features that we may directly invert. But the capability for quantitative recovery of information using caustic imaging theory is shown in chapter 3 to be both possible and practical.

## **1.4 Understanding LEEM image contrast**

### **1.4.1 Wave optical treatment of LEEM (Paper 3)**

In LEEM, the electron beam reaches the surface of the specimen and scatters, returning with information relating to the surface (Telieps and Bauer, 1985; Bauer, 1994; Altman et al., 1998; Pang et al., 2009; Altman, 2010). Where the surface is crystalline, the elastically backscattered beam is concentrated into specific Bragg angles by diffraction, which may be exploited via a contrast aperture to image specific diffracted beams in LEEM (Bauer, 1994; Pang et al., 2009; Altman, 2010). Several models have been developed to explain image contrast and estimate spatial resolution in LEEM. This includes an early wave optical description of resolution (Shao and Crewe, 1989) and geometrical descriptions (Bauer, 1985; Rempfer and Griffith, 1992; Rempfer, 1992). Chung and Altman (1998) and Altman et al. (1998) first applied wave optical techniques to directly explain LEEM image contrast of surface steps, via the interference of Fresnel diffracted waves from adjacent terraces either side of the step. Aberrations in the electrostatic immersion lens and magnetic objective lens, and diffraction effects created by the contrast aperture, play a key role in determining resolution and image contrast for surface features close to the resolution limit (Bauer, 1985, 1994; Rempfer and Griffith, 1992; Rempfer, 1992; Pang et al., 2009; Tromp et al., 2010), but these were not fully implemented in the initial treatment of Chung and Altman (1998).

A general wave optical treatment of LEEM is able to incorporate lens aberrations and the contrast aperture effect in a natural way, and is therefore highly desirable. Such a treatment is developed in chapter 4 using a complex transfer function approach. Independently, a Fourier optics description of LEEM image contrast, incorporating the aberrations of the objective lens and the effect of the contrast aperture, was developed by Pang et al. (2009). Both methods apply techniques from transmission electron microscopy to describe LEEM imaging, and share the same essential principles and methods.

In chapter 4 the specimen surface is treated as a perfect mirror, so there is no change in the amplitude of the reflected electron wave function, and neither

multiple nor inelastic scattering, nor the quantum mechanical interaction of the electron with the band structure of the surface atoms is considered (Altman, 2010). Chapter 4 investigates only phase contrast LEEM images, e.g. due to surface steps or quantum size effects in thin films (Bauer, 1994; Altman et al., 1995, 1998; Chung and Altman, 1998; Altman, 2010) which form a pure phase object, i.e. a wave function with only transverse phase variation. Pang et al. (2009) likewise assume that the effects of multiple and inelastic scattering are negligible, but they apply the Fourier optics method to both amplitude contrast and phase contrast, where amplitude contrast is due, for example, to differing reflectivity of surface structures (Altman et al., 2001; Man et al., 2004; Pang et al., 2009; Altman, 2010). Whilst chapter 4 considers only phase contrast LEEM images, the methods described are also applicable to amplitude contrast. The complex transfer function method has a small advantage in its efficiency of calculation and straightforward application to two dimensional images.

As foreshadowed in chapter 4 and by Pang et al. (2009), with the recent development of aberration corrected LEEM instruments (Scherzer, 1947; Rose and Preikszas, 1992; Bauer, 1994; Fink et al., 1997; Rempfer et al., 1997; Tromp et al., 1998; Wichtendahl et al., 1998; Schmidt et al., 2002; Schönhense and Spiecker, 2002; Hartel et al., 2003; Wan et al., 2004; Könenkamp et al., 2008; Schmidt et al., 2010; Tromp et al., 2010), it has become necessary to include higher order aberration terms in order to understand and simulate LEEM image contrast. The complex transfer function method has very recently been expanded by Schramm et al. (2010) to include higher order aberration terms than in previous wave optical descriptions (Pang et al., 2009; Kennedy et al., 2009). The method also includes the resolution-limiting effects of the detector, which are more relevant with the absence of lower order aberrations, and rigorously calculates the aberration coefficients for the instrument designed and built by Tromp et al. (2010). Finally, Schramm et al. (2010) have adapted the complex transfer function formalism to PEEM, the primary distinguishing feature being the absence of spatial coherence in the electron wave in PEEM, as a result of the photoemission of electrons compared to a coherent incident electron beam in LEEM.

#### **1.4.2 Recovering specimen information from LEEM images (Paper 4)**

Chapter 5 introduces the application of phase retrieval methods to LEEM images, whereby knowledge of the complex transfer function including any

aberrations (via chapter 4 in this case but equally valid for the expanded transfer function of Schramm et al. (2010)) is used to retrieve the phase object that produced the LEEM image contrast. Such techniques have been applied to transmission electron microscopy (TEM) images (Op de Beeck et al., 1996; Bajt et al., 2000; Meyer et al., 2000; Allen et al., 2001; Allen and Oxley, 2001), for phase–amplitude retrieval using the transport-of-intensity equation (Teague, 1983; Paganin and Nugent, 1998), for coherent diffractive imaging (Miao et al., 1999; Spence, 2007), Fourier holography (Eisebitt et al., 2004) and ptychography (Faulkner and Rodenburg, 2004; Rodenburg et al., 2007).

Whilst chapter 5 demonstrates the retrieval from a single image of a wave function with only phase variations, more complex electron wave functions, e.g. those that include both phase and amplitude variations, may in general be recovered using a series of images (Misell, 1973; Op de Beeck et al., 1996; Paganin and Nugent, 1998; Bajt et al., 2000; Allen and Oxley, 2001; Gureyev et al., 2004). In the future, phase and/or amplitude retrieval methods could and should be applied to experimental LEEM images from the new generation of aberration corrected instruments to extract high resolution structural information.

## 1.5 Wave optical treatment of MEM image contrast

In addition and complementary to the ray-based methods of chapters 2 and 3, and inspired by the methods of chapters 4 and 5, we next consider the development of a wave optical description of MEM, using a similar formalism to that developed for LEEM in chapter 4. This is desirable because it would comprehensively include aberrations in both standard and aberration-corrected instruments, and allow the implementation of existing phase and amplitude retrieval techniques, as well as deepening our understanding of MEM image contrast. However, the first major requirement in moving from a ray to a wave-based treatment of MEM is to properly understand the behaviour of an electron in the turning region of the electron beam, which in MEM occurs above the specimen surface. Additionally, as the electron beam only interacts with the electric field above the specimen rather than the surface directly, the connection between surface features and properties and the electron wave function may be more complex in MEM than in LEEM. In addressing these two requirements, it is useful to first employ analytical methods where possible, as they may yield important physical insight into the mechanisms of contrast.

### 1.5.1 Investigating the MEM turn around region (Paper 5)

In chapter 6 we consider the first requirement, investigating the turn around region of the electron beam. Following a similar analytical method to Hermans and Petterson (1970), the Schrödinger equation for the electron in the immersion lens of a typical MEM instrument is solved, and the electron wave is described via Airy functions (Abramowitz and Stegun, 1964; Hermans and Petterson, 1970; Kennedy et al., 2006). In particular, in chapter 6 we investigate the variation of phase in the vicinity of the turn around region. We discover a transition that occurs between hard and soft reflection limits, where the “softness” of reflection is defined as the distance over which the wave turns around compared to its wavelength. This is of interest in its own right (Friedrich and Trost, 1996a,b), and provides further insight into the accumulation of phase in the turn around region of the electron beam, where the sensitivity of MEM is highest.

### 1.5.2 Sensitivity of MEM to weak fields (Paper 6)

Finally, chapter 7 extends the investigation into the turning region of the electron beam (chapter 6), and considers the sensitivity of MEM to weak fields above the specimen surface. This includes the intriguing possibility of moving the turn around region well above the cathode surface, to image weak fields not created by the specimen itself, a capability unique to MEM. One example is the weak ponderomotive potential experienced by an electron in a standing light wave (Kapitza and Dirac, 1933; Freimund and Batelaan, 2002). The high sensitivity of low energy electrons to weak potentials, and the relatively long exposure time in the turn around region compared to transmission experiments, makes the imaging of weak potentials via MEM a compelling possibility, and may extend the application of MEM beyond surface science studies.

### 1.5.3 Completing the wave optical treatment of MEM

Building upon chapters 6 and 7, future work includes addressing the second requirement of a wave optical description of MEM, i.e. understanding the connection between surface features and properties and the electron wave function. One possibility is in using the ray trajectory method of chapter 3, where each trajectory may be given the same initial phase, and then by integrating along each distinct path and accounting for the phase changes associated with caustics (Marcuse, 1976), a phase difference between ray

trajectories will accumulate. This would produce an estimate of the electron wave function's phase across a plane parallel to the cathode surface, opening up the direct application of transfer function theory.

## **1.6 Application to PEEM image contrast**

The methods developed above, which describe image contrast in MEM and LEEM and are used to recover specimen information from experimental images, may in principle be applied to PEEM with appropriate modifications. The Laplacian imaging theory may be altered to include only the electron motion away from the surface, reducing the shifts and corresponding blurring functions. The caustic imaging theory of MEM may likewise be modified so that a family of rays is emitted from the specimen surface with very low energy, with trajectories traced away from the surface through the electric field. This would enable, for example, a comparison of the apparent sizes of specimen features with the actual size on the cathode surface. With appropriate aberration coefficients the wave optical treatment of LEEM may also be applied to understanding PEEM image contrast, and has been performed by Schramm et al. (2010). The loss of spatial coherence in the electron wave in PEEM, due to the random creation of photoelectrons, must be taken into account in general (Schramm et al., 2010). These extensions are not considered in detail here.

## **1.7 Overview of the thesis**

This chapter has briefly reviewed MEM and LEEM, establishing context for each of the six proceeding chapters that comprise the bulk of this thesis by publication. Chapters 2 and 3 develop two complementary treatments of MEM image contrast using primarily ray-based methods. The thesis then moves on to LEEM image contrast in chapter 4, developing a wave optical treatment of LEEM with the specific example of phase contrast images of surface steps. This model is used in chapter 5, which applies phase retrieval techniques to LEEM phase contrast images. The thesis then returns to MEM imaging, developing a wave optical description of MEM image contrast by first examining the electron behaviour in the immersion lens in chapters 6 and 7, with emphasis on the turn around region and the sensitivity of the electron beam to weak fields in this region. The thesis is then brought to a close in chapter 8 with concluding remarks and comments on future work.

---

## Laplacian image contrast in MEM

This chapter is an author generated post print of the article

S. M. Kennedy, C. X. Zheng, W. X. Tang, D. M. Paganin, and D. E. Jesson, 'Laplacian image contrast in mirror electron microscopy,' *Proc. R. Soc. A*, **466** (2010) 2857–2874, available electronically at <http://rspa.royalsocietypublishing.org/> or via doi:10.1098/rspa.2010.0093.



### Declaration for thesis chapter 'Laplacian image contrast in mirror electron microscopy.'

#### Declaration by candidate

For this chapter, the nature and extent of my contribution to the work was the following:

Nature of contribution	Extent of contribution (%)
Developed the model used in the paper, performed the image simulations, co-wrote the paper.	70

The following co-authors contributed to the work. Co-authors who are students at Monash University must also indicate the extent of their contribution in percentage terms:

Name	Nature of contribution	Extent of contribution (%) for student co-authors only
Changxi Zheng	Provided experimental images, both AFM and MEM, and provided technical expertise.	25
Wen-Xin Tang	Provided technical expertise.	
David Paganin	Co-wrote, helped develop the model and provided technical expertise.	
David Jesson	Co-wrote, helped develop the model and provided technical expertise.	

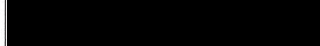
Candidate's Signature  Date 25/8/10

#### Declaration by co-authors

The undersigned hereby certify that:

- (1) the above declaration correctly reflects the nature and extent of the candidate's contribution to this work, and the nature of the contribution of each of the co-authors.
- (2) they meet the criteria for authorship in that they have participated in the conception, execution, or interpretation, of at least that part of the publication in their field of expertise;
- (3) they take public responsibility for their part of the publication, except for the responsible author who accepts overall responsibility for the publication;
- (4) there are no other authors of the publication according to these criteria;
- (5) potential conflicts of interest have been disclosed to (a) granting bodies, (b) the editor or publisher of journals or other publications, and (c) the head of the responsible academic unit; and
- (6) the original data are stored at the following location(s) and will be held for at least five years from the date indicated below:

Location(s)

Signature 1		Date 25/08/10
Signature 2		25/08/10
Signature 3		26/08/2010
Signature 4		26-8-10



# Laplacian image contrast in mirror electron microscopy

BY S. M. KENNEDY, C. X. ZHENG, W. X. TANG, D. M. PAGANIN, D. E. JESSON†

*School of Physics, Monash University, Victoria 3800, Australia.*

We discuss an intuitive approach to interpreting mirror electron microscope (MEM) images, whereby image contrast is primarily caused by the Laplacian of small height or potential variations across a sample surface. This variation is blurred slightly to account for the interaction of the electrons with the electrical potential away from the surface. The method is derived from the established geometrical theory of MEM contrast, and whilst it loses quantitative accuracy outside its domain of validity, it retains a simplicity that enables rapid interpretation of MEM images. A strong parallel exists between this method and out of focus contrast in transmission electron microscopy (TEM), which allows a number of extensions to be made such as including the effects of spherical and chromatic aberration.

**Keywords:** Mirror electron microscopy (MEM), Laplacian image contrast, phase contrast, Ga droplets, GaAs

## 1. Introduction

Mirror electron microscopy (MEM) is a well-established technique which has seen wide application in the real time study of surface phenomena. Applications include the study of chemical processes at solid surfaces (Świąch *et al.* 1993), surface magnetic fields (Barnett & Nixon 1967*a*), electric field contrast (Luk'yanov *et al.* 1974; Bok 1978; Slezák *et al.* 2000; Shimakura *et al.* 2008) and droplet surface dynamics (Tersoff *et al.* 2009). MEM is unique in surface electron microscopy in that electrons neither impact nor are emitted from the specimen surface. Instead, a near-normally incident beam is reflected at equipotential surfaces just above the specimen. This is achieved by holding the specimen at a small negative voltage relative to the electron source. As the electrons reverse direction, they are travelling very slowly and are consequently sensitive to spatial and/or temporal variations in microfields in the vicinity of the surface. These microfields may, for example, result from small variations in the electric field above the cathode caused by the surface topography (Bauer 1998; Nepijko *et al.* 2001*b*; Speake & Trenkel 2003) and/or variations in the electric potential of the specimen itself, including contact potentials, surface charges and varying conductivity (Barnett & Nixon 1967*a, b*; Luk'yanov *et al.* 1974; Bok 1978; Świąch *et al.* 1993; Godehardt 1995). MEM therefore has a significant advantage in that it can probe surface phenomena benignly, without electrons impacting the surface.

The reflected electrons in MEM contain information concerning microfields which are in turn related to the topography and/or the electrical and magnetic properties of the surface. This has stimulated significant efforts over the years to interpret MEM image contrast and extract quantitative information regarding the microfields and surface properties. Although a variety of approaches have been employed, including some based on wave mechanics (Hermans & Petterson 1970; Kennedy *et al.* 2006), most have been based on geometrical ray tracing techniques (Barnett & Nixon 1967*b*; Sedov 1970; Luk'yanov *et al.* 1974; Someya & Kobayashi 1974; Bok 1978; Rempfer & Griffith 1992; Świąch *et al.* 1993; Godehardt 1995). Building on this latter work, a geometrical theory has been developed in which MEM contrast is viewed as a transverse redistribution of electron current density on an imaging screen due to shifts in electron trajectories following interaction with microfields

† Author for correspondence (David.Jesson@monash.edu).

just above the specimen surface (Sedov 1970; Dyukov *et al.* 1991; Nepijko & Sedov 1997). This work, which has been used extensively to simulate MEM and photoemission electron microscopy (PEEM) contrast in a variety of situations (Nepijko *et al.* 2001*a, b*, 2003, 2007; Jesson *et al.* 2007; Nepijko & Schönhense 2010; Tang *et al.* 2009), will form the basis of this paper and we henceforth refer to this approach as the geometrical theory of MEM contrast.

An advantage of the geometrical theory of MEM contrast is that, for special geometries, the electron shifts can be calculated analytically which can provide important insight into the mechanisms of contrast (Nepijko & Sedov 1997; Nepijko *et al.* 2001*a*). Presently, however, there is no direct way of intuitively interpreting MEM contrast of a given general specimen. Here, we present a theory of Laplacian image contrast (see, for example, Berry (2006)) in MEM which is an approximation of the geometrical theory, yet applicable to a wide range of practical imaging situations. The advantage of the theory is that the image contrast can be interpreted in terms of the Laplacian of an effective two-dimensional phase object which is directly related to the near-surface microfield. For variations in surface topography, the effective phase is related to a blurred surface height function so that the contrast can be intuitively linked to surface features. Even beyond its strict range of applicability, Laplacian image contrast retains a simplicity which enables rapid interpretation of MEM images. We will show that a strong parallel exists between this method and ‘out of focus’ contrast in transmission electron microscopy (TEM) (Cowley 1995; Spence 2003). This allows a number of extensions to be made to the intuitive method, such as including the effects of spherical and chromatic aberration.

## 2. Geometrical theory of MEM contrast

Nepijko, Sedov and Dyukov (Dyukov *et al.* 1991; Nepijko & Sedov 1997), building upon earlier work of Sedov (1970), Luk’yanov *et al.* (1974) and others (Barnett & Nixon 1967*b*; Bok 1978) have developed a robust geometrical theory of MEM contrast. The approach utilizes a predominantly classical ‘ray based’ description of the electron motion inside the imaging system. While the major results are quoted by Nepijko & Sedov (1997) and Nepijko *et al.* (2001*b*, 2003), and many salient points of the theory are emphasized by Luk’yanov *et al.* (1974), the foundations of the methodology are less accessible (Dyukov *et al.* 1991, in Russian). Since the geometrical theory is the basis for our development of a theory of Laplacian image contrast in MEM, we therefore briefly summarize the key steps here, highlighting the assumptions used in the general case as well as adapting the method to a low energy electron microscope (LEEM) imaging system.

A typical electrostatic MEM immersion lens is shown schematically in figure 1. Here the  $z$  axis coincides with the optical axis of the immersion lens and the planar sample surface corresponds to the  $(x, y)$  plane of a Cartesian coordinate system. The specimen is held at a negative potential ( $V < 0$ ) relative to the grounded anode aperture a distance  $L$  away. The specimen therefore acts as the cathode of the immersion objective lens (Barnett & Nixon 1967*b*; Luk’yanov *et al.* 1974; Bok 1978; Bauer 1985). Electrons, accelerated to initial energy  $U$ , travel along the optic axis, pass through the anode aperture (figure 1) and are deflected by the difference in electric field either side of the aperture (Grant & Phillips 1990). For a perfectly smooth sample surface, the electric field between anode and cathode is uniform (except very close to the aperture) and we may trace the electron path classically, whereby the electron moves along a parabolic path as shown in figure 1. If the potential  $V$  is chosen such that the electron has zero energy at the cathode surface, i.e.  $U = -eV$  with electronic charge  $-e$ , the classical turning point is at  $z = L$ . Experimentally it is customary to adjust  $V$  so that  $U < -eV$  and the classical turning point is at  $z = L_M$  as per figure 1, which is located a distance of  $\delta$  above the specimen surface. For simplicity deflections in the  $y$  direction are not shown, but they are treated independently in the same fashion.

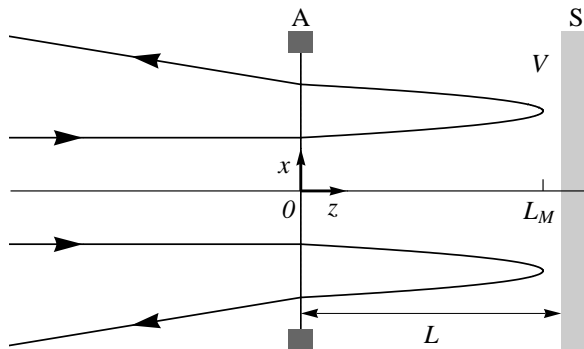


Figure 1. Classical electron trajectories (solid lines), travelling parallel to the optical axis  $z$  along the centre of an anode aperture A, are deflected away from the axis due to the aperture acting as a diverging lens, both upon entering and exiting the anode–cathode region. The aperture separates an electric field free region ( $z < 0$ ) from a constant electric field of  $V/L$  ( $0 \leq z \leq L$ ), where the cathode specimen S is held at potential  $V < 0$  compared to the anode. An electron of energy  $U < -eV$  turns at a distance of  $z = L_M$ . The  $y$  axis extends out of the page. Based on Nepijko & Sedov (1997).

The objective lenses of modern LEEM instruments frequently consist of the electrostatic MEM immersion lens shown in figure 1 combined with a magnetic imaging part (Bauer 1994). To a good approximation these two components can be treated separately (Bauer 1985). As shown in figure 2, the effect of the homogeneous electric field on the trajectory of an electron which turns around a distance  $\delta$  above the surface is that it appears to originate from the point  $P$ , located in the virtual image plane at a distance  $2L_M$  from the anode where  $L_M = L - \delta$ . The effect of the anode aperture is incorporated by assuming that the uniform field is terminated by an ideal diverging lens (Grant & Phillips 1990; Rempfer & Griffith 1992; Nepijko & Sedov 1997), as shown in figure 2. The virtual specimen created by the uniform field at  $z = 2L_M$  is the object of the aperture lens with focal length  $f = -4L_M$ . This lens forms a virtual image of the virtual specimen at point  $Q$  which is located in a virtual image plane a distance  $4L_M/3$  from the anode. This is the object plane of the magnetic LEEM objective lens.

The geometrical theory of MEM contrast (Dyukov *et al.* 1991; Nepijko & Sedov 1997) considers the interaction of an electron with variations in the electrical potential  $V(x, y, \bar{z})$  above the sample surface, where  $\bar{z} = L - z$ . This potential is associated with a local surface potential function  $V(x, y, \bar{z} = 0)$  which may, for example, arise due to areas of differing work function or applied voltage. A further case arises when the surface is equipotential but varies in height. This situation is equivalent to a planar surface with a corresponding potential distribution (Nepijko & Sedov 1997)

$$V(x, y, \bar{z} = 0) = VH(x, y)/L, \quad (2.1)$$

where  $H(x, y)$  specifies the surface height of the specimen. In this paper we will chiefly concentrate on situations of MEM contrast from variations in surface topography via equation (2.1). However, we emphasize that the discussion is entirely valid for variations in potential which can be incorporated directly in  $V(x, y, \bar{z} = 0)$ . By solving the Dirichlet problem for Laplace's equation for a half space we have (Polozhiy 1967; Boudjelkha & Diaz 1972; Nepijko & Sedov 1997)

$$V(x, y, \bar{z}) = \frac{\bar{z}}{2\pi} \int \int_{-\infty}^{\infty} \frac{V(\xi, \eta, \bar{z} = 0)}{((x - \xi)^2 + (y - \eta)^2 + \bar{z}^2)^{3/2}} d\xi d\eta, \quad (2.2)$$

which expressed as a convolution is (Cowley 1995; Press *et al.* 2007)

$$V(x, y, \bar{z}) = \frac{\bar{z}}{2\pi} V(x, y, \bar{z} = 0) \otimes (x^2 + y^2 + \bar{z}^2)^{-3/2}. \quad (2.3)$$

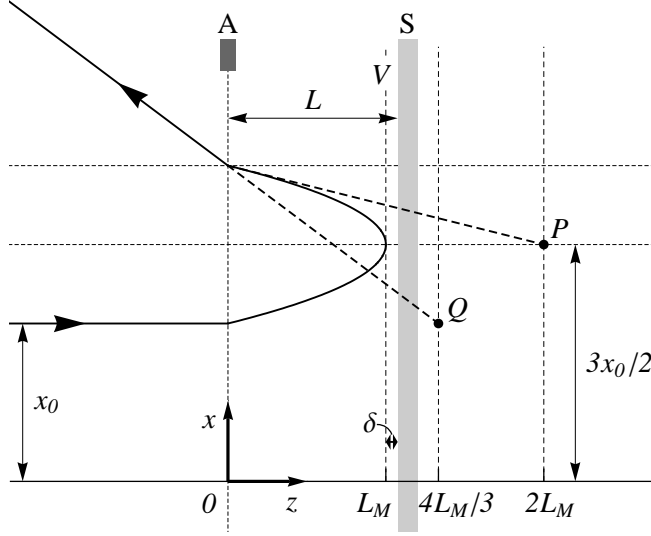


Figure 2. The electron trajectory (solid line) entering the anode aperture A at a lateral position  $x_0$  is deflected by the homogeneous electric field in the region  $0 \leq z \leq L$  so that it appears to originate from the point P at  $z = 2L_M$ . Upon passing back through the anode aperture A the electron trajectory is again deflected so that the apparent point of origin P is moved to Q at a distance of  $z = 4L_M/3$  with a magnification of  $2/3$ . Note that the electron is closest to the surface S at  $x = 3x_0/2$ .

From equation (2.1), the variation in electric potential above the specimen surface can then be expressed as the height function  $H(x, y)$  convolved with a smoothing function,

$$V(x, y, \bar{z}) = \frac{\bar{z}V}{2\pi L} H(x, y) \otimes (x^2 + y^2 + \bar{z}^2)^{-3/2}. \quad (2.4)$$

Physically the smoothing function represents the blurring and softening of the electric field when moving away the cathode surface. This smoothed potential will therefore extend beyond the  $(x, y)$  range of a localised hill or valley described by  $H(x, y)$ , for example. The additional potential  $V(x, y, \bar{z})$  rapidly approaches zero as  $\bar{z}$  increases away from the surface. The geometrical theory therefore assumes that any change to the electron motion caused by the finite height variation of the cathode occurs very close to the sample surface. In addition, the  $z$ -dimension motion is assumed to be unchanged, so that all of the momentum change in the transverse dimensions  $(x, y)$  occurs very close to the classical turning point at  $z = L_M$ . This amounts to a column approximation, whereby an electron entering the anode at  $(x_0, y_0)$  is affected most strongly by the cathode at  $(3x_0/2, 3y_0/2)$  where it is closest to the surface (see figure 2). The  $x$  and  $y$  derivatives of the potential, integrated along the  $z$  axis for the column  $(3x_0/2, 3y_0/2)$  therefore give the change to the  $x$  and  $y$  velocities respectively. Using the approach of Nepijko & Sedov (1997) and Dyukov *et al.* (1991) the shift of electron position  $S_x, S_y$  on the plane  $z = 4L_M/3 + \Delta f$  due to  $H(x, y)$  for a small defocus  $\Delta f$  of the magnetic objective lens (see figure 3) is given by

$$S_x(x, y, \delta, \Delta f) = \frac{\partial}{\partial x} \frac{\sqrt{L_M}}{\pi} \frac{9\Delta f}{8L_M - 6\Delta f} H(x, y) \otimes ((\delta^2 + x^2 + y^2)^{-3/4} (2E_E(x, y, \delta) - E_K(x, y, \delta))), \quad (2.5)$$

$$S_y(x, y, \delta, \Delta f) = \frac{\partial}{\partial y} \frac{\sqrt{L_M}}{\pi} \frac{9\Delta f}{8L_M - 6\Delta f} H(x, y) \otimes ((\delta^2 + x^2 + y^2)^{-3/4} (2E_E(x, y, \delta) - E_K(x, y, \delta))), \quad (2.6)$$

where

$$E_E(x, y, \delta) = E \left( \frac{1}{2} - \frac{\delta}{2(\delta^2 + x^2 + y^2)^{1/2}} \right), \quad E_K(x, y, \delta) = K \left( \frac{1}{2} - \frac{\delta}{2(\delta^2 + x^2 + y^2)^{1/2}} \right), \quad (2.7)$$

and  $K$ ,  $E$  respectively denote complete elliptic integrals of the first and second kind (Abramowitz & Stegun 1964; Borwein & Borwein 1987). Here, the magnitude of the electron shift is scaled to the object coordinates (Dyukov *et al.* 1991; Nepijko & Sedov 1997). Note that for  $\Delta f = 0$  the electron shifts are zero, even for a rough surface with non-zero  $H(x, y)$ . The plane  $z = 4L_M/3$  therefore corresponds to the in-focus plane of minimum contrast and a finite defocus  $\Delta f$  is required to obtain image contrast. In the special case where  $\delta = 0$  the electron has sufficient energy to reach the surface, and the shifts simplify to

$$S_x(x, y, \Delta f) = \frac{\partial}{\partial x} \sqrt{\frac{L}{\pi^3}} \frac{9\Delta f}{8L - 6\Delta f} \Gamma(3/4)^2 H(x, y) \otimes (x^2 + y^2)^{-3/4}, \quad (2.8)$$

and similarly for  $S_y$ . For later convenience, we separate the derivatives in  $S_x$  and  $S_y$  from the convolution of the height with the blurring function, introducing the blurred height  $H_B$

$$H_B(x, y, \delta, \Delta f) = \frac{\Delta f}{4L_M - 3\Delta f} H(x, y) \otimes B(x, y, \delta). \quad (2.9)$$

The blurring function is

$$B(x, y, \delta) = \frac{9\sqrt{L_M}}{2\pi} (\delta^2 + x^2 + y^2)^{-3/4} (2E_E(x, y, \delta) - E_K(x, y, \delta)), \quad (2.10)$$

which incorporates the smoothing or softening of the electric field as we move away from the cathode surface (see equation (2.4)), and the resulting interaction of the electron with this field. Note that the factor  $\Delta f/(4L_M - 3\Delta f)$  in equation (2.9) also contributes to the blurring of the height, but it is kept separate from  $B(x, y, \delta)$  for later convenience. Equation (2.5), for example, can then be expressed as

$$S_x(x, y, \delta, \Delta f) = (\partial/\partial x)H_B(x, y, \delta, \Delta f). \quad (2.11)$$

The shifts in electron position defined by equations (2.5) and (2.6) result in a redistribution of intensity on the plane  $z = 4L_M/3 + \Delta f$ . The new intensity distribution can be derived from electron flux conservation giving (Dyukov *et al.* 1991; Nepijko *et al.* 2001b)

$$I(x + S_x, y + S_y) = I_0(x, y) \left| 1 + \frac{\partial S_x}{\partial x} + \frac{\partial S_y}{\partial y} + \frac{\partial S_x}{\partial x} \frac{\partial S_y}{\partial y} - \frac{\partial S_x}{\partial y} \frac{\partial S_y}{\partial x} \right|, \quad (2.12)$$

where  $I_0(x, y)$  is the unperturbed intensity distribution on the plane corresponding to  $H(x, y) = 0$  and is typically taken as unity. Intensity values are therefore calculated from the first spatial derivatives of the shift functions, and these are moved from  $(x, y)$  to  $(x + S_x, y + S_y)$  to evaluate the new intensity distribution.

### 3. Laplacian image contrast in MEM

We now consider the geometrical theory of MEM contrast in the limit of small objective lens defocus and/or slowly varying  $H(x, y)$ , which is an important practical case frequently encountered in MEM. In addition to the assumptions underpinning the geometrical model highlighted in section §2, we require that the derivatives of the blurred height are small,

$$|\partial^2 H_B(x, y, \delta, \Delta f)/\partial x^2| \ll 1, \quad |\partial^2 H_B(x, y, \delta, \Delta f)/\partial y^2| \ll 1, \quad (3.1)$$

which for simplicity we will refer to as

$$|\nabla_{\perp}^2 H_B(x, y, \delta, \Delta f)| \ll 1, \quad (3.2)$$

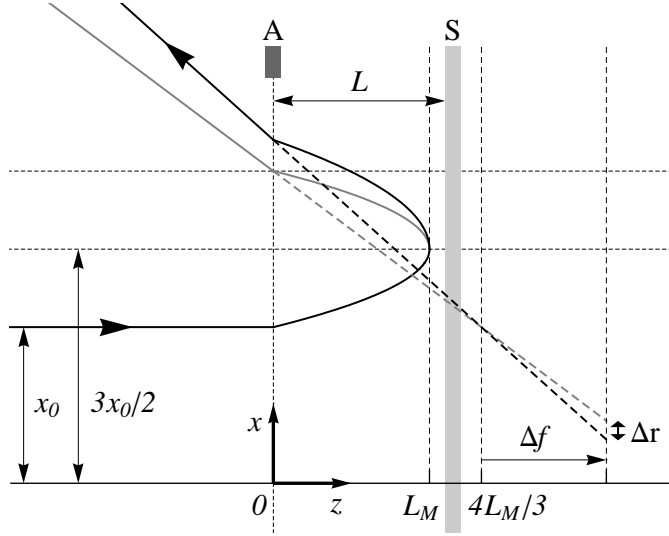


Figure 3. The unperturbed (grey line) and perturbed (black line) electron trajectories are traced back along their apparent straight line paths (dashed lines) to the plane  $z = 4L_M/3 + \Delta f$ . The difference in their position  $\Delta r$  is scaled by the expected magnification of the image on this plane relative to the cathode surface S, to obtain the electron position shifts  $S_x$  and  $S_y$  in the specimen plane.

where  $\nabla_{\perp}^2$  is the transverse Laplacian ( $\partial^2/\partial x^2 + \partial^2/\partial y^2$ ). For a given blurring function  $B$  (equation 2.10) that is determined by the experimental parameters, the required limits of equations (3.1) and (3.2) are met with a sufficiently small objective lens defocus  $\Delta f$  satisfying

$$|\Delta f| < 4L_M / (3 + \max_{x,y} |\nabla_{\perp}^2 H(x,y) \otimes B(x,y,\delta)|), \quad (3.3)$$

where  $\max_{x,y} g(x,y)$  denotes the maximum value of  $g(x,y)$  over the range of points  $(x,y)$ . Conversely, if we require that the maximum  $|\Delta f|$  used in a through-focal series of images is large enough to provide significant image contrast, i.e.  $|\Delta f| > \alpha$  for some distance  $\alpha$ , equation (3.3) demands that  $H(x,y)$  be sufficiently slowly varying to satisfy  $\max_{x,y} |\nabla_{\perp}^2 H(x,y) \otimes B(x,y,\delta)| < -3 + 4L_M/\alpha$ . Note that smoothness of the height profile is not required, only that the Laplacian of the height profile (blurred by the function  $B$ ) and/or the defocus is small enough to satisfy equations (3.1) and (3.2).

Inserting equations (2.9) and (2.11) into equation (2.12), the image intensity can be expressed in terms of the blurred height function as

$$I\left(x + \frac{\partial H_B}{\partial x}, y + \frac{\partial H_B}{\partial y}, \delta, \Delta f\right) = 1 / \left| 1 + \frac{\partial^2 H_B}{\partial x^2} + \frac{\partial^2 H_B}{\partial y^2} + \left(\frac{\partial^2 H_B}{\partial x^2}\right) \left(\frac{\partial^2 H_B}{\partial y^2}\right) - \left(\frac{\partial^2 H_B}{\partial x \partial y}\right)^2 \right|. \quad (3.4)$$

For small defocus  $\Delta f$  and/or slowly varying  $H(x,y)$  ensuring small derivatives of the blurred height (equations (3.1) and (3.2)), the intensity expression is approximated by

$$I(x,y,\delta,\Delta f) \approx 1 / |1 + \partial^2 H_B / \partial x^2 + \partial^2 H_B / \partial y^2|. \quad (3.5)$$

This is valid for small shifts in electron trajectory (see equation (2.11)) so that we have neglected the change in  $x, y$  coordinates in  $I(x,y,\delta,\Delta f)$  and derivatives greater than second order. Since the second derivatives in equation (3.5) are much smaller than unity, the denominator will always be positive, so we may remove the absolute value signs and take the binomial approximation of the denominator giving

$$I(x,y,\delta,\Delta f) \approx 1 - (\partial^2/\partial x^2 + \partial^2/\partial y^2)H_B(x,y,\delta,\Delta f) = 1 - \nabla_{\perp}^2 H_B(x,y,\delta,\Delta f). \quad (3.6)$$

The blurred height contains the constant term  $\Delta f/(4L_M - 3\Delta f)$  (see equation (2.9)), and provided we choose a defocus much smaller than the sample-to-anode distance  $L$ , e.g.  $\Delta f = 10^{-5}$  m,  $L = 10^{-3}$  m, this term is approximately proportional to the defocus  $\Delta f$ . So we may write the intensity as

$$I(x, y, \delta, \Delta f) \approx 1 - \Delta f \nabla_{\perp}^2 H(x, y) \otimes B(x, y, \delta)/4L_M, \quad (3.7)$$

where the blurring function  $B(x, y, \delta)$  is given in equation (2.10). This indicates that where the height variation and/or defocus is small enough to satisfy equation (3.2), the image intensity on the ‘out of focus’ plane  $z = 4L_M/3 + \Delta f$  is the Laplacian image of the height function, blurred with a function  $B(x, y, \delta)/4L_M$  to account for the interaction of the electron with the electric field above the cathode surface. In the regime where this approximate expression is valid, we may therefore interpret MEM image contrast to be created solely by the transverse second derivatives (curvature) of the surface height variation, smoothed by a blurring function. This is an important result for the intuitive interpretation of MEM contrast of surface topography.

Laplacian imaging is widely encountered in many contexts ranging from X-Ray imaging (Paganin 2006) to oriental magic mirrors (Berry 2006) and their modern equivalent in Makyoh topography (Riesz 2000). It is also known as out of focus contrast in transmission electron microscopy (TEM) of thin specimens (Lynch *et al.* 1975; Cowley 1995; Spence 2003). The applicability of the Laplacian imaging formalism to MEM under particular conditions considerably simplifies image interpretation as we will discuss in §4.

#### 4. Intuitive interpretation of MEM image contrast

As an application of Laplacian imaging in MEM we apply the technique to investigate Ga droplets on GaAs (001). This system is known to exhibit droplet surface dynamics which obey an unusual temperature dependence (Tersoff *et al.* 2009). As Ga droplets move on the rough GaAs (001) surface they leave behind smooth trails as shown in the atomic force microscope (AFM) image in figure 4. Outside of the trail there is significant surface roughness and we obtain a mean trail profile by averaging the surface height along the  $y$  axis in the framed region shown in figure 4. The resulting averaged cross-sectional profile, contained in figure 5(a), is  $1.9 \mu\text{m}$  wide and  $14 \text{ nm}$  deep. For the range of droplet sizes studied by AFM we find that the width to depth ratio of the trails is approximately constant ( $\sim 140$ ). With  $L = 2 \text{ mm}$ ,  $\delta = 40 \text{ nm}$ ,  $V = -20000.4 \text{ V}$  and  $U = 20 \text{ keV}$ , and for the droplet trails considered here we find that  $\max_{x,y} |\nabla_{\perp}^2 H(x, y) \otimes B(x, y, \delta)| \approx 35 \text{ m}^{-1}$  or lower, so that the condition of equation (3.3) requires that  $|\Delta f| < 200 \mu\text{m}$  in order to satisfy  $|\nabla_{\perp}^2 H_B| \ll 1$ . Therefore the assumptions underpinning a Laplacian contrast interpretation as outlined in §3 are valid and we choose the droplet trails as convenient test objects for Laplacian MEM imaging. Note that the height of the droplet itself (denoted ‘D’ in figure 4) is too large ( $0.3 \mu\text{m}$  above the cathode surface) to satisfy the assumption that changes in the  $z$ -component of the electron motion can be neglected. Therefore, it is inappropriate to apply the geometrical theory and a Laplacian interpretation in this case.

It is experimentally impractical to obtain both AFM and MEM images of the same droplet trail, therefore we consider only the general features of the AFM data of figure 4. Specifically, we ignore the significant surface roughness outside the trail, still present due to the limited area available for averaging, which will inevitably lead to strong intensity fluctuations in MEM images. So rather than use the AFM data directly in the Laplacian MEM method, in this example we instead model the trail using a height function  $H(x)$  which is the sum of two inverse tangent functions,

$$H(x) = \frac{T}{\pi} \left( \tan^{-1} \left( \frac{x - R}{O} \right) - \tan^{-1} \left( \frac{x + R}{O} \right) \right). \quad (4.1)$$

Here  $T$  sets the maximum depth of the trail,  $R$  is the distance of the side from the centre, and  $O$  sets the steepness of the trail edge, e.g. for  $O = 0.1 \mu\text{m}$ , 80% of the variation of the trail edge about

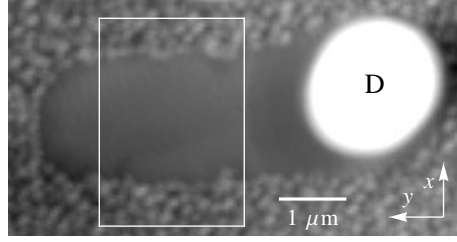


Figure 4. Atomic Force Microscope (AFM) image of a trail left by a moving Ga droplet marked D on a GaAs (001) surface. The region inside the box is integrated along  $y$  to obtain a one dimensional height profile in  $x$ , shown in figure 5(a).

its midpoint occurs over a distance of  $0.5 \mu\text{m}$  (see figure 5(a)). A background linear variation in  $x$  in the AFM data was ignored when fitting the height function (the variation was removed to give figure 5(a)), as we consider only the general features of the AFM data in this example. Note that the Laplacian contrast method is insensitive to linear variations in  $x$  that span the entire AFM image, since the second derivative of the height dominates the image contrast. However a linear variation that begins and/or ends within the data range will introduce a discontinuity where the linear variation starts and/or finishes, which has a non-zero second derivative and will contribute to the image intensity.

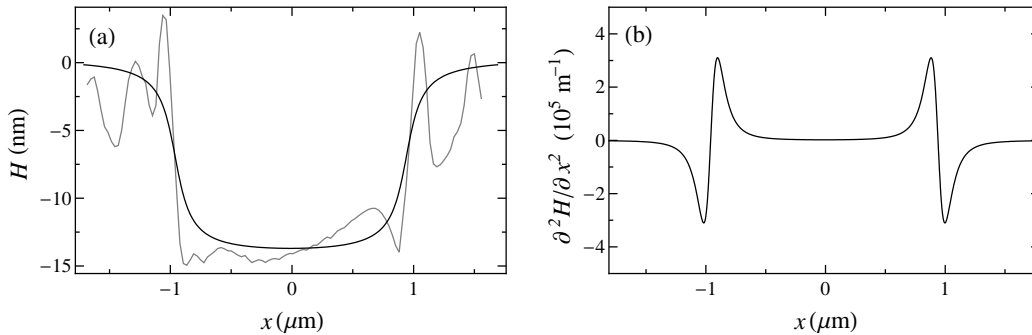


Figure 5. (a) Averaged one dimensional profile of a droplet trail on the cathode surface (grey line), along with the simplified height function  $H(x)$  (black line) fitted using equation (4.1) with  $R = 0.95 \mu\text{m}$ ,  $O = 0.1 \mu\text{m}$ ,  $T = 15 \text{ nm}$ . (b) Second spatial derivative of  $H(x)$  which provides the key qualitative features of the MEM image.

Fitting equation (4.1) to the general features of the averaged cross-sectional profile gives a simplified model of the trail height function (see figure 5(a)). As indicated in figure 5(a), we choose a broad trail edge to account for the width variation and surface roughness evident in figure 4. As discussed earlier, a major advantage of Laplacian imaging contrast is its ease of interpretation via equation (3.7). It is therefore straightforward to predict the general features of the image contrast of a droplet trail from the second derivative of the model trail height function contained in figure 5(a). This is shown in figure 5(b) and indicates that the MEM image should contain a bright and dark contrast band in the vicinity of the trail edges, along with constant intensity in the centre of the trail. We emphasise that such a first order interpretation of MEM contrast in terms of surface curvature is quite general and independent of the surface profile, provided the Laplacian imaging theory is valid. This has important practical value for studies of surface phenomena using MEM.

In practice, equation (3.7) indicates that the second derivative of  $H$  is softened or smoothed by convolution with the blurring function  $B(x, y, \delta)$  in forming the image, physically accounting for the electron interacting with the electric field above the cathode. The defocus  $\Delta f$  will affect both the magnitude and the sign of the contrast peaks. A qualitative comparison of simulated Laplacian contrast images, based on equation (3.7), with experimental MEM images of a trail similar to that in figure 4 is shown in figure 6 for negative, zero and positive defocus values. Although the surface roughness outside the trail region results in significant contrast fluctuations, it can be seen that the main features of the experimental image through-focus sequence are consistent with Laplacian imaging theory for a generalised trail profile. A more complex or realistic height profile, e.g. that recovered in §7 in figure 9(b), can account for image features caused by surface roughness. Figure 7 compares simulations and experimental profiles of the MEM image intensity for positive and negative defocus values. The latter profiles have been integrated over the two dimensional panel region on figure 6, parallel to the trail edges, to reduce the intensity fluctuations caused by the surface roughness. The good agreement in both cases again illustrates the applicability of Laplacian imaging which facilitates the interpretation of image contrast in terms of surface curvature.

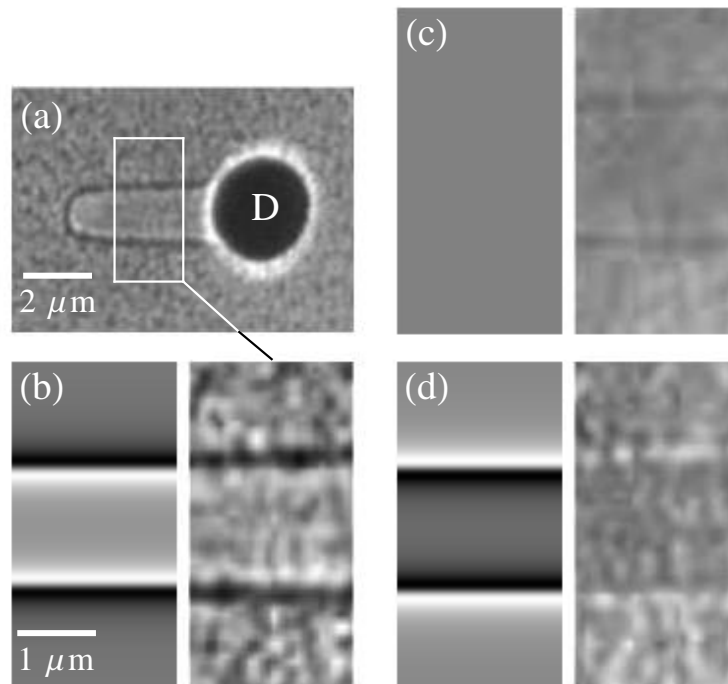


Figure 6. (a) MEM image of a moving Ga droplet D and the trail left on a GaAs (001) surface. Imaging conditions were  $V = -20000.4$  V,  $U = 20$  keV and  $L = 0.002$  m giving  $\delta = 40$  nm. Comparison of MEM images and simulations using equation (3.7) of the trail region contained in the frame in (a) are shown for (b) negative defocus ( $\Delta f = -15$   $\mu\text{m}$ ), (c) approximately zero defocus and (d) positive defocus ( $\Delta f = 15$   $\mu\text{m}$ ). The trail height function was approximated using equation (4.1) for  $R = 0.83$   $\mu\text{m}$ ,  $O = 0.1$   $\mu\text{m}$ ,  $T = 13$  nm.

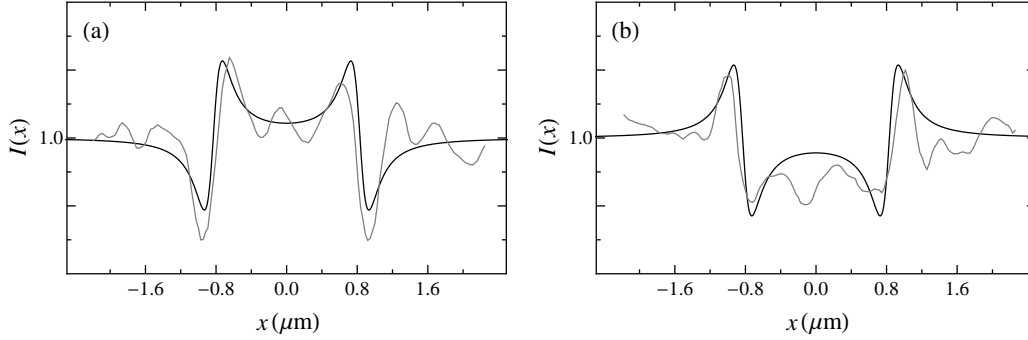


Figure 7. Comparison of simulated Laplacian contrast images (black lines) with experimental MEM intensity profiles of a droplet trail (grey lines). The experimental MEM intensity profiles were obtained by spatially averaging the intensities parallel to the trail edge over the two dimensional regions in figure 6(b) and (d). (a)  $\Delta f = -15 \mu\text{m}$ , (b)  $\Delta f = 15 \mu\text{m}$ . The trail height function was approximated using equation (4.1) for  $R = 0.83 \mu\text{m}$ ,  $O = 0.1 \mu\text{m}$ ,  $T = 13 \text{nm}$ . The grey scale intensity values in the experimental images were scaled to match the vertical axis of the simulations, allowing a qualitative comparison.

## 5. Comparison of the Laplacian and geometrical theory

It is important to establish and confirm the domain of validity of Laplacian imaging theory. We therefore compare image simulations based on the height profile of the droplet trail shown in figure 5(a), using the geometrical (equation (3.4)) and the approximate Laplacian contrast approaches (equation (3.7)). As shown in figure 8(a) for defocus  $\Delta f = -15 \mu\text{m}$  and classical turning point  $\delta = 40 \text{nm}$  from the cathode surface, the two methods agree very closely. Increasing the magnitude of the defocus and/or decreasing the turning point distance will increase the blurred height  $H_B$  and its derivatives. This weakens the validity of the assumption made in the Laplacian contrast method that  $|\nabla_{\perp}^2 H_B| \ll 1$ , and we therefore see an increased discrepancy between the image contrast generated from the Laplacian contrast and geometrical imaging simulation methods (figure 8(b)). Conversely, reducing the magnitude of the defocus and/or increasing the turning distance improves the agreement between the two approaches as expected.

## 6. Extensions of the Laplacian imaging theory of MEM contrast

Having established the applicability of Laplacian imaging theory to MEM we now utilise previous studies to extend our analysis. In particular, Laplacian contrast is also known as out of focus contrast in TEM of thin specimens (Lynch *et al.* 1975; Cowley 1995; Spence 2003), and we can utilise this formalism to include the effects of spherical and chromatic aberration. These aberrations are an intrinsic part of an MEM imaging system and limit resolution (Rempfer & Griffith 1992). Since a Laplacian contrast interpretation is applicable to imaging objects at high resolution provided  $|\nabla_{\perp}^2 H_B| \ll 1$ , it is important to incorporate such effects into the imaging theory. The expression for TEM out of focus contrast for a thin uniformly-illuminated specimen is (Lynch *et al.* 1975; Cowley 1995; Spence 2003)

$$I(x, y, z = z_0 + \Delta f) = 1 - k^{-1} \Delta f \nabla_{\perp}^2 \phi, \quad (6.1)$$

for a defocus  $\Delta f$  and electron wavenumber  $k = 2\pi/\lambda$ . The electron phase change through the specimen  $\phi$  is inversely proportional to the local electron wavelength  $\lambda$  so that the wavelength

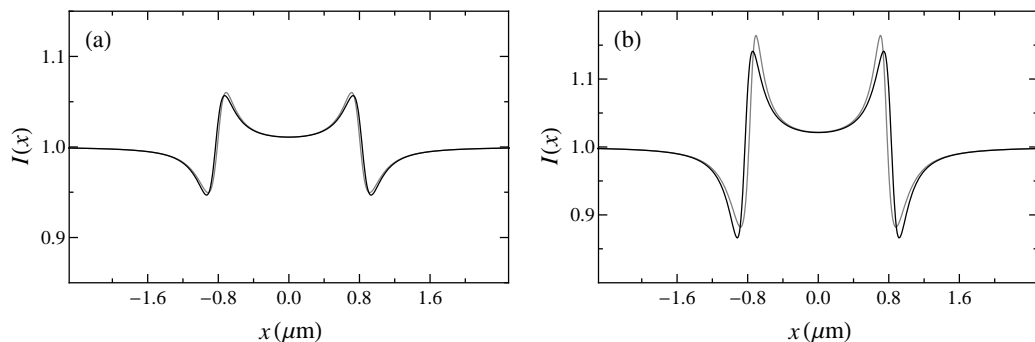


Figure 8. Comparison of the one dimensional intensity profile predicted using the geometrical treatment (grey line) with the Laplacian contrast method (black line), for the droplet trail height profile of figure 5, using  $R = 0.83 \mu\text{m}$ ,  $O = 0.1 \mu\text{m}$ ,  $T = 13 \text{ nm}$ . (a)  $\Delta f = -15 \mu\text{m}$ ,  $\delta = 40 \text{ nm}$ , (b)  $\Delta f = -30 \mu\text{m}$  and  $\delta = 20 \text{ nm}$ .

dependence factors out in equation (6.1) and so it is possible to extrapolate the wavelength to zero (cf. equation (6.4)).

We note that equation (6.1) is identical to the Laplacian theory description of MEM contrast (equation (3.7)) provided the phase of the wave function is

$$\phi(x, y, \delta) = \frac{k}{\Delta f} H_B(x, y, \delta, \Delta f). \quad (6.2)$$

We may view this as the effective phase variation of an electron wave post interaction with the cathode sample surface, which has been scaled up to the vacuum or post anode aperture energy. Equation (6.1) therefore describes the out of focus MEM contrast in the defocused image plane  $z = 4L_M/3 + \Delta f$ .

Lynch *et al.* (1975) extended the TEM out of focus expression to include the effects of spherical aberration, which depends on the bi-Laplacian or iterated Laplacian ( $\nabla_{\perp}^4 \equiv \nabla_{\perp}^2 \nabla_{\perp}^2$ ) of the phase variation  $\phi$ , scaled by the spherical aberration coefficient  $C_S$ ,

$$I(x, y, \delta, \Delta f) \approx 1 - \frac{\Delta f}{k} \nabla_{\perp}^2 \phi(x, y, \delta) + \frac{C_S}{2k^3} \nabla_{\perp}^4 \phi(x, y, \delta). \quad (6.3)$$

We may recast this equation using equation (6.2) to give

$$I(x, y, \delta, \Delta f) \approx 1 - \nabla_{\perp}^2 H_B(x, y, \delta, \Delta f) + \frac{C_S}{2\Delta f k^2} \nabla_{\perp}^4 H_B(x, y, \delta, \Delta f), \quad (6.4)$$

which extends our Laplacian contrast expression to include spherical aberration. For the resolutions employed in the study of droplet trails and with  $C_S$  values derived by Rempfer & Griffith (1992) we have found that including spherical aberration provides less than a one percent change in the simulated intensity variation. However, we anticipate that the inclusion of spherical aberration will be of benefit in simulating higher resolution images of surface objects within the domain of validity of Laplacian imaging.

We may also extend the Laplacian contrast method to include the effects of a finite energy spread in the electron beam, which causes chromatic aberration in the image intensity. A distribution in energy  $D(U)$  varies the classical turning point  $\delta$ , via

$$\delta = L \left( 1 + \frac{U}{eV} \right), \quad (6.5)$$

where the cathode surface is kept at a potential of  $V < 0$ . The distribution in turning point  $D(\delta)$  can then be obtained from the energy distribution, e.g.  $D(\delta) \approx D(U)dU/d\delta$ . Following the approach of Fejes (1977) we incoherently average over the distribution, summing up the contributions of each intensity (equation (3.7)) weighted by the distribution function,

$$I_C(x, y, \Delta f) = \int I(x, y, \delta, \Delta f)D(\delta)d\delta \approx \int D(\delta)d\delta - \nabla_{\perp}^2 \int H_B(x, y, \delta, \Delta f)D(\delta)d\delta. \quad (6.6)$$

Since the turning distance  $\delta$  only appears in the blurring function, in effect we may replace the monochromatic blurring function  $(\Delta f/(4L_M - 3\Delta f))B(x, y, \delta)$  with the chromatically averaged  $B_C(x, y, \delta_0, \Delta f)$ , given by

$$B_C(x, y, \delta_0, \Delta f) = \int \frac{\sqrt{L-\delta}}{\pi} \frac{9(\Delta f + 2(\delta - \delta_0))}{8(L-\delta) - 6(\Delta f + 2(\delta - \delta_0))} (\delta^2 + x^2 + y^2)^{-3/4} \\ \times (2E_E(x, y, \delta) - E_K(x, y, \delta))D(\delta)d\delta, \quad (6.7)$$

with a defocus of  $\Delta f + 2(\delta - \delta_0)$  to ensure that each intensity corresponds to the plane  $z = 4(L - \delta_0)/3 + \Delta f$ , and where  $\delta_0$  is the mean of the distribution. Chromatic aberration, then, can be incorporated into the approximate method by adjusting the blurring function, in essence averaging over several blurring functions to obtain the effective blurring function  $B_C$ . With a normalized distribution we then have

$$I_C(x, y, \delta_0, \Delta f) \approx 1 - \nabla_{\perp}^2 H(x, y) \otimes B_C(x, y, \delta_0, \Delta f). \quad (6.8)$$

As with spherical aberration, chromatic aberration has a small effect on simulating the MEM image contrast of the droplet trails (less than one percent as expected). This is true for a Gaussian energy distribution with a typical full-width-half-maximum equal to 0.3 eV for a Schottky field emission source and a variety of mean  $\delta_0$  values. However, we would again envisage that equation (6.8) will be of value for the study of surface objects at high resolution within the Laplacian imaging regime of  $|\nabla_{\perp}^2 H_B| \ll 1$ .

## 7. Inverse problem of Laplacian MEM imaging

Many of the geometrical treatments consider the important ‘inverse problem’ of MEM imaging, whereby image contrast is analysed to estimate the perturbed electric potential and/or the height variation of the specimen (Luk’yanov *et al.* 1974; Dyukov *et al.* 1991; Nepijko & Sedov 1997; Nepijko & Schönhense 2010). The inverse problem has also been explored in other areas of surface electron microscopy such as LEEM (Yu *et al.* 2010). In the Laplacian theory of MEM contrast this may be achieved in a very straightforward fashion using the Fourier derivative theorem (Cowley 1995; Paganin 2006) to convert between spatial derivatives and Fourier space coordinates,

$$\mathcal{F}(I(x, y, \delta, \Delta f) - 1) \approx \mathcal{F}(-\nabla_{\perp}^2 H_B(x, y, \delta, \Delta f)) = (k_x^2 + k_y^2)\mathcal{F}H_B(x, y, \delta, \Delta f). \quad (7.1)$$

Here  $k_x$  and  $k_y$  are the Fourier space coordinates corresponding to real space coordinates  $x$  and  $y$  respectively,  $\mathcal{F}$  is the Fourier transform with respect to  $x$  and  $y$ , and  $\mathcal{F}^{-1}$  is the corresponding inverse Fourier transform. We therefore have (Gureyev & Nugent 1997)

$$H_B(x, y, \delta, \Delta f) \approx \mathcal{F}^{-1}((k_x^2 + k_y^2)^{-1}\mathcal{F}(I(x, y, \delta, \Delta f) - 1)), \quad (7.2)$$

which in principle allows the recovery of the blurred height function from a single image, facilitating the analysis of MEM movie dynamics (Tersoff *et al.* 2009). This expression bears a strong resemblance to phase retrieval via the transport of intensity equation (Teague 1983; Gureyev & Nugent 1997; Paganin & Nugent 1998), whereby a phase contrast image may be used to recover

the original phase object.

Upon obtaining the blurred height function, we then deconvolve to obtain the height function, for example via equation (2.9) using the convolution theorem (Cowley 1995)

$$H(x, y, \delta) = \frac{(4L_M - 3\Delta f)}{2\pi\Delta f} \mathcal{F}^{-1} \left( \frac{\mathcal{F}(H_B(x, y, \delta, \Delta f))}{\mathcal{F}(B(x, y, \delta))} \right). \quad (7.3)$$

If the value of the defocus is not known, we can only recover the height to within the scaling factor  $(4L_M - 3\Delta f)/\Delta f$ . Here we present two preliminary examples in one dimension of the inverse problem of Laplacian MEM imaging. Figure 9(a) shows the recovered height using equations (7.3) and (7.3) from the simulated MEM images shown in figure 7. The recovered height is in very good agreement with the ideal height profile of equation (4.1), also shown in figure 9(a).

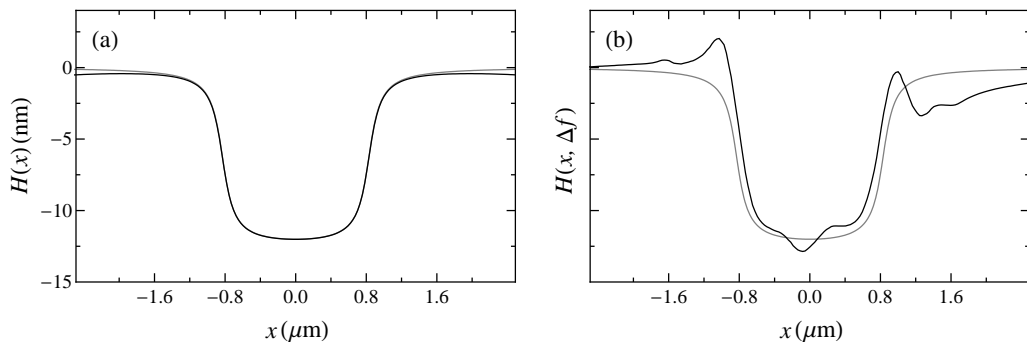


Figure 9. Recovered height profiles of the droplet trail (black lines) using equations (7.3) and (7.3) compared to the ideal height profile (grey lines) of equation (4.1) with  $R = 0.83 \mu\text{m}$ ,  $O = 0.1 \mu\text{m}$ ,  $T = 13 \text{ nm}$ . (a) the recovered height from the simulated MEM intensity profiles for the ideal height (black lines in figure 7), using  $\Delta f = -15 \mu\text{m}$ . (b) average of the recovered height profiles (black line) of the experimental MEM images (grey lines in figure 7). The recovered height  $H(x, \Delta f) = H(x)\Delta f/(4L_M - 3\Delta f)$  includes the scaling factor  $\Delta f/(4L_M - 3\Delta f)$  since  $\Delta f$  in each image was unknown.

Figure 9(b) shows an average of the recovered heights from the experimental MEM intensity profiles of figure 7 to within a scaling factor, as the specific defocus values were not known. The general features of the recovered height are in good agreement with the ideal height profile, with discrepancies largely due to the surface roughness evident in the recovered height profile. Using equation (3.7) to simulate the Laplacian image contrast of the recovered height profile of figure 9(b), we found that the normalised root mean squared difference between the simulated intensity and the measured MEM image intensity profiles (figure 7) was 3 % and 10 % for the negative and positive defocus images respectively.

## 8. Conclusions

We have demonstrated that Laplacian imaging theory can be applied to MEM imaging of surface topography (or equivalently surface potentials) provided the height function describing the surface topography is slowly spatially varying and/or the objective lens defocus is small. Under such conditions, image contrast is primarily caused by the Laplacian of small height or potential variations across a sample surface. This contrast is blurred due to the interaction of the electrons with the electrical potential away from the surface. However, the method facilitates the rapid and intuitive interpretation of image contrast in terms of surface topographic or potential variations.

The approach can be readily extended to include spherical and chromatic aberration. Finally, we have demonstrated that the Laplacian imaging theory forms a convenient basis for the solution of the inverse problem in MEM.

We are grateful to Rod Mackie for technical support. S.M.K. acknowledges funding from the J. L. William Bequest. D.M.P., W.X.T. and D.E.J. acknowledge funding from the Australian Research Council.

## References

- Abramowitz, M. & Stegun, I. A. 1964 *Handbook of mathematical functions with formulas, graphs, and mathematical tables*, second printing, Ch. 17, pp. 589–592, Washington: United States Department of Commerce and National Bureau of Standards (also available online).
- Barnett, M. E. & Nixon, W. C. 1967a A mirror electron microscope using magnetic lenses *J. Sci. Instrum.* **44**, 893–897. (DOI 10.1088/0950-7671/44/11/302).
- Barnett, M. E. & Nixon, W. C. 1967b Electrical contrast in mirror electron microscopy *Optik* **26**, 310–325.
- Bauer, E. 1985 The resolution of the low energy electron reflection microscope *Ultramicroscopy* **17** 51–56. (DOI 10.1016/0304-3991(85)90176-7).
- Bauer, E. 1994 Low energy electron microscopy *Rep. Prog. Phys.* **57** 895–938. (DOI 10.1088/0034-4885/57/9/002).
- Bauer, E. 1998 LEEM basics *Surf. Rev. Lett.* **5** 1275–1286. (DOI 10.1142/S0218625X98001614).
- Berry, M. V. 2006 Oriental magic mirrors and the Laplacian image *Eur. J. Phys.* **27** 109–118. (DOI 10.1088/0143-0807/27/1/012).
- Bok, A. B. 1978 Mirror electron microscopy theory and applications. In *Diffraction and imaging techniques in material science* (eds S. Amelinckx, R. Gevers & J. Van Landuyt), 2nd rev. edn., pp. 761–788, Amsterdam: North-Holland.
- Borwein, J. M. & Borwein, P. B. 1987 *Pi and the AGM, a study in analytic number theory and computational complexity*, vol. 4, pp. 7–9, New York: John Wiley & Sons.
- Boudjelkha, M. T. & Diaz, J. B. 1972 Half space and quarter space Dirichlet problems for the partial differential equation *Applicable Analysis* **1** 297–324. (DOI 10.1080/00036817208839020).
- Cowley, J. M. 1995 *Diffraction physics*, 3rd rev. edn., pp. 26–35, 59–63, Amsterdam: North-Holland.
- Dyukov, V. G., Nepijko, S. A. & Sedov, N. N. 1991 *Electron microscopy of local potentials*, pp. 10–12, 28–35, 45–51, 63–66, 73–76, Kiev: Naukova Dumka (in Russian).
- Fejes, P. L. 1977 Approximations for the calculation of high-resolution electron-microscope images of thin films *Acta Cryst.* **A33** 109–113. (DOI 10.1107/S0567739477000230).
- Godehardt, R. 1995 Mirror electron microscopy *Adv. Imag. Elect. Phys.* **94** 81–150. (DOI 10.1016/S1076-5670(08)70144-7).
- Grant, I. S. & Phillips, W. R. 1990 *Electromagnetism*, 2nd edn., pp. 100–103, Chichester: John Wiley & Sons.
- Gureyev, T. E. & Nugent, K. A. 1997 Rapid quantitative phase imaging using the transport of intensity equation *Opt. Commun.* **133** 339–346. (DOI 10.1016/S0030-4018(96)00454-3).
- Hermans, A. J. & Petterson, J. A. 1970 A quantum mechanical treatment of the mirror electron microscope *J. Eng. Math.* **4** 141–154. (DOI 10.1007/BF01535086).
- Jesson, D. E., Pavlov, K. M., Morgan, M. J. & Usher, B. F. 2007 Imaging surface topography using Lloyd’s mirror in photoemission electron microscopy *Phys. Rev. Lett.* **99** 016103. (DOI 10.1103/PhysRevLett.99.016103).
- Kennedy, S. M., Jesson, D. E., Morgan, M. J., Smith, A. E. & Barker, P. F. 2006 Phase sensitivity of slow electrons to interactions with weak potentials *Phys. Rev. A* **74** 044701. (DOI 10.1103/PhysRevA.74.044701).
- Luk’yanov, A. E., Spivak, G. V. & Gvozdover, R. S. 1974 Mirror electron microscopy *Sov. Phys. Usp.* **16** 529–552. (DOI 10.1070/PU1974v016n04ABEH005299).
- Lynch, D. F., Moodie, A. F. & O’Keefe, M. A. 1975 n-beam lattice images. V. The use of the charge-density approximation in the interpretation of lattice images *Acta Cryst.* **A31** 300–307. (DOI 10.1107/S0567739475000642).
- Nepijko, S. A. & Schönhense, G. 2010 Measurement of potential distribution function on object surface by using an electron microscope in the mirror operation mode *J. Microsc.* **238** 90–94. (DOI 10.1111/j.1365-2818.2009.03340.x).

- Nepijko, S. A. & Sedov, N. N. 1997 Aspects of mirror electron microscopy *Adv. Imag. Elect. Phys.* **102** 273–323. (DOI 10.1016/S1076-5670(08)70125-3).
- Nepijko, S. A., Sedov, N. N., Schmidt, O., Schönhense, G., Bao, X. & Huang, W. 2001a Imaging of three-dimensional objects in emission electron microscopy *J. Microsc.* **202** 480–487. (DOI 10.1046/j.1365-2818.2001.00846.x).
- Nepijko, S. A., Sedov, N. N. & Schönhense, G. 2001b Peculiarities of imaging one- and two-dimensional structures using an electron microscope in the mirror operation mode *J. Microsc.* **203** 269–276. (DOI 10.1046/j.1365-2818.2001.00895.x).
- Nepijko, S. A., Gloskovskii, A., Sedov, N. N. & Schönhense, G. 2003 Measurement of the electric field distribution and potentials on the object surface in an emission electron microscope without restriction of the electron beams *J. Microsc.* **211** 89–94. (DOI 10.1046/j.1365-2818.2003.01199.x).
- Nepijko, S. A., Marx, G. K. L. & Schönhense, G. 2007 Quantitative determination of magnetic fields on object surfaces via photoemission electron microscopy without restriction of the electron beam *Nucl. Instr. and Meth. in Phys. Res. B* **264** 194–200. (DOI 10.1016/j.nimb.2007.08.076).
- Paganin, D. M. & Nugent, K. A. 1998 Noninterferometric phase imaging with partially coherent light *Phys. Rev. Lett.* **80** 2586–2589. (DOI 10.1103/PhysRevLett.80.2586).
- Paganin, D. M. 2006 *Coherent X-ray optics*, pp. 278–284, 295–301, 395–396, New York: Oxford University Press.
- Polozhiy, G. N. 1967 *Equations of mathematical physics*, pp. 62–64, 149, New York: Hayden Book Company.
- Press, W. H., Teukolsky, S. A., Vetterling, W. T. & Flannery, B. P. 2007 *Numerical recipes, the art of scientific computing*, 3rd edn., pp. 600–604, Cambridge: Cambridge University Press.
- Rempfer, G. F. & Griffith, O. H. 1992 Emission microscopy and related techniques: resolution in photoelectron microscopy, low energy electron microscopy and mirror electron microscopy *Ultramicroscopy* **47** 35–54. (DOI 10.1016/0304-3991(92)90184-L).
- Riesz, F. 2000 Geometrical optical model of the image formation in Makyoh (magic-mirror) topography *J. Phys. D: Appl. Phys.* **33** 3033–3040. (DOI 10.1088/0022-3727/33/23/305).
- Sedov, N. N. 1970 Théorie quantitative des systèmes en microscopie électronique à balayage, à miroir et à émission. *J. Microscopie* **9** 1–26.
- Slezák, J., Ondřejček, M., Chvoj, Z., Cháb, V., Conrad, H., Heun, S., Schmidt, Th., Ressel, B. & Prince, K. C. 2000 Surface diffusion of Au on Si(111): a microscopic study *Phys. Rev. B* **61** 16121–16128. (DOI 10.1103/PhysRevB.61.16121).
- Shimakura, T., Takahashi, Y., Sugaya, M., Ohnishi, T., Hasegawa, M., Ohta H. 2008 Mirror electron microscope for inspecting nanometer-sized defects in magnetic media *Microelectron. Eng.* **85** 1811–1814. (DOI 10.1016/j.mee.2008.05.018).
- Someya, T. & Kobayashi, J. 1974 Quantitative application of electron-mirror microscopy to the determination of pure shear of ferroelectric  $\text{Gd}_2(\text{MoO}_4)_3$  *Phys. Stat. Sol. (a)* **26** 325–336. (DOI 10.1002/pssa.2210260134).
- Speake, C. C. & Trenkel, C. 2003 Forces between conducting surfaces due to spatial variations of surface potential *Phys. Rev. Lett.* **90** 160403. (DOI 10.1103/PhysRevLett.90.160403).
- Spence, J. C. H. 2003 *High-resolution electron microscopy*, 3rd edn., Ch. 3, Oxford: Oxford University Press.
- Świąch, W., Rausenberger, B., Engel, W., Bradshaw, A. M. & Zeitler, E. 1993 In-situ studies of heterogeneous reactions using mirror electron microscopy *Surf. Sci.* **294** 297–307. (DOI 10.1016/0039-6028(93)90116-2).
- Tang, W. X., Jesson, D. E., Pavlov, K. M., Morgan, M. J. & Usher, B. F. 2009 Ga droplet morphology on GaAs(001) studied by Lloyd’s mirror photoemission electron microscopy *J. Phys.: Condens. Matter* **21** 314022. (DOI 10.1088/0953-8984/21/31/314022).
- M. R. 1983 Deterministic phase retrieval: a Green’s function solution *J. Opt. Soc. Am.* **73** 1434–1441. (DOI 10.1364/JOSA.73.001434).
- Tersoff, J., Jesson, D. E. & Tang W. X. 2009 Running droplets of Ga from evaporation of GaAs *Science* **324** 236–238. (DOI 10.1126/science.1169546).
- Yu, R. P., Kennedy, S. M., Paganin, D. M. & Jesson, D. E. 2010 Phase retrieval low energy electron microscopy *Micron* **41** 232–238. (DOI 10.1016/j.micron.2009.10.010).

## 2.1 Addendum for chromatic aberration, the inclusion of the magnetic objective lens effect

In addition to including the chromatic aberration of the immersion lens in Laplacian imaging theory, via Eqs. (6.5)–(6.8) in this chapter, we may also include the chromatic aberration due to the magnetic objective lens. This results from the variation in focus condition experienced by electrons of varying energy in the magnetic field. While we found that this effect was typically smaller than the chromatic aberration of the immersion lens for the cases in this chapter, at high resolution it may become important to include the magnetic component of chromatic aberration as well.

As per chapter 4, the magnetic objective lens chromatic aberration can be incorporated by varying the defocus value as a function of energy, replacing the defocus  $\Delta f$  with  $\Delta f + \epsilon(\xi)$ , for

$$\epsilon(\xi) = -C_C \xi / U, \quad (2.1)$$

where  $C_C$  is the chromatic aberration coefficient and  $\xi$  is the energy variation from the average  $U$ . We may incorporate this additional change to the defocus in Eq. (6.7) of chapter 2, by first noting that the turning distance, Eq. (6.5) of chapter 2,

$$\delta = L \left( 1 + \frac{U + \xi}{eV} \right), \quad (2.2)$$

can be rearranged as

$$\xi = eV \left( \frac{\delta}{L} - 1 \right) - U. \quad (2.3)$$

Substituting Eq. (2.3) into Eq. (2.1) we may express  $\epsilon$  as a function of turning distance  $\delta$ ,

$$\epsilon(\delta) = C_C \left( 1 + \frac{eV}{U} \left( 1 - \frac{\delta}{L} \right) \right). \quad (2.4)$$

We may then replace  $\Delta f$  in Eq. (6.7) of chapter 2 with  $\Delta f + \epsilon(\delta)$ , and carry out the integration in  $\delta$  as normal to obtain the complete chromatically averaged blurring function  $B_C$ . This extension, using Eq. (6) of chapter 4 and Rempfer and Griffith (1992) to give  $C_C = 0.03875$  m, did not change the result in chapter 2, i.e. including chromatic aberration had a very small effect ( $< 1\%$ ) on the simulations performed.

## 2.2 Addendum for parallel illumination

In chapter 2 a Laplacian imaging theory was developed for divergent sample illumination geometry, as considered by authors Luk'yanov et al. (1974); Dyukov et al. (1991); Godehardt (1995); Nepijko and Sedov (1997); Nepijko et al. (2001a,b, 2003, 2007); Nepijko and Schönhense (2010). However, in a modern low energy electron microscope (LEEM), equipped with a magnetic objective lens, the sample is often illuminated by a parallel, collimated beam (Altman, 2010; Tromp et al., 2010). Here, we briefly develop the Laplacian imaging theory for this parallel illumination geometry.

In Fig. 2.1 below, the incident electron beam for  $z < 0$  is converging, directed towards the  $z$  axis to the point  $z = 4L_M$ . The anode aperture acts as a diverging lens with focal length  $f = -4L_M$ , so the electron paths passing through the aperture are deflected and emerge parallel to the  $z$  axis for  $z > 0$ , illuminating the specimen surface with a parallel electron beam.

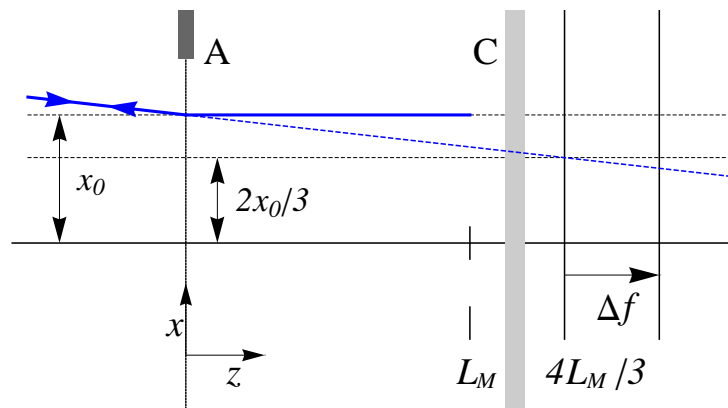


Figure 2.1: Formation of the virtual image plane at  $z = 4L_M/3$  for a flat, equipotential cathode specimen. An electron trajectory directed towards the point  $(x = 0, z = 4L_M)$  is deflected when passing through the anode aperture, emerging parallel to the  $z$  axis. After turning in the vicinity of  $(x = x_0, z = L_M)$ , the returning electron passes back through the anode aperture and is again deflected away from the  $z$  axis. The apparent straight line path of the exiting electron is traced back to the virtual image plane in the vicinity of  $z = 4L_M/3$ , with transverse distance  $x = 2x_0/3$ . The  $y$  axis extends out of the page. Based on Fig. 2 of Kennedy et al. (2011).

As seen in Fig. 2.1, the unperturbed electron path that passes through the anode aperture at  $(x_0, y_0, 0)$  remains parallel to the  $z$  axis, turning around in the vicinity of the point  $(x_0, y_0, L_M)$ . It then retraces the incident ray's path, emerging from the anode aperture making the angle  $x_0/4L_M$  to the  $z$  axis in

the  $x$  direction, and  $y_0/4L_M$  in  $y$ . We trace back along the apparent straight line path of the emerging electron to the virtual image plane at  $z = \Delta f + 4L_M/3$  as before, which has a magnification  $M$  of

$$M(\Delta f) = \frac{2}{3} \left( 1 - \frac{3\Delta f}{8L_M} \right), \quad (2.5)$$

compared to the specimen surface.

The analysis proceeds as per Eqs. (2.1)-(2.4) of chapter 2, where an additional potential  $V(x, y, \bar{z})$  is introduced due to a surface height variation  $H$ ,

$$V(x, y, \bar{z}) = \frac{\bar{z}V}{2\pi L} H(x, y) \otimes (x^2 + y^2 + \bar{z}^2)^{-3/2}. \quad (2.6)$$

As per section 2 of chapter 2, we assume that any change to the electron motion caused by  $H$  occurs very close to the sample surface. In addition, the motion in the  $z$  dimension is assumed to be unchanged, so that all of the momentum change in the transverse dimensions ( $x, y$ ) occurs very close to the classical turning point at  $z = L_M$ . This is a column approximation, whereby an electron passing through the anode at  $(x_0, y_0)$  is affected most strongly by the cathode at  $(x_0, y_0)$ , as this is the point at which the unperturbed path (Fig. 2.1) is closest to the specimen surface. Note that this is different to the column  $(3x_0/2, 3y_0/2)$  used previously in chapter 2.

The transverse shifts on the virtual imaging plane at  $z = \Delta f + 4L_M/3$  are given by scaling the difference between perturbed and unperturbed positions on the imaging plane by the magnification  $M$ , resulting in

$$S_x(x, y, \delta, \Delta f) = (\partial/\partial x) \frac{\sqrt{L_M}}{\pi} \frac{18\Delta f}{16L_M - 6\Delta f} H(x, y) \otimes ((\delta^2 + x^2 + y^2)^{-3/4} (2E_E(x, y, \delta) - E_K(x, y, \delta))), \quad (2.7)$$

and

$$S_y(x, y, \delta, \Delta f) = (\partial/\partial y) \frac{\sqrt{L_M}}{\pi} \frac{18\Delta f}{16L_M - 6\Delta f} H(x, y) \otimes ((\delta^2 + x^2 + y^2)^{-3/4} (2E_E(x, y, \delta) - E_K(x, y, \delta))). \quad (2.8)$$

As before,

$$E_E(x, y, \delta) = E \left( \frac{1}{2} - \frac{\delta}{2(\delta^2 + x^2 + y^2)^{1/2}} \right), \quad E_K(x, y, \delta) = K \left( \frac{1}{2} - \frac{\delta}{2(\delta^2 + x^2 + y^2)^{1/2}} \right), \quad (2.9)$$

and  $K, E$  respectively denote complete elliptic integrals of the first and second kind (Abramowitz and Stegun, 1964; Borwein and Borwein, 1987). These differ from Eqs. (2.5) and (2.6) of chapter 2 only in that the term

$9\Delta f/(8L_M - 6\Delta f)$  has been replaced by  $18\Delta f/(16L_M - 6\Delta f)$ . Thus for defocus  $|\Delta f| \ll 16L_M/6$ , these shifts and the resulting expressions are negligibly affected by the change in MEM geometry. We may quantify the difference between the two terms by taking the binomial approximation of each for  $6\Delta f/16L_M \ll 1$ , and subtracting the two expressions, giving a difference of

$$D(\Delta f) \approx \frac{27\Delta f^2}{64L_M^2} + O(\Delta f^3), \quad (2.10)$$

where  $O(\Delta f^3)$  contains terms involving  $\Delta f^3$  and higher order. For the defocus values and parameters used in chapter 2, the change to the shift functions, the blurring function and the resulting images is  $< 1\%$ , so the results and conclusions of chapter 2 remain valid for the parallel illumination geometry.

For completeness, we update the relevant expressions of chapter 2 for parallel illumination geometry. The blurred height  $H_B$  of Eq. (2.9) becomes

$$H_B(x, y, \delta, \Delta f) = \frac{\Delta f}{8L_M - 3\Delta f} H(x, y) \otimes B(x, y, \delta), \quad (2.11)$$

with blurring function (Eq. (2.10))

$$B(x, y, \delta) = \frac{18\sqrt{L_M}}{2\pi} (\delta^2 + x^2 + y^2)^{-3/4} (2E_E(x, y, \delta) - E_K(x, y, \delta)). \quad (2.12)$$

The maximum defocus condition of Eq. (3.3) is now

$$|\Delta f| \ll 8L_M / (3 + \max_{x,y} |\nabla_{\perp}^2 H(x, y) \otimes B(x, y, \delta)|), \quad (2.13)$$

and the approximate MEM image intensity (Eq. (3.7)) is given by

$$I(x, y, \delta, \Delta f) \approx 1 - \Delta f \nabla_{\perp}^2 H(x, y) \otimes \frac{B(x, y, \delta)}{8L_M}. \quad (2.14)$$

Finally, the chromatically averaged blurring function of Eq. (6.7) is now

$$B_C(x, y, \delta_0, \Delta f) = \int \frac{\sqrt{L - \delta}}{\pi} \frac{18(\Delta f + 2(\delta - \delta_0))}{16(L - \delta) - 6(\Delta f + 2(\delta - \delta_0))} (\delta^2 + x^2 + y^2)^{-3/4} \\ \times (2E_E(x, y, \delta) - E_K(x, y, \delta)) D(\delta) d\delta. \quad (2.15)$$

under the parallel illumination geometry.



---

## Caustic imaging of gallium droplets using MEM

This chapter is an author generated pre print of the article

S. M. Kennedy, C. X. Zheng, W. X. Tang, D. M. Paganin, and D. E. Jesson, 'Caustic imaging of gallium droplets using mirror electron microscopy,' *Ultramicroscopy*, **111** (2011) 356–363, available electronically at <http://www.elsevier.com/locate/ultramic> or via doi:10.1016/j.ultramic.2011.01.019.



### Declaration for thesis chapter 'Caustic imaging of Gallium droplets using mirror electron microscopy.'

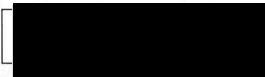
#### Declaration by candidate

For this chapter, the nature and extent of my contribution to the work was the following:

Nature of contribution	Extent of contribution (%)
Developed the model used in the paper, performed the image simulations, co-wrote the paper.	70

The following co-authors contributed to the work. Co-authors who are students at Monash University must also indicate the extent of their contribution in percentage terms:

Name	Nature of contribution	Extent of contribution (%) for student co-authors only
Changxi Zheng	Provided experimental images, both AFM and MEM, and provided technical expertise.	25
Wen-Xin Tang	Provided technical expertise.	
David Paganin	Co-wrote, helped develop the model and provided technical expertise.	
David Jesson	Co-wrote, helped develop the model and provided technical expertise.	

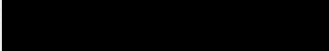
Candidate's Signature		Date 25/8/10
-----------------------	---	--------------

#### Declaration by co-authors

The undersigned hereby certify that:

- (1) the above declaration correctly reflects the nature and extent of the candidate's contribution to this work, and the nature of the contribution of each of the co-authors.
- (2) they meet the criteria for authorship in that they have participated in the conception, execution, or interpretation, of at least that part of the publication in their field of expertise;
- (3) they take public responsibility for their part of the publication, except for the responsible author who accepts overall responsibility for the publication;
- (4) there are no other authors of the publication according to these criteria;
- (5) potential conflicts of interest have been disclosed to (a) granting bodies, (b) the editor or publisher of journals or other publications, and (c) the head of the responsible academic unit; and
- (6) the original data are stored at the following location(s) and will be held for at least five years from the date indicated below:

Location(s)

Signature 1		Date 26/08/10
Signature 2		25/08/10
Signature 3		26/08/2010
Signature 4		26-8-10



# Caustic imaging of gallium droplets using mirror electron microscopy

S. M. Kennedy, C. X. Zheng, W. X. Tang, D. M. Paganin and D. E. Jesson<sup>1</sup>

*School of Physics, Monash University, Victoria, 3800, Australia*

---

## Abstract

We discuss a new interpretation of mirror electron microscopy (MEM) images, whereby electric field distortions caused by surface topography and/or potential variations are sufficiently large to create caustics in the image contrast. Using a ray-based trajectory method, we consider how a family of rays overlaps to create caustics in the vicinity of the imaging plane of the magnetic objective lens. Such image caustics contain useful information on the surface topography and/or potential, and can be directly related to surface features. Specifically we show how a through-focus series of MEM images can be used to extract the contact angle of a Ga droplet on a GaAs (001) surface.

*Keywords:* Mirror electron microscopy (MEM), caustic imaging, Ga droplets, GaAs, contact angle

---

## 1. Introduction

Mirror electron microscopy (MEM) is a well-established technique for imaging surface phenomena in real time, with applications in studying electric field contrast [1–6], droplet surface dynamics [7–9], surface magnetic fields [10], and chemical processes at solid surfaces [11]. The importance of understanding *in situ* dynamical behaviour and surface evolution under technologically important conditions makes the interpretation of MEM images an important avenue of investigation. In MEM, electrons neither touch nor are emitted from the sample. Instead a normally incident electron beam is reflected just above the specimen surface, as a result of the specimen

---

<sup>1</sup>david.jesson@monash.edu

voltage being tuned to be slightly more negative than that of the electron source. In the turn-around region, the slow moving electrons are sensitive to spatial and/or temporal variations in the electric field and are deflected, creating image contrast in the reflected beam. Such variations in the electric field may, for example, be caused by the surface topography [12–15] and/or variations in the electric potential of the specimen, which includes contact potentials, surface charges and varying conductivity [1–3, 6, 10, 11, 16].

The returning electron beam therefore contains information on the electric field variations caused by surface topography and/or electrical and magnetic phenomena. This has stimulated numerous efforts to interpret MEM image contrast and extract quantitative information regarding electric field variations and surface properties. A variety of approaches have been employed, some based on wave mechanics [17, 18], but most have been based on geometrical ray tracing techniques [1, 2, 11, 14, 16, 19–24]. For small surface variations and/or small defocus, it has recently been shown that MEM image contrast can be intuitively and rapidly interpreted as the Laplacian or curvature of a blurred surface height function [25].

Large variations in surface height or potential are, however, capable of deflecting the electron trajectories so much that very strong image contrast is created including caustic features [1, 19, 26, 27]. Such deflections typically violate the assumptions underlying many of the previous approaches, which assume that the  $z$  motion of the electron beam (i.e. along the optical axis) is largely unchanged by the surface height or potential variations [6, 14, 19, 20, 24, 25]. Approaches allowing for strongly deflected electron trajectories have, to date, only been solvable for specific analytical cases [14, 20]. Here we present a general ray-based method of interpreting MEM image contrast using a family or envelope of incident electron rays traced through the electric field close to the specimen surface. This approach is similar to the methods employed by Kan and Phaneuf [13]. Where strong deflections occur, ray trajectories crossing a caustic surface are observed, which can be directly related to variations in the field above the surface. This specifically allows for the simulation and interpretation of MEM image contrast in the presence of stronger field variations than has previously been possible.

## 2. MEM imaging geometry

A typical electrostatic MEM immersion lens is shown schematically in Fig. 1. Electrons of initial energy  $U$  travel along the optical axis  $z$  of the im-

immersion lens, pass through the anode aperture A, and are reflected in the vicinity of  $z = L_M$ , a distance of  $\delta$  above the specimen surface C. The specimen, located a distance of  $L$  from the anode, acts as the cathode of the immersion objective lens [1, 2, 16, 25, 28, 29], and is held at a negative potential  $V < -U/e < 0$  relative to the grounded anode, where  $-e$  is the electronic charge.

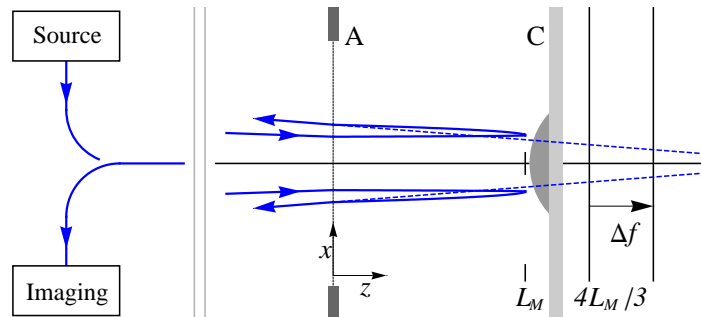


Figure 1: MEM imaging geometry. An electron beam of energy  $U$  is focused by the magnetic objective lens to a cross-over point ( $x = 0, z = 4L_M$ ). The anode aperture A acts as a diverging lens, deflecting the electron trajectories away from the  $z$  axis as they enter and leave. The cathode C is set at the potential  $V < -U/e < 0$  so that the electron beam turns around in the vicinity of  $z = L_M$ , where it is sensitive to deviations in the electric field due to surface and/or potential variations of the cathode. We trace the exiting electron trajectories back along the apparent straight line paths to the virtual image plane at  $z = \Delta f + 4L_M/3$ . This is the object plane for the magnetic objective lens. The  $y$  axis extends out of the page.

The magnetic imaging part of the objective lens can, to a good approximation, be considered separately to the electrostatic MEM immersion lens of Fig. 1 [28, 29]. Following reflection, the returning electron beam is further deflected by the anode aperture which acts as a diverging lens [20, 22, 25, 30]. On retracing back along the apparent straight line paths of the exiting electron trajectories it can be seen that a virtual image is formed on a plane at  $z = \Delta f + 4L_M/3$ . This is the object plane of the magnetic objective lens defocused by  $\Delta f$ , which is defined as positive in the positive  $z$  direction, and where  $L_M$  is given by

$$L_M = -LU/eV = L - \delta. \quad (1)$$

As shown in Fig. 2, the incident electron beam is focused on the point  $z = 4L_M$  by the magnetic objective lens. However, the anode aperture

acts as a diverging lens providing parallel illumination of the sample. For the perfectly flat and equipotential specimen of Fig. 2, the electron beam remains parallel to the  $z$  axis at the transverse distance of  $x = x_0$ . After turning in the vicinity of  $z = L_M$ , the returning electron beam is deflected away from the  $z$  axis as it passes back through the anode aperture, and travels along the same trajectory as the incident beam. We trace the apparent straight line path of the emerging electron beam back to the virtual image plane in the vicinity of  $z = 4L_M/3$ . At this plane, an electron that interacted with the potential above the cathode surface at  $x = x_0$  appears on the virtual image plane at  $2x_0/3$ , so the virtual image must have transverse distances scaled by  $3/2$  to return to the scale of the specimen.

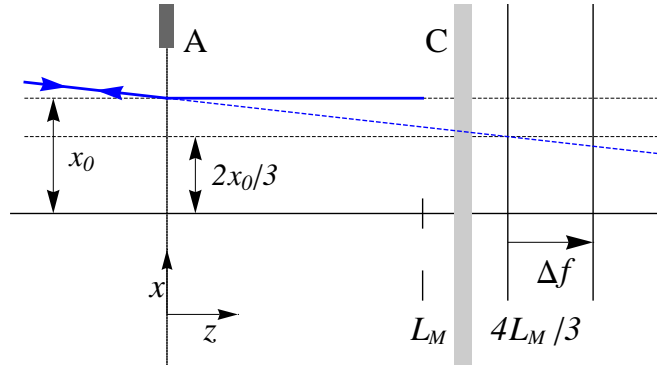


Figure 2: Formation of the virtual image plane at  $z = 4L_M/3$  for an unperturbed cathode specimen. An electron trajectory directed towards the point  $(x = 0, z = 4L_M)$  is deflected when passing through the anode aperture, emerging parallel to the  $z$  axis. After turning in the vicinity of the point  $(x = x_0, z = L_M)$ , the returning electron is again deflected away from the  $z$  axis. The apparent straight line path of the exiting electron is traced back to the virtual image plane in the vicinity of  $z = 4L_M/3$ , with transverse distance  $2x_0/3$ . The  $y$  axis extends out of the page.

### 3. Evaluation of the electric potential above the specimen surface

To calculate the distribution of electron positions on the image plane  $z = \Delta f + 4L_M/3$ , we must first solve Laplace's equation for the electric potential  $\phi(r, \theta, z)$  in the region  $0 \leq z \leq L$ . In cylindrical coordinates  $r, \theta, z$ , this is given by [31]

$$\nabla^2 \phi = \frac{1}{r} \frac{\partial}{\partial r} \left( r \frac{\partial \phi}{\partial r} \right) + \frac{1}{r^2} \frac{\partial^2 \phi}{\partial \theta^2} + \frac{\partial^2 \phi}{\partial z^2} = 0. \quad (2)$$

For an equipotential flat specimen surface, there is no  $r$  or  $\theta$  dependence and the solution of Eq. (2) is approximately

$$\phi_U(z) = Vz/L, \quad 0 \leq z \leq L, \quad (3)$$

where the penetration of the electric field through the anode aperture is approximated by treating the aperture as a thin diverging lens [20, 22, 25, 30]. For spatial variations in surface topography and/or potential the solution of Eq. (2) is necessarily more complex. In limited cases, analytical solutions can be found [20]. Additionally, for surface potential variations, and for sufficiently small variations in topography, the system can be reduced to the equivalent Dirichlet problem for Laplace's equation for a half space, facilitating the calculation of  $\phi(r, \theta, z)$  [20, 25, 32–35]. However, this latter approach breaks down when surface topographical variations are large enough to appreciably move the electron turn-around region (i.e. by many times the unperturbed turning distance  $\delta$  from the specimen).

In general it is necessary to solve Eq. (2) numerically. Many authors use charge-ring techniques [36–38], but here we employ standard finite element methods, using the specimen topography as one boundary (either equipotential or with a variable surface potential) and the grounded anode as the opposite boundary. Our simulations utilise the finite element methods package FreeFem++ v3.9-0 [39], with mesh adaptation. We consider the specific case of a cylindrically symmetrical electric potential,  $\phi(r, z)$ , so we need only consider the electric field in two dimensions. However, the method is readily extendable to three dimensions with a corresponding increase in complexity and computation time.

#### 4. Caustic image simulations

With knowledge of the electric potential in the region  $0 \leq z \leq L$ , we can evaluate the electron trajectories through this region and project them back onto the virtual image plane at  $z = \Delta f + 4L_M/3$ . To this end, let  $(r^{(j)(t)}, z^{(j)(t)})$  and  $(v_r^{(j)(t)}, v_z^{(j)(t)})$  denote the respective position and velocity of the  $j$ th electron at time  $t$ . For the maximum velocities  $v_{max} \approx 0.28c$  m/s considered here, where  $c$  is the speed of light in vacuum, the Lorentz factor  $(1 - v_{max}^2/c^2)^{-1/2} \approx 1.04$  so we ignore relativistic corrections. At  $t = 0$  we input a family of electron ray trajectories at  $z = 0$ , which are equally spaced in the transverse dimension  $r$  by the distance  $r_0$ . The  $j$ th ray at

$t = 0$  begins at the point

$$(r^{(j)(0)}, z^{(j)(0)}) = (jr_0, 0), \quad (4)$$

with velocities  $(v_r^{(j)(0)}, v_z^{(j)(0)})$  in the  $r$  and  $z$  directions respectively. The initial velocity in  $z$  is set by the electron beam energy,

$$v_z^{(j)(0)} = \sqrt{2U/m}, \quad (5)$$

where  $m$  is the electron rest mass. The initial velocity in  $r$  is zero, as the electron trajectories at  $z = 0$  are parallel to the  $z$  axis after passing through the anode aperture that acts as a diverging lens with focal length  $-4L_M$  [20, 22, 25, 30], giving

$$v_r^{(j)(0)} = 0. \quad (6)$$

From these initial conditions we use a fourth order Runge–Kutta method to trace each trajectory through the electric potential, calculating the position and velocity for successive time steps of  $h$  [40]. Details of this procedure are provided in Appendix A, and are similar to the approach used in Kan and Phaneuf [13]. Eventually, the  $j$ th electron exits the immersion lens at position  $(r^{(j)(exit)}, 0)$  with velocities  $(v_r^{(j)(exit)}, v_z^{(j)(exit)})$ . We account for the anode aperture deflection and trace back along the apparent straight line path of the electron to the virtual image plane  $z = \Delta f + 4L_M/3$  (Figs. 1 and 2), giving the virtual position of the  $j$ th ray,

$$\left( r^{(j)(exit)} - \left( \Delta f + \frac{4L_M}{3} \right) \left( \frac{v_r^{(j)(exit)}}{-v_z^{(j)(exit)}} + \frac{r^{(j)(exit)}}{4L_M} \right), \Delta f + \frac{4L_M}{3} \right). \quad (7)$$

The family of ray trajectories from a flat equipotential (i.e. unperturbed) specimen surface exit the anode aperture equally spaced at position  $jr_0$ , and will maintain an equal spacing  $S(\Delta f)$  when traced back to the image plane, with

$$S(\Delta f) = r_0 \left( \frac{2}{3} - \frac{\Delta f}{4L_M} \right). \quad (8)$$

We may calculate the image intensity on the plane  $\Delta f + 4L_M/3$  by considering the density of rays on this plane. This is inversely proportional to the ray spacing in  $r$ ,  $s(r, \Delta f)$  [41], given by the difference between  $r$  positions of adjacent rays in Eq. (7). Assuming an input intensity of unity, a ray spacing of  $s(r, \Delta f) = S(\Delta f)$  gives unit intensity. We therefore convert the family of ray trajectories into an intensity at any position on the plane

$\Delta f + 4L_M/3$  by dividing the unperturbed ray separation  $S(\Delta f)$  by the distance between adjacent rays  $s(r, \Delta f)$ , so giving [41]

$$I(r, \Delta f) = S(\Delta f)/s(r, \Delta f). \quad (9)$$

The image intensity may then be expressed as a one-dimensional profile in  $r$ , or as a two-dimensional plot by exploiting the cylindrical symmetry. Where initially adjacent rays cross ( $s \rightarrow 0$ ) the intensity is theoretically infinite, but in practice this results in a region of very high intensity, creating caustic features in the image [26, 27, 42]. Caustic surfaces, most of which are stable with respect to perturbation, are envelopes of ray families that may be classified into a variety of equivalence classes [27, 43]. Numerically, we may account for crossing rays by choosing a threshold ray spacing, e.g.  $s(r, \Delta f) = 0.1S(\Delta f)$ , below which from Eq. (9) we keep  $I \approx 10$ . This is equivalent to specifying the saturation level of the detector.

## 5. Caustic imaging of Ga droplets on GaAs (001)

As a specific application of caustic imaging theory we investigate liquid Ga droplets on GaAs (001). Such droplets are formed during Langmuir evaporation [9] and exhibit droplet surface dynamics with an unusual temperature dependence [8]. In particular, Ga droplets move on the rough GaAs (001) surface and leave behind smooth trails, as shown by the room temperature atomic force microscope (AFM) image in Fig. 3. An experimental through-focus MEM image sequence obtained at 660 °C during Langmuir evaporation is shown in Fig. 4. We now separately remark on the image contrast of the trails and droplets.

(a) *Trails.* The AFM data indicates that the droplet trails are typically shallow (15 nm) with slowly varying edges, so that Laplacian imaging theory is applicable and the MEM contrast can be interpreted in terms of surface curvature [25]. Specifically, the Laplacian imaging theory states that the image contrast is proportional to both  $\Delta f$  and to the transverse Laplacian of the local height profile  $H(x, y)$ , providing that  $H(x, y)$  is sufficiently slowly varying and/or  $\Delta f$  is sufficiently small [25]. At exact focus ( $\Delta f = 0$ ) the trail contrast vanishes.

(b) *Droplets.* The droplets, however, typically extend  $0.3 \mu\text{m}$  from the surface, which is many times larger than a typical electron turning distance ( $\delta = 40 \text{ nm}$ ) from the cathode. This produces significant perturbations

of the electric field creating caustic features for a wide range of defocus values. At negative defocus the image consists of a bright caustic ring  $C_R$  bordering a dark central region (see [8]). For large positive defocus, a very bright central caustic region is visible. Close to  $\Delta f = 0$  there is still strong droplet contrast visible exhibiting a transition between the two extremes. This illustrates the breakdown of Laplacian imaging theory [25] and we therefore apply caustic imaging theory to understand droplet image contrast.

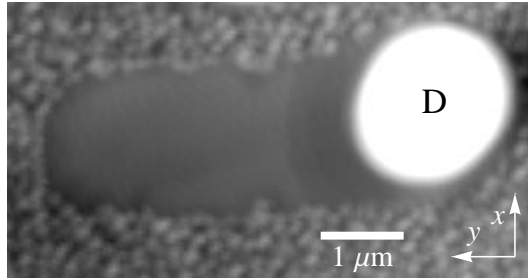


Figure 3: AFM image of a liquid Ga droplet D and the smooth trail it leaves on a GaAs (001) surface [25]. The shape of the droplet is well-approximated by a spherical cap.

## 6. Electric potential due to a liquid surface droplet

We evaluate the perturbing potential by modelling the droplet height  $H$  as a cylindrically symmetric spherical cap shown in Fig. 5, which is in good agreement with AFM measurements of solidified droplets (Fig. 3). This equilibrium shape is characterized by the projected radius  $R$  and the contact angle  $\Theta$ ,

$$H(0 \leq r \leq R) = \sqrt{\frac{R^2}{\sin^2 \Theta} - r^2} - \frac{R}{\tan \Theta}, \quad H(r > R) = 0, \quad (10)$$

as shown in Fig. 5. We use dimensions  $R = 0.78 \mu\text{m}$ ,  $\Theta = 36^\circ$  and  $H(0) = 0.25 \mu\text{m}$  for a typical droplet as imaged by AFM. Since the droplet consists of almost pure Ga, it may also be at a different potential to the GaAs (001) cathode, due to having a different surface work function [3, 44]. Massies *et al.* [44] indicate that the work function difference between the Ga droplet and the GaAs surface is in the range of 0.1 V to 0.3 V.

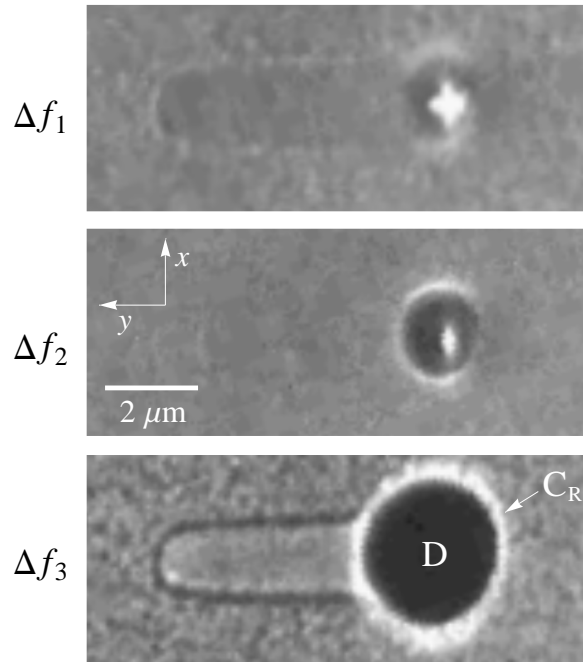


Figure 4: Experimental MEM images of a liquid Ga droplet marked D and the smooth trail it leaves on a GaAs (001) surface, for defoci  $\Delta f_1 = 16 \mu\text{m}$ ,  $\Delta f_2 = 0$ , and  $\Delta f_3 = -78 \mu\text{m}$ . Note the caustic ring  $C_R$  bordering a dark central region D in the bottom panel. Images were obtained using an Elmitec LEEM III system at  $660 \text{ }^\circ\text{C}$ .  $U = 20 \text{ keV}$  and  $V = -20000.4 \text{ V}$  which, for  $L = 2 \text{ mm}$ , gives a turning distance of  $\delta = 40 \text{ nm}$ .

We solve Laplace's equation (Eq. (2)) in the region  $0 \leq r \leq 100 \mu\text{m}$  and from  $L - 120 \mu\text{m} \leq z \leq L$  using the finite element methods package FreeFem++ v3.9-0 [39], using mesh adaptation with interpolation error level of  $5 \times 10^{-6}$  (see the end of Appendix A for a discussion on suitable computational parameters). The bottom boundary follows the height profile of Eq. (10) and has a potential of  $V = -20000.4 \text{ V}$  outside the droplet and  $-20000.7 \text{ V}$  at the droplet boundary to account for a work function difference of  $0.3 \text{ V}$ . The top boundary has the potential expected for the unperturbed potential (Eq. (3))  $\phi_U(z = L - 120 \mu\text{m}) = -18800.376 \text{ V}$  with  $L = 2 \text{ mm}$ . The  $r = 0$  and  $r = 100 \mu\text{m}$  boundaries are kept open, and the model assumes that the equipotential lines will be perpendicular to these boundaries. This ensures that the system is rotationally symmetric about the axis  $r = 0$ , and demands that the perturbations to the potential caused

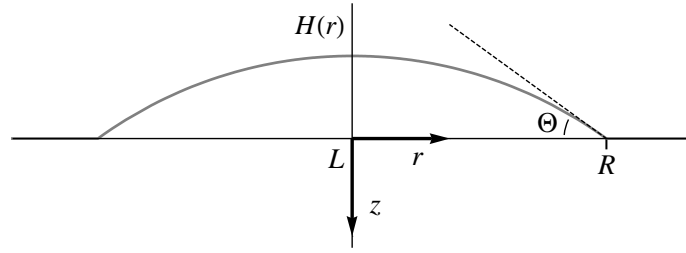


Figure 5: The droplet is modelled as a spherical cap (Eq. (10)), with projected radius  $R$  and contact angle  $\Theta$ .

by the droplet are zero at the chosen distance of  $r = 100 \mu\text{m}$ . The boundaries and mesh are shown in Fig. 6, and the resulting equipotential lines close to the droplet surface are shown in Fig. 7 for a work function of 0.3 V.

## 7. Caustic image simulation of a Ga droplet

To simulate the MEM contrast of a Ga droplet we employed the methods of section 4, inputting 201 rays at  $z = 0$  from  $r = 0 \mu\text{m}$  to  $r = 4.5 \mu\text{m}$  which gives an equal spacing of  $r_0 = 22.5 \text{ nm}$ . Using a fourth order Runge–Kutta method (Appendix A) with a sufficiently small time step of  $h = 5 \times 10^{-14} \text{ s}$ , we propagated each ray through the electric field, and then traced the exiting electron trajectories back along the apparent straight line paths to  $z = \Delta f + 4L_M/3$  using Eq. (7). The resulting distribution of electron ray trajectories is shown in Fig. 8 for  $-100 \mu\text{m} \leq \Delta f \leq 100 \mu\text{m}$ , where positive  $\Delta f$  is in the positive  $z$  direction (Fig. 1). Accompanying grey scale image simulations are shown for indicated defocus values.

The distribution of the envelope of electron ray trajectories and accompanying image simulations in Fig. 8 displays three distinct regimes of caustic features which accurately reproduce and explain the experimental through focus sequence in Fig. 4. For negative defocus, the contrast is dominated by a bright fold caustic ring  $C_R$  bordering a dark central region, with diameter increasing with negative defocus. For positive defocus, we expect a very bright central spot associated with the central cusp caustic evident in the ray tracing. For defocus values close to zero, we see a transition between the two extremes, where both a bright ring and bright central spot coexist. Note that the contrast close to zero defocus is not explainable

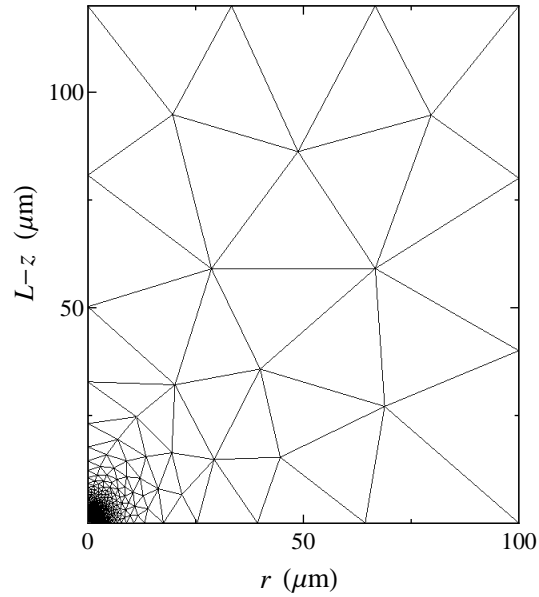


Figure 6: Boundaries and adapted mesh used to solve Laplace's equation (Eq. (2)) above the droplet surface with the FreeFem++ v3.9-0 package [39]. Note that the base of the droplet, as shown in Fig. 5, extends out to  $r = 0.78 \mu\text{m}$ .

with Laplacian imaging theory [25], which predicts zero image contrast. Caustic imaging theory may therefore be used to interpret and understand the image features of specimens that significantly perturb the electric field close to the sample. We now consider the potential utility of caustic imaging theory in recovering surface structural information from experimental MEM images.

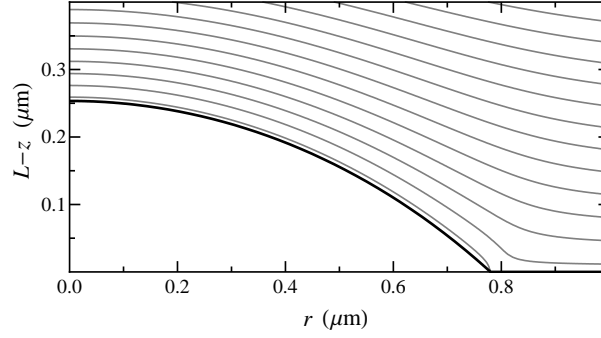


Figure 7: Equipotential surfaces above a Ga droplet on GaAs (001) evaluated from Eq. (2). A work function difference of 0.3 V exists between the droplet surface (black line) and the planar GaAs (001) surface ( $L-z = 0$  axis). The droplet and GaAs (001) surfaces are therefore at  $-20000.7$  V and  $-20000.4$  V respectively. Equipotential surfaces, beginning at  $-20000.6$  V and increasing by 0.3 V, are indicated by the grey lines.

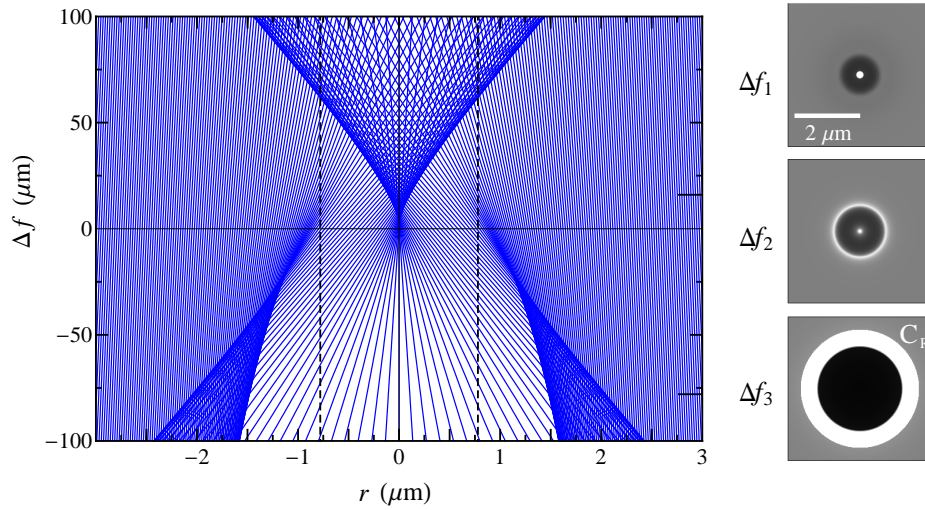


Figure 8: Distribution of the family of electron ray trajectories on the imaging plane  $z = \Delta f + 4L_M/3$ , after interaction with the electric field above a Ga droplet on GaAs (001) (solid lines). The defocus  $\Delta f$  is positive in the positive  $z$  direction (see Fig. 1). The  $r$  positions have been multiplied by  $3/2$  so that the virtual image plane matches the transverse scale of the specimen (see Fig. 2). The projected radius of the droplet,  $R = 0.78 \mu\text{m}$  is indicated by vertical dashed lines. (Right panels) two dimensional image simulations calculated from Eq. (9) are shown for  $\Delta f_1 = 16 \mu\text{m}$ ,  $\Delta f_2 = 0 \mu\text{m}$ , and  $\Delta f_3 = -78 \mu\text{m}$ , and show good agreement with the experimental images of Fig. 4. Color online.

## 8. Recovering surface topography from experimental MEM images

Caustic imaging theory provides a direct link between strong image features in experimental MEM images and the electric field distortions produced by specimen surface and/or potential variations. Understanding the “forward problem” of caustic formation allows one to broach the associated “inverse problem” of extracting structural information from the caustics present in a through-focus series of images. As a particular example of this inverse problem of caustic imaging, here we show how to determine the contact angle  $\Theta$  (Fig. 5) of a Ga droplet during Langmuir evaporation of GaAs (001).

As noted earlier, a running droplet of Ga leaves a shallow trail on GaAs (001) as shown in Fig. 3. We can apply Laplacian imaging theory [25] to the trail image contrast in Fig. 4 to estimate the trail width as  $1.56 \pm 0.02 \mu\text{m}$ . This utilises the approximately symmetrical change in the width of the trail contrast for defocus values close to and either side of zero, and therefore fixes the droplet projected radius  $R = 0.78 \pm 0.01 \mu\text{m}$ . We can also compare the features of the simulated trail contrast using caustic imaging theory to the MEM images to calibrate the relationship between the magnetic objective lens defocus and the lens current. The weaker contrast trail region therefore provides a useful reference to help quantify the droplet contrast. In general, however, there may not exist a convenient object for defocus calibration. In such cases, and as an alternative to the method outlined above, Schmidt *et al.* [45] have derived an expression relating defocus and experimental parameters including objective lens current.

Since the droplet has a spherical cap geometry, with  $R$  known, it is only necessary to determine  $\Theta$  to fully reconstruct the droplet shape. To determine the contact angle we select a caustic feature in the experimental images and compare this with simulation for a range of defocus values. The radius  $R_D$  of the dark central region bounded by the bright caustic in Fig. 9 is an excellent candidate since: (i) it is well defined, (ii) it is a sharp feature of intrinsically high visibility, and (iii) it varies monotonically with defocus in the range  $-140 \mu\text{m} < \Delta f < -30 \mu\text{m}$ .

Simulated values of  $R_D$  as a function of  $\Delta f$  are displayed in Fig. 10 for different values of contact angle. Here, we have assumed a work function difference of 0.3 V between the droplet and GaAs (001) surface. Exper-

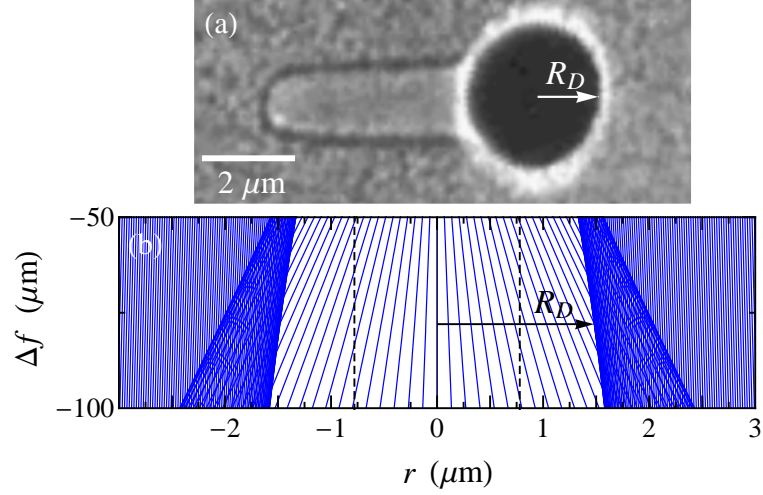


Figure 9: Radius of the dark central region bounded by the bright fold caustic,  $R_D$ , is shown on (a) an experimental MEM image and (b) a family of simulated rays. Colour online.

imental measurements of  $R_D$  are overlaid on this plot which fixes the contact angle to be  $38 \pm 3^\circ$ . This is in excellent agreement with the *ex situ* AFM measurement of  $36^\circ$  with standard deviation of  $2^\circ$  for typical Ga droplets, and demonstrates that caustic imaging can provide quantitative topographical data. Note that introducing a lower work function will affect the simulated  $R_D$  values and increase our estimate of  $\Theta$ . However, the maximum increase is only 4 degrees for the limiting case of zero work function difference. If the uncertainties are added in quadrature, we measure the contact angle to be  $38 \pm 7^\circ$ .

The effects of spherical aberration of the magnetic objective lens on the simulated images can be estimated using the exit angle of the electron,  $\alpha$ , as it emerges from the anode aperture. The tangent of this angle is given by

$$\tan \alpha = \frac{v_r^{(j)(exit)}}{-v_z^{(j)(exit)}} + \frac{r^{(j)(exit)}}{4L_M}, \quad (11)$$

using the terminology of Eq. (7). We estimate the change to the transverse

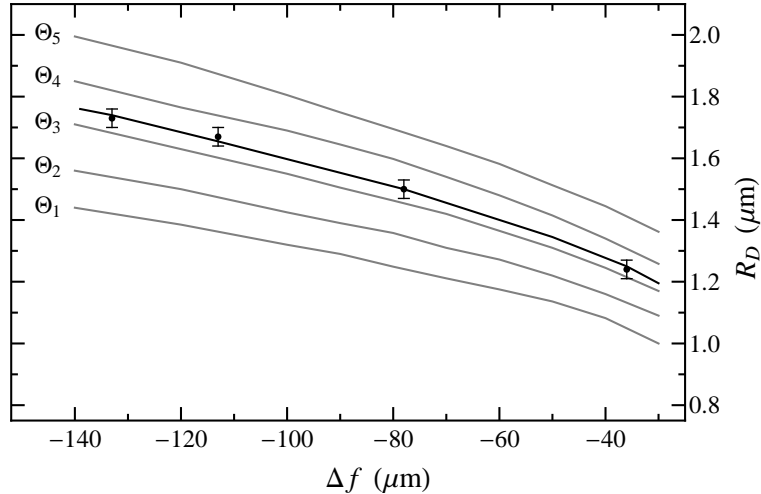


Figure 10: Simulated radius of the dark central region  $R_D$  for MEM images at negative defocus, for Ga droplets of projected radius  $0.78 \mu\text{m}$ , work function difference  $0.3 \text{ V}$ , and contact angles  $\Theta_1 = 15^\circ$ ,  $\Theta_2 = 25^\circ$ ,  $\Theta_3 = 35^\circ$ ,  $\Theta_4 = 45^\circ$ , and  $\Theta_5 = 55^\circ$  (grey lines). Measured experimental radius values, with uncertainty of  $\pm 0.03 \mu\text{m}$ , are overlaid and the line of best fit is shown as the black line.

position  $\Delta r$  of an electron in the vicinity of the virtual image plane  $z = 4L_M/3$  via [22, 46]

$$\Delta r = C_S \alpha^3, \quad (12)$$

where  $C_S$  is the spherical aberration coefficient. This can be directly incorporated into Eq. (7), by adding the approximate shift  $\Delta r$  to each ray's virtual position (Eq. (7)). We have simulated the ray envelope with  $C_S = 0.1 \text{ m}$  [22, 25, 45], and find that for the ray trajectories that determine the radius of the dark central region  $R_D$ , the change in position due to spherical aberration  $\Delta r$  is less than  $5 \text{ nm}$ , so spherical aberration for  $C_S \leq 0.1 \text{ m}$  has a negligible effect on the results of Fig. 10. The small number of rays with the largest angle  $\alpha$ , which determine the outer edge of the caustic ring  $C_R$  in Fig. 8, are estimated to be shifted by as much as  $50 \text{ nm}$ , but this does not affect the determination of the contact angle using the method outlined here. We may also include the effects of chromatic aberration by taking a weighted average of a series of monochromatic intensity patterns for a spread of energy values [25, 47]. For a Gaussian energy spread of full-width half-maximum  $0.3 \text{ eV}$ , we find that the effect on the image intensity for the low resolution case considered here is very small ( $< 1 \%$ ).

The capability to extract three-dimensional topographical or surface potential information from surface electron microscopy is extremely valuable. Experiments can be undertaken at elevated temperatures during material deposition under ultra high vacuum (UHV) conditions. Surface features such as contact angles can in principle be determined *in situ* from caustic features as a function of external conditions, provided the conditions do not vary rapidly on the time scale of a through-focus series which typically takes only a few seconds to acquire. By mapping several different caustic features as a function of defocus it should be possible to eliminate defocus entirely from the structure determination and/or extend the method to more complex geometries.

## 9. Multi-dimensional caustic imaging

We saw particular caustics in Fig. 8, namely cusp and fold caustics, fully unfolded [27] in a control space coordinatised by the transverse spatial coordinate  $r$  and a single control parameter  $\tau = \Delta f$ . More generally, one could have higher-dimensional caustics (e.g. the hyperbolic umbilic, the elliptic umbilic, the parabolic umbilic, etc. [43]). Since such higher-dimensional caustics require more than two dimensions for a full unfolding, the previously mentioned through-focal series  $I(r, \tau = \Delta f)$  might be replaced with the more general control-parameter series  $I(x, y, \tau_1, \tau_2, \dots)$ ; here  $(x, y)$  are Cartesian coordinates in the detector plane perpendicular to the optical axis  $z$ , and  $(\tau_1, \tau_2, \dots)$  denote a suitable set of continuously-variable control parameters such as defocus, cathode potential, electron energy, etc. For a given image series, the number of parameters in the set  $(x, y, \tau_1, \tau_2, \dots)$  will ideally be equal to the dimension of the space required for a full unfolding of the caustic being imaged.

Regarding the inverse problem, of determining surface structure from a given MEM caustic in the image series  $I(x, y, \tau_1, \tau_2, \dots)$ , the approach of Fig. 10 may be generalised as follows. Suppose one has an *a priori* model of the structure of interest (cf. Fig. 5), which is parameterized by a suitably small set of numbers  $(\Theta_1, \Theta_2, \dots)$ . Suppose, further, that in a given experiment one has measured the MEM caustic surfaces in  $I(x, y, \tau_1, \tau_2, \dots)$ . Importantly, such caustic surfaces are intrinsically of high visibility, and will therefore typically dominate image contrast. Under a suitable error metric, let  $\mathcal{E}[(\Theta_1, \Theta_2, \dots); I(x, y, \tau_1, \tau_2, \dots)]$  denote the mismatch between

the measured MEM caustic surfaces in  $I(x, y, \tau_1, \tau_2, \dots)$ , and the caustic surfaces which result when one evaluates the forward problem for the specified model as a function of  $(\Theta_1, \Theta_2, \dots)$ . The inverse problem of caustic imaging is then reduced to the multi-dimensional optimisation problem of finding the particular set of parameters  $(\Theta_1, \Theta_2, \dots)$  which minimise  $\mathcal{E}$ . Many numerical algorithms exist for such a multi-dimensional optimisation problem, see for example Chapter 10 of Press *et al.* [40]. Note, moreover, that such optimisations might also be carried out over data spaces with dimension smaller than that required for a full caustic unfolding, a particular example of which was given in Fig. 10.

## 10. Conclusions

We have demonstrated that a caustic dominated imaging theory can be usefully applied to interpret MEM contrast from surface topography (and/or surface potential) variations which appreciably distort the electric field above the specimen surface. The method obtains the electric potential above the specimen by numerically solving Laplace's equation. A family of electron ray trajectories is then numerically propagated through the electric field close to the specimen surface to obtain the electron distribution in the objective lens image plane. The resulting contrast may include strong image features where one has envelopes of overlapping rays, evident as bright caustic regions. Such caustics can be related to the specimen topography and/or potential and may be used to recover quantitative surface topographical information.

## Acknowledgments

We are grateful to Rod Mackie for technical support. S.M.K. acknowledges funding from the J. L. William Bequest. D.M.P., W.X.T. and D.E.J. acknowledge funding from the Australian Research Council via the Discovery-Projects programme.

## Appendix A. Fourth order Runge–Kutta method

The fourth order Runge–Kutta method is one of several methods that may be used to evaluate the electron path through the electric field (see the discussion and references in [38, 40]). Assuming rotational symmetry in cylindrical polar coordinates, at time  $t$  the  $j$ th electron is at  $(r^{(j)(t)}, z^{(j)(t)})$  with velocity  $(v_r^{(j)(t)}, v_z^{(j)(t)})$ . We estimate the new electron location and

velocity at time  $t + h$  using classical kinematic equations of motion. The fourth order Runge–Kutta method in essence estimates the average velocity in  $r$  and  $z$  over the time interval from  $t$  to  $t + h$ , and then multiplies this average velocity by  $h$  to obtain the new position in  $r$  and  $z$ . In the  $r$  direction, for example, the equation of motion is

$$v_{r,f} = v_{r,i} + \Delta t a_{r,av}(r, z), \quad (\text{A.1})$$

where  $v_{r,f}$  is the final velocity,  $v_{r,i}$  is the initial velocity, the acceleration  $a_r$  is

$$a_r(r, z) = -\frac{e}{m} \frac{\partial \phi(r, z)}{\partial r}, \quad (\text{A.2})$$

and  $a_{r,av}$  is the average acceleration over the time interval  $\Delta t$ . Where the acceleration is constant at all points  $(r, z)$ , Eq. (A.1) is trivial to apply. However where  $a_r(r, z)$  and  $a_z(r, z)$  vary with  $(r, z)$ , we use the fourth order Runge–Kutta method to generate a series of estimates of the acceleration and velocity over the time from  $t$  to  $t + h$ ,

$$\begin{aligned} vr_1 &= v_r^{(j)(t)}, & vz_1 &= v_z^{(j)(t)}, \\ vr_2 &= v_r^{(j)(t)} + (h/2)(-e/m) \left[ \frac{\partial \phi(r, z)}{\partial r} \right]_{(r=r^{(j)(t)}+(h/2)vr_1, z=z^{(j)(t)}+(h/2)vz_1)}, \\ vz_2 &= v_z^{(j)(t)} + (h/2)(-e/m) \left[ \frac{\partial \phi(r, z)}{\partial z} \right]_{(r=r^{(j)(t)}+(h/2)vr_1, z=z^{(j)(t)}+(h/2)vz_1)}, \\ vr_3 &= v_r^{(j)(t)} + (h/2)(-e/m) \left[ \frac{\partial \phi(r, z)}{\partial r} \right]_{(r=r^{(j)(t)}+(h/2)vr_2, z=z^{(j)(t)}+(h/2)vz_2)}, \\ vz_3 &= v_z^{(j)(t)} + (h/2)(-e/m) \left[ \frac{\partial \phi(r, z)}{\partial z} \right]_{(r=r^{(j)(t)}+(h/2)vr_2, z=z^{(j)(t)}+(h/2)vz_2)}, \\ vr_4 &= v_r^{(j)(t)} + h(-e/m) \left[ \frac{\partial \phi(r, z)}{\partial r} \right]_{(r=r^{(j)(t)}+hvr_3, z=z^{(j)(t)}+hvr_3)}, \\ vz_4 &= v_z^{(j)(t)} + h(-e/m) \left[ \frac{\partial \phi(r, z)}{\partial z} \right]_{(r=r^{(j)(t)}+hvr_3, z=z^{(j)(t)}+hvr_3)}, \\ r^{(j)(t+h)} &= r^{(j)(t)} + (h/6)(vr_1 + 2vr_2 + 2vr_3 + vr_4), \\ z^{(j)(t+h)} &= z^{(j)(t)} + (h/6)(vz_1 + 2vz_2 + 2vz_3 + vz_4). \end{aligned} \quad (\text{A.3})$$

Similarly, we may estimate the average acceleration over the time interval, and multiply this by  $h$  to obtain the new velocity in  $r$  and  $z$ . We use the classical kinematic equation of motion, in  $r$  for example,

$$r_f = r_i + v_{r,i}\Delta t + (a_{r,av}(r, z)/2)\Delta t^2, \quad (\text{A.4})$$

for final and initial points  $r_f$  and  $r_i$  respectively, to obtain the necessary points at which we evaluate the acceleration and obtain a weighted average,

$$\begin{aligned}
ar_1 &= (-e/m) \left[ \frac{\partial\phi(r,z)}{\partial r} \right]_{(r=r^{(j)}(t), z=z^{(j)}(t))}, \\
az_1 &= (-e/m) \left[ \frac{\partial\phi(r,z)}{\partial z} \right]_{(r=r^{(j)}(t), z=z^{(j)}(t))}, \\
ar_2 &= (-e/m) \left[ \frac{\partial\phi(r,z)}{\partial r} \right]_{(r=r^{(j)}(t) + (h/2)v_r^{(j)}(t) + (ar_1/2)(h/2)^2, \\
&\quad z=z^{(j)}(t) + (h/2)v_z^{(j)}(t) + (az_1/2)(h/2)^2)}, \\
az_2 &= (-e/m) \left[ \frac{\partial\phi(r,z)}{\partial z} \right]_{(r=r^{(j)}(t) + (h/2)v_r^{(j)}(t) + (ar_1/2)(h/2)^2, \\
&\quad z=z^{(j)}(t) + (h/2)v_z^{(j)}(t) + (az_1/2)(h/2)^2)}, \\
ar_3 &= (-e/m) \left[ \frac{\partial\phi(r,z)}{\partial r} \right]_{(r=r^{(i)}(t) + (h/2)v_r^{(j)}(t) + (ar_2/2)(h/2)^2, \\
&\quad z=z^{(j)}(t) + (h/2)v_z^{(j)}(t) + (az_2/2)(h/2)^2)}, \\
az_3 &= (-e/m) \left[ \frac{\partial\phi(r,z)}{\partial z} \right]_{(r=r^{(i)}(t) + (h/2)v_r^{(j)}(t) + (ar_2/2)(h/2)^2, \\
&\quad z=z^{(j)}(t) + (h/2)v_z^{(j)}(t) + (az_2/2)(h/2)^2)}, \\
ar_4 &= (-e/m) \left[ \frac{\partial\phi(r,z)}{\partial r} \right]_{(r=r^{(j)}(t) + hv_r^{(j)}(t) + (ar_3/2)h^2, \\
&\quad z=z^{(j)}(t) + hv_z^{(j)}(t) + (az_3/2)h^2)}, \\
az_4 &= (-e/m) \left[ \frac{\partial\phi(r,z)}{\partial z} \right]_{(r=r^{(j)}(t) + hv_r^{(j)}(t) + (ar_3/2)h^2, \\
&\quad z=z^{(j)}(t) + hv_z^{(j)}(t) + (az_3/2)h^2)}, \\
v_r^{(j)(t+h)} &= v_r^{(j)(t)} + (h/6)(ar_1 + 2ar_2 + 2ar_3 + ar_4), \\
v_z^{(j)(t+h)} &= v_z^{(j)(t)} + (h/6)(az_1 + 2az_2 + 2az_3 + az_4).
\end{aligned} \tag{A.5}$$

Typically, we expect that any perturbations to the electric field will approach zero far from the specimen (e.g.  $10^{-4}$  m), so we often need only solve for the electric field relatively close to the cathode variations. We may also, then, begin the Runge–Kutta method at some point  $z = z_1$  much closer to the cathode, minimising computation time. This also ensures that the final point of the trajectory is at  $z = 0$  as required, whereas a full Runge–Kutta treatment to  $z = 0$  would often overshoot the position  $z = 0$  due to the discrete size of the time step  $h$ .

The derivative of the electric potential  $\phi$  may be performed, for example, via the symmetric finite-difference approximation [40]

$$\partial\phi(r, z)/\partial r \approx (\phi(r + \Delta, z) - \phi(r - \Delta, z))/2\Delta. \tag{A.6}$$

Note that a smaller derivative step size  $\Delta$  will not always increase accuracy, as a  $\Delta$  that is too small may result in the difference  $(\phi(r+\Delta, z) - \phi(r-\Delta, z))$  being in the significant figures affected by numerical noise and/or rounding errors. For the examples in this paper,  $\Delta = 5 \times 10^{-9}$  m for  $z$  derivatives and  $\Delta = 10^{-7}$  m for  $r$  derivatives.

The choice of time step  $h$  follows similar constraints. If it is too large (e.g.  $10^{-12}$  s), the electron may pass beyond the classical turning point  $z = L_M$  and the boundary of the droplet, which disrupts the ray tracing method. If it is too small (e.g.  $10^{-15}$  s), computation time is greatly increased and the differences in position may occur only in the significant figures that are most strongly affected by numerical noise and/or rounding errors.

The choice of the parameters used in the FreeFEM++ solution of Laplace's equation (see section 6) will influence the accuracy of the simulations, as numerical errors in the electric potential solution will directly affect the simulated trajectories. In particular, the number of maximum mesh points allowed in the mesh adaption function must be sufficient to properly sample the variations of the electric field. For the droplet and trail considered here, the default FreeFEM++ maximum of 9000 mesh vertices was sufficient, but for a rapidly varying electric potential (e.g. sharp surface steps that are tens of nanometres apart) a higher maximum is required. Similarly, the mesh adaption error must be sufficiently small, so that the generated mesh samples the electric potential over an appropriately small scale where the potential varies over a short distance.

If these parameters are not well chosen, it is usually evident as large coarse areas of mesh, in asymmetry in the mesh pattern above a symmetrical specimen, and in the instability and roughness of the recovered equipotential surfaces. We therefore recommend examining plots of the mesh and equipotential surfaces above the specimen to ensure they are well behaved.

- [1] A. E. Luk'yanov, G. V. Spivak, R. S. Gvozdover, *Sov. Phys. Usp.* 16 (1974) 529 (doi:10.1070/PU1974v016n04ABEH005299).
- [2] A. B. Bok, in *Diffraction and Imaging Techniques in Material Science* (Eds. S. Amelinckx, R. Gevers & J. Van Landuyt), 2nd rev. edn., Amsterdam: North-Holland, 1978, pp. 761–788.

- [3] J. C. Dupuy, A. Sibai, B. Vilotitch, *Surf. Sci.* 147 (1984) 191 (doi:10.1016/0039-6028(84)90175-4).
- [4] J. Slezák, M. Ondřejček, Z. Chvoj, V. Cháb, H. Conrad, S. Heun, Th. Schmidt, B. Ressel, K. C. Prince, *Phys. Rev. B* 61 (2000) 16121 (doi:10.1103/PhysRevB.61.16121).
- [5] T. Shimakura, Y. Takahashi, M. Sugaya, T. Ohnishi, M. Hasegawa, H. Ohta, *Microelectron. Eng.* 85 (2008) 1811 (doi:10.1016/j.mee.2008.05.018).
- [6] S. A. Nepijko, G. Schönhense, *J. Microsc.* 238 (2010) 90 (doi:10.1111/j.1365-2818.2009.03340.x).
- [7] E. Hilner, A. A. Zakharov, K. Schulte, P. Kratzer, J. N. Andersen, E. Lundgren, A. Mikkelsen, *Nano Lett.* 9 (2009) 2710 (doi:10.1021/nl9011886).
- [8] J. Tersoff, D. E. Jesson, W. X. Tang, *Science* 324 (2009) 236 (doi:10.1126/science.1169546).
- [9] J. Tersoff, D. E. Jesson, W. X. Tang, *Phys. Rev. Lett.* 105 (2010) 035702 (doi:10.1103/PhysRevLett.105.035702).
- [10] M. E. Barnett, W. C. Nixon, *J. Sci. Instrum.* 44 (1967) 893 (doi:10.1088/0950-7671/44/11/302).
- [11] W. Świąch, B. Rausenberger, W. Engel, A. M. Bradshaw, E. Zeitler, *Surf. Sci.* 294 (1993) 297 (doi:10.1016/0039-6028(93)90116-2).
- [12] E. Bauer, *Surf. Rev. Lett.* 5 (1998) 1275 (doi:10.1142/S0218625X98001614).
- [13] H.-C. Kan, R. J. Phaneuf, *J. Vac. Sci. Technol. B* 19 (2001) 1158 (doi:10.1116/1.1385688).
- [14] S. A. Nepijko, N. N. Sedov, G. Schönhense, *J. Microsc.* 203 (2001) 269 (doi:10.1046/j.1365-2818.2001.00895.x).
- [15] C. C. Speake, C. Trenkel, *Phys. Rev. Lett.* 90 (2003) 160403 (doi:10.1103/PhysRevLett.90.160403).
- [16] M. E. Barnett, W. C. Nixon, *Optik* 26 (1967) 310.

- [17] A. J. Hermans, J. A. Petterson, *J. Eng. Math.* 4 (1970) 141 (doi:10.1007/BF01535086).
- [18] S. M. Kennedy, D. E. Jesson, M. J. Morgan, A. E. Smith, P. F. Barker, *Phys. Rev. A* 74 (2006) 044701 (doi:10.1103/PhysRevA.74.044701).
- [19] R. Godehardt, *Adv. Imag. Elect. Phys.* 94 (1995) 81 (doi:10.1016/S1076-5670(08)70144-7).
- [20] S. A. Nepijko, N. N. Sedov, *Adv. Imag. Elect. Phys.* 102 (1997) 273 (doi:10.1016/S1076-5670(08)70125-3).
- [21] S. A. Nepijko, A. Gloskovskii, N. N. Sedov, G. Schönhense, *J. Microsc.* 211 (2003) 89 (doi:10.1046/j.1365-2818.2003.01199.x).
- [22] G. F. Rempfer, O. H. Griffith, *Ultramicroscopy* 47 (1992) 35 (doi:10.1016/0304-3991(92)90184-L).
- [23] N. N. Sedov, *J. Microsc.-Paris* 9 (1970) 1.
- [24] T. Someya, J. Kobayashi, *Phys. Status Solidi (a)* 26 (1974) 325 (doi:10.1002/pssa.2210260134).
- [25] S. M. Kennedy, C. X. Zheng, W. X. Tang, D. M. Paganin, D. E. Jesson, *Proc. R. Soc. A* 466 (2010) 2857 (doi:10.1098/rspa.2010.0093). And *ibid.* Addendum, submitted in 2010.
- [26] M. V. Berry, in *Physics of Defects, Les Houches Lecture Series Session XXXV* (Eds. R. Balian, M. Kléman, J.-P. Poirier), Amsterdam: North-Holland, 1981, pp. 453–543.
- [27] J. F. Nye, *Natural Focusing and Fine Structure of Light: Caustics and Wave Dislocations*, Bristol: Institute of Physics Publishing, 1999, pp. 9–11, 46–48.
- [28] E. Bauer, *Ultramicroscopy* 17 (1985) 51–56 (doi:10.1016/0304-3991(85)90176-7).
- [29] E. Bauer, *Rep. Prog. Phys.* 57 (1994) 895 (doi:10.1088/0034-4885/57/9/002).
- [30] I. S. Grant, W. R. Phillips, *Electromagnetism*, 2nd edn., Chichester: John Wiley & Sons, 1990, pp. 100–103.

- [31] J. D. Jackson, *Classical Electrodynamics*, 3rd edn., New York: John Wiley & Sons, 1999, pp. 34–35, 111–112.
- [32] M. T. Boudjelkha, J. B. Diaz, *Appl. Anal.* 1 (1972) 297 (doi:10.1080/00036817208839020).
- [33] D. E. Jesson, K. M. Pavlov, M. J. Morgan, B. F. Usher, *Phys. Rev. Lett.* 99 (2007) 016103 (doi:10.1103/PhysRevLett.99.016103).
- [34] G. N. Polozhiy, *Equations of Mathematical Physics*, New York: Hayden Book Company, 1967, pp. 62–64, 149.
- [35] W. X. Tang, D. E. Jesson, K. M. Pavlov, M. J. Morgan, B. F. Usher, *J. Phys.: Condens. Matter* 21 (2009) 314022 (doi:10.1088/0953-8984/21/31/314022).
- [36] H. R. Lewis Jr., *J. Appl. Phys.* 37 (1966) 2541 (doi:10.1063/1.1782081).
- [37] G. Schönecker, R. Spehr, H. Rose, *Nucl. Instr. and Meth. A* 298 (1990) 360 (doi:10.1016/0168-9002(90)90638-M).
- [38] W. Wan, J. Feng, H.A. Padmore, D.S. Robin, *Nucl. Instr. and Meth. A* 519 (2004) 222 (doi:10.1016/j.nima.2003.11.159).
- [39] F. Hecht, O. Pironneau, A. Le Hyaric, J. Morice, FreeFem++ version 3.9-0, accessed June 2010, available from <http://www.freefem.org/ff++/>
- [40] W. H. Press, S. A. Teukolsky, W. T. Vetterling, B. P. Flannery, *Numerical Recipes, the Art of Scientific Computing*, 3rd edn., Cambridge: Cambridge University Press, 2007, pp. 229–232, 907–910, and chapter 10.
- [41] M. Born, E. Wolf, *Principles of Optics*, 7th (expanded) edn., Cambridge: Cambridge University Press, 2006, pp. 120–125.
- [42] M. V. Berry, in *Singular Optics*, SPIE proceedings (Ed. M. S. Soskin), vol. 3487, Bellingham, WA: SPIE International Society for Optical Engineering, 1998, pp. 1–5.
- [43] V. I. Arnol'd, in *Bifurcations and Catastrophe Theory* (Eds. V. I. Arnol'd, V. S. Afrajmovich, Yu. S. Il'yashenko, L. P. Shil'nikov, N. Kazarinoff), Berlin: Springer-Verlag, 1999, Ch. 2.

- [44] J. Massies, P. Etienne, F. Dezaly, N. T. Linh, *Surf. Sci.* 99 (1980) 121 (doi:10.1016/0039-6028(80)90582-8).
- [45] Th. Schmidt, H. Marchetto, P. L. Lévesque, U. Groh, F. Maier, D. Preikszas, P. Hartel, R. Spehr, G. Lilienkamp, W. Engel, R. Fink, E. Bauer, H. Rose, E. Umbach, H.-J. Freund, *Ultramicroscopy* 110 (2010) 1358 (doi:10.1016/j.ultramic.2010.07.007).
- [46] J. C. H. Spence, *High-Resolution Electron Microscopy*, 3rd edn., Oxford University Press, 2003, pp. 40–41.
- [47] S. M. Kennedy, N. E. Schofield, D. M. Paganin, D. E. Jesson, *Surf. Rev. Lett* 16 (2009) 855 (doi:10.1142/S0218625X09013402).

---

## Wave optical treatment of surface step contrast in LEEM

This chapter is an author generated post print of the article

S. M. Kennedy, N. E. Schofield, D. M. Paganin and D. E. Jesson, 'Wave optical treatment of surface step contrast in low-energy electron microscopy,' *Surf. Rev. Lett.*, **16** (2009) 855–867, available electronically at <http://www.worldscinet.com/srl/> or via doi:10.1142/S0218625X09013402.

A minor correction was made to Eq. (4) of chapter 4, which was missing a negative sign. This was a typographical error carried over from Shao and Crewe (1989) (see Rempfer and Griffith, 1992), but in all calculations the correct sign was used. In a related sentence following Eq. (4) the word 'negative' was replaced by 'positive.'

In the last paragraph of page 75 of chapter 4, the word 'optimum' was removed when used in reference to the Scherzer defocus in the published version. This is because the Scherzer defocus is, in general, only an optimum defocus for weak phase objects, and some of the examples used in chapter 4 are not weak phase objects. In the last paragraph of page 75 and the last paragraph of page 82 of chapter 4 we now explicitly mention that the Scherzer defocus is optimum for weak phase objects.



### Declaration for thesis chapter 'Wave optical treatment of surface step contrast in low-energy electron microscopy.'

#### Declaration by candidate

For this chapter, the nature and extent of my contribution to the work was the following:

Nature of contribution	Extent of contribution (%)
Significantly extended the initial model, performed the simulations and produced the images of the paper, co-wrote the paper.	75

The following co-authors contributed to the work. Co-authors who are students at Monash University must also indicate the extent of their contribution in percentage terms:

Name	Nature of contribution	Extent of contribution (%) for student co-authors only
Naomi Schofield	Preliminary development of the model in previous Honours work. Co-wrote and provided technical expertise.	15
David Paganin	Co-wrote, helped develop the model and provided technical expertise.	
David Jesson	Co-wrote, helped develop the model and provided technical expertise.	

Candidate's Signature  Date 25/8/10

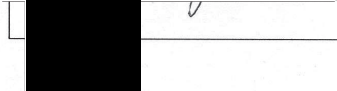
#### Declaration by co-authors

The undersigned hereby certify that:

- (1) the above declaration correctly reflects the nature and extent of the candidate's contribution to this work, and the nature of the contribution of each of the co-authors.
- (2) they meet the criteria for authorship in that they have participated in the conception, execution, or interpretation, of at least that part of the publication in their field of expertise;
- (3) they take public responsibility for their part of the publication, except for the responsible author who accepts overall responsibility for the publication;
- (4) there are no other authors of the publication according to these criteria;
- (5) potential conflicts of interest have been disclosed to (a) granting bodies, (b) the editor or publisher of journals or other publications, and (c) the head of the responsible academic unit; and
- (6) the original data are stored at the following location(s) and will be held for at least five years from the date indicated below:

Location(s)

Signature 1  Date 25/8/10

Signature 2  Date 26/8/2010

Signature 3  Date 26-8-10



## WAVE OPTICAL TREATMENT OF SURFACE STEP CONTRAST IN LOW ENERGY ELECTRON MICROSCOPY

S. M. KENNEDY, N. E. SCHOFIELD, D. M. PAGANIN and D. E. JESSON\*

*School of Physics, Monash University  
Victoria 3800, Australia  
e-mail: david.jesson@monash.edu*

A wave-optical treatment of surface step contrast in a low energy electron microscope (LEEM) is presented. The aberrations of an idealised LEEM imaging system are directly incorporated into a transfer function (TF) and image simulations of surface steps are evaluated in one- and two-dimensions. Under the special circumstances of a weak phase object, the simplified form of the contrast transfer function (CTF) is used to discuss LEEM image contrast and optimum defocus conditions.

*Keywords:* Low energy electron microscopy (LEEM); surface steps; phase contrast imaging; contrast transfer function.

### 1. Introduction

Low energy electron microscopy (LEEM) is a well-established technique for the imaging of surfaces.<sup>1,2,3,4,5,6</sup> The capability to image the behaviour of surface steps in real-time has provided important insight into a wealth of surface physics phenomena including mass-transport, evaporation and nucleation processes.<sup>1,2</sup> The two main methods for imaging surface steps in LEEM are diffraction and phase contrast imaging. Diffraction contrast can be usefully exploited when different surface reconstructions exist on the up and down-side of steps. A classic example of this geometry is Si(001) where monolayer surface steps are present at the boundaries between  $(2 \times 1)$  and  $(1 \times 2)$  reconstructions. An aperture is placed around appropriate diffraction spots in the low energy electron diffraction (LEED) pattern to select scattering from only one of the reconstructed surfaces.<sup>6</sup> Thus steps are revealed at the boundaries between bright and dark reconstructed domains in the image. Phase contrast methods are more general and exploit the variation in phase of the incident electron wave as it is reflected in the vicinity of the step edge. Although significant progress has been made in understanding the origin of step contrast in terms of the Fresnel integrals of paraxial wave optics,<sup>3,4</sup> image simulations which formally incorporate the instrument aberrations into a transfer function (TF) have yet to be implemented. The development of such methods is of particular importance given the likely emergence

---

\*Corresponding author.

of aberration corrected LEEM systems<sup>7</sup> where contrast interpretation at high resolution may become a significant issue.

Here we develop a method to rapidly simulate LEEM image contrast from surface steps. We treat the interaction of the low energy electrons with the surface step as a wave optical phenomenon and define the appropriate surface phase object function  $O(\mathbf{R})$ . We then combine the aberrations of the LEEM imaging system to obtain the TF of the effective objective lens which forms a virtual image of  $O(\mathbf{R})$ . This method has the advantage that conventional contrast transfer function theory can be applied and used to interpret the image contrast and assess resolution in terms of instrumental parameters.<sup>8</sup> LEEM image simulations of two-dimensional objects can be readily performed. We briefly consider the restricted case of imaging a weak phase object (WPO) in which the simplified form of the contrast transfer function (CTF) can be used to discuss optimum defocus conditions and the important role of chromatic aberration.

## 2. Phase Object Function for Surface Step Contrast

A schematic showing electron interaction with a surface step of height  $a$  is contained in Fig. 1(a).

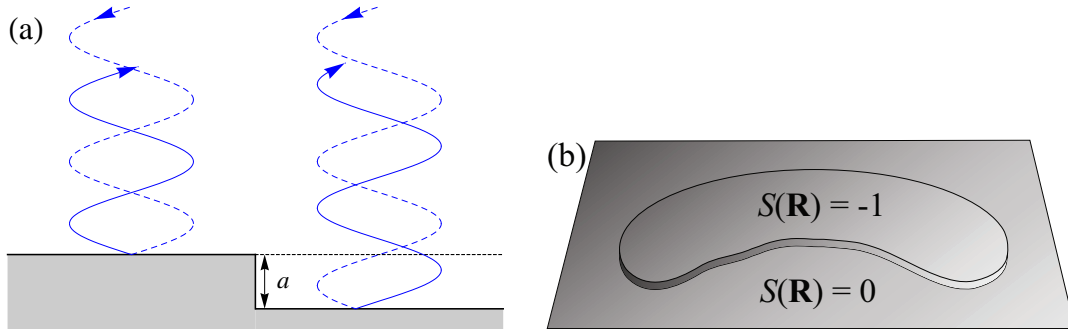


Figure 1: (a) Origin of the electron phase change at a surface step. Electrons reflected from the lower terrace travel an extra distance  $2a$  compared with electrons reflected from the upper terrace. (b) Schematic of a monolayer-height island which is described by the shape function  $S(\mathbf{R})$ .

Electrons reflected either side of the step will experience a relative phase difference given by

$$\phi(\mathbf{R}) = \frac{4\pi a}{\lambda_i} S(\mathbf{R}), \quad (1)$$

where  $\lambda_i$  is the incident electron wavelength close to the surface,  $S(\mathbf{R})$  is the step shape function such that  $S(\mathbf{R}) = 0$  if  $z = 0$  (the reference plane), and  $\mathbf{R}$  is a two-dimensional position vector in the plane perpendicular to the optic axis (see Fig. 1(b)). For  $n$  steps up each of height  $z = a$  we have  $S(\mathbf{R}) = -n$ , since a step up has reduced phase compared with the surface  $S(\mathbf{R}) = 0$ , and for  $n$  steps down each of height  $z = -a$  we have  $S(\mathbf{R}) = n$ . The phase object function defining the surface is then given by

$$O(\mathbf{R}) = \exp(i\phi(\mathbf{R})). \quad (2)$$

The phase object function can be readily generalized to arbitrary combinations of steps in an obvious way. It is important to appreciate that this approach inherently assumes

that the surface steps do not significantly modify the uniform electric field of the cathode immersion lens. For larger surface perturbations it is essential to incorporate local changes in the electric field which can significantly distort the image.<sup>9,10</sup>

### 3. LEEM Cathode Immersion Lens

In LEEM, a nearly parallel beam of low energy electrons is normally incident upon the surface which acts as the cathode of an immersion lens (Fig. 2(a)). The potential of the specimen cathode is offset from the potential of the electron gun by a small adjustable bias voltage  $V$ . The incident electrons are decelerated by the electric field between the specimen and anode at potential  $U_0$  before being reflected at energy  $eV$  and reaccelerated towards the anode. The electric field between the anode and specimen cathode is essentially uniform except for close to the anode aperture which acts as a diverging lens.

It is convenient to partition image formation by the immersion lens into two parts; an accelerating and imaging part, which can then be treated separately.<sup>11</sup> In Fig. 2(b) we show the influence of the homogeneous electric field on the trajectory of an electron reflected from the surface with energy  $eV$  from the point  $O$ . The electrons experience a parabolic path in the uniform field and appear to originate from a point  $A$  located in a virtual image plane at a distance  $2L$  from the anode. The spherical and chromatic aberration coefficients of this uniform field have been evaluated by Shao *et al.*<sup>12</sup> to be

$$C_S^U = 2\rho_0 L \left( \frac{1}{2}\omega_0^{3/2} - \omega_0 + \frac{1}{2}\sqrt{\omega_0} \right), \quad (3)$$

and

$$C_C^U = -2L \left( 1 - \frac{1}{\sqrt{\omega_0}} - \frac{1}{2\rho_0\sqrt{\omega_0}} \right), \quad (4)$$

where  $\rho_0 = V/U_0$  and  $\omega_0 = (1 + 1/\rho_0)$ . We note that  $C_C^U$  is positive and has the same sign as a conventional electron lens.

Finally, we take into account the effect of the aperture by assuming that the uniform field is terminated by an ideal diverging lens as shown in Fig. 2(c).<sup>5</sup> The virtual specimen, created by the uniform field at  $2L$  from the anode, is the object of the aperture lens with focal length  $f = -4L$ . As shown in Fig. 2(c), this lens forms a virtual image of the virtual specimen at point  $B$  which is located in a virtual image plane a distance  $4L/3$  from the anode. This image is demagnified by a factor of  $2/3$ .

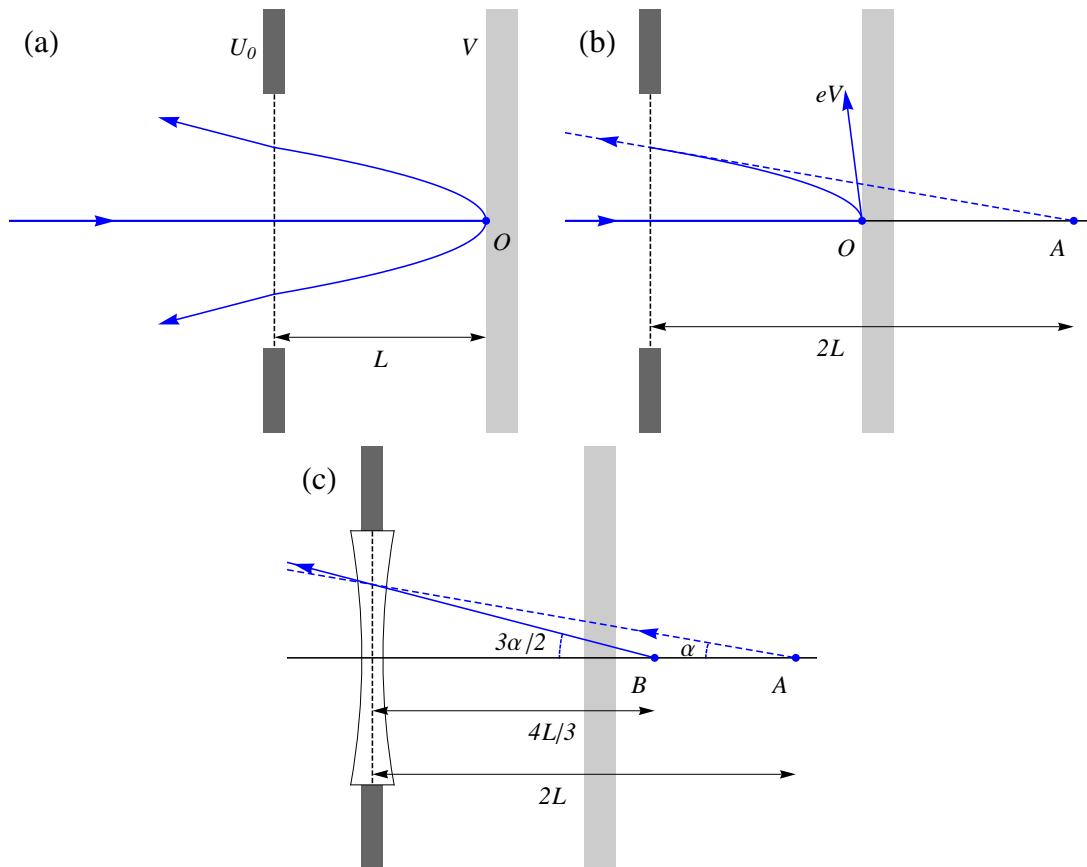


Figure 2: Schematic of the cathode immersion lens. (a) A parallel beam of incident electrons is reflected at point  $O$  and accelerated towards the anode at potential  $U_0$ . The potential of the specimen differs from the anode by  $V$  and the anode aperture acts as a diverging lens. (b) Influence of the homogeneous electric field on the trajectory of an electron reflected from the surface with energy  $eV$  from the point  $O$ . The electrons travel a parabolic path in the uniform field and appear to originate from a point  $A$  located in a virtual image plane at a distance  $2L$  from the anode. (c) The effect of the aperture is incorporated by assuming that the uniform field is terminated by an ideal diverging lens. The virtual object created by the uniform field at  $2L$  is the object of the aperture lens of focal length  $f = -4L$ . This lens forms a virtual image of the virtual specimen at point  $B$  which is located in a virtual image plane a distance  $4L/3$  from the anode. This is the object plane of the LEEM objective lens. Adapted from Rempfer and Griffith<sup>5</sup>

#### 4. Objective Lens

The virtual image at  $4L/3$  is the object plane of the LEEM objective lens. Given the geometry of the cathode immersion lens and the necessity to focus on this plane, the focal length of the objective must be large. This means that its spherical ( $C_S^O$ ) and chromatic ( $C_C^O$ ) aberration coefficients are also large and must be included in the imaging model. To combine the aberration coefficients of the objective lens with those of the homogenous field we note that they must be referred to objects of the same lateral magnification. However, following the action of the aperture lens the lateral magnification of the object for the objective lens is  $2/3$ . As discussed by Rempfer *et al.*,<sup>5</sup> a ray angle  $\alpha$  following divergence by the aperture lens is increased to  $1.5\alpha$  (see Fig. 2(c)) and so the combined aberration coefficients of the homogeneous accelerating field and objective lens are<sup>5</sup>

$$C_S = C_S^U + (1.5)^4 C_S^O, \quad (5)$$

and

$$C_C = C_C^U + (1.5)^2 C_C^O. \quad (6)$$

Thus, we can consider imaging a virtual object of magnification  $M = 1$  located in a virtual image plane at a distance  $2L$  from the anode with an effective lens of aberration coefficients  $C_S$  and  $C_C$ .

#### 5. Transfer Function

With the aberrations of the uniform accelerating field and objective lens combined, we are now in the position to define the transfer function of the instrument and apply wave optical methods to evaluate the image of a phase object function for a given surface step arrangement. Under the assumption that one is working with a shift-invariant linear imaging system,<sup>13</sup> the LEEM instrument transforms each point in the phase object function into an extended region, such that the wavefunction in the image plane is given by<sup>14</sup>

$$\psi(\mathbf{R}) = O(\mathbf{R}) \otimes T(\mathbf{R}), \quad (7)$$

where  $T(\mathbf{R})$  is the complex point spread function (Green function, real-space propagator) and  $\otimes$  denotes two-dimensional convolution. Note that harmonic time dependence, for all stationary-state complex scalar wavefunctions considered here, will be suppressed.

To evaluate the LEEM image intensity it is convenient to work with the Fourier transform of  $\psi(\mathbf{R})$  with respect to  $\mathbf{R}$  and evaluate the electron wavefunction in the back-focal plane of the effective objective lens. We then have

$$\psi(\mathbf{u}) = O(\mathbf{u})T(\mathbf{u}), \quad (8)$$

where  $O(\mathbf{u})$  is the Fourier transform of  $O(\mathbf{R})$ .  $T(\mathbf{u})$  is the transfer function of the system given by

$$T(\mathbf{u}) = A(\mathbf{u})B(\mathbf{u}), \quad (9)$$

where  $\mathbf{u}$  is a reciprocal (diffraction) space coordinate and we use the convention  $u = 1/R$ . The aperture function

$$A(\mathbf{u}) = \begin{cases} 1, & |\mathbf{u}| \leq u_A, \\ 0, & \text{otherwise,} \end{cases} \quad (10)$$

takes into account the effect of a contrast aperture by removing all spatial frequencies with a magnitude greater than  $u_A$ . Due to practical considerations the contrast aperture is usually located in a conjugate plane to the back-focal plane of the objective lens in the imaging part of the LEEM column, with equivalent effect.

The aberration function  $B(\mathbf{u})$  is written as

$$B(\mathbf{u}) = \exp(i\chi(\mathbf{u})), \quad (11)$$

where<sup>14,15,16</sup>

$$\chi(\mathbf{u}) = \pi\Delta f\lambda u^2 + \pi C_S\lambda^3 u^4/2. \quad (12)$$

Here  $\lambda$  is the incident electron wavelength, with energy  $eU_0$  ( $e$  is the electron charge). In the first term of Eq. (12),  $\Delta f$  represents the amount of defocus away from the object plane of the objective lens, which is located a distance  $2L$  from the anode (see Fig. 2(c)). The second term takes into account the phase shift introduced by spherical aberration and includes the combined aberration coefficient given by Eq. (5). Higher order aberrations, e.g. higher order spherical aberration terms, can also be naturally incorporated into the transfer function formalism. The inclusion of such terms will be of increasing importance given the likely emergence of aberration corrected LEEM systems.<sup>7</sup>

Substituting Eqs. (9)–(12) into (8) then provides an expression for  $\psi(\mathbf{u})$ ,

$$\psi(\mathbf{u}) = O(\mathbf{u})A(\mathbf{u}) \exp(i\pi\Delta f\lambda u^2 + i\pi C_S\lambda^3 u^4/2). \quad (13)$$

The above discussion is for a monochromatic electron beam. We must also take into account the finite energy spread of the electron source. A spread in emission energies results in a distribution in defocus  $\varepsilon$  about the mean value  $\Delta f$ , because electrons with different energy are focused to a different point. We may therefore replace  $\Delta f$  in Eq. (13) with  $\Delta f + \varepsilon$  to represent the Fourier transform of the electron wavefunction  $\psi_\varepsilon(\mathbf{R})$ , which is located at a distance  $\varepsilon$  from the imaging plane at  $2L + \Delta f$  from the anode. The image at a particular value of defocus  $\varepsilon$  is given by

$$I_\varepsilon(\mathbf{R}) = |\psi_\varepsilon(\mathbf{R})|^2. \quad (14)$$

To evaluate the final intensity we must average the intensities over defocus

$$I_C(\mathbf{R}) = \int_{-\infty}^{\infty} I_\varepsilon(\mathbf{R})D(\varepsilon) d\varepsilon. \quad (15)$$

Following the approach of Fejes,<sup>17</sup> we approximate the defocus distribution as a Gaussian distribution with standard deviation  $\sigma$ ,

$$D(\varepsilon) = \frac{1}{\sigma\sqrt{2\pi}} \exp\left(-\frac{\varepsilon^2}{2\sigma^2}\right), \quad (16)$$

although other distributions can be readily incorporated. The standard deviation of the defocus Gaussian distribution  $\sigma$  is related to the energy distribution via<sup>15,18</sup>

$$\sigma = C_C \frac{\sigma_E}{E} = C_C \frac{\Delta E}{E\sqrt{8\log(2)}}. \quad (17)$$

Here  $C_C$  is the combined chromatic aberration coefficient (Eq. (6)),  $\sigma_E$  is the standard deviation of the energy Gaussian distribution,  $E = eU_0$  is the incident electron energy,

and  $\Delta E$  is the full width half maximum of the energy distribution. It is also possible to include defocus variations due to fluctuations in lens currents and/or the accelerating voltage. Here we assume that energy spread dominates chromatic aberration. In addition to temporal coherence, the electron source is a finite size and this will influence spatial coherence. However, for modern field emission guns this latter effect can be neglected compared with the influence of energy spread.<sup>3,4</sup>

## 6. Simulation of LEEM contrast from steps

Based on the above formalism, we are now in a position to perform LEEM image simulations of surface step contrast in both one and two dimensions. We begin with a one dimensional step as depicted schematically in Fig. 1(a). We choose a step height  $a = 0.31$  nm corresponding to steps on the Si(111) surface<sup>19</sup> which for a bias voltage  $V = 5$  V gives a phase difference across the step of  $(0.82 + 2\pi)$  as defined by Eq. (1). For all simulations we assume typical values of  $L = 2$  mm and  $U_0 = 20$  kV. The contrast aperture of radius  $u_A = 0.6$  nm<sup>-1</sup> removes all spatial frequencies greater than this value from the LEEM image (see Eq. (10)). However, for the modelling considered here we shall see that the inclusion of chromatic aberration typically dampens the high frequency contributions to a negligible value, so provided the aperture is greater than  $\sim 0.4$  nm<sup>-1</sup>, the precise position of the aperture has no effect on the image contrast.

To numerically evaluate the LEEM image of the step we first evaluated  $O(\mathbf{u})$  by obtaining the Fourier transform of  $O(\mathbf{R})$ . The discrete step was approximated analytically by the sum of two inverse tangent functions which have a finite transition or step width. However, provided this width is sufficiently narrow ( $\leq 0.1$  nm), the precise shape of the step profile was found to have little influence on the images generated. The fast Fourier transform algorithm<sup>20</sup> employed uses a uniformly spaced array of discrete data points, and assumes periodic boundary conditions for the array. To maintain periodicity we therefore considered the transverse periodic continuation of a step-down and step-up system taking care to separate the steps sufficiently ( $\sim 1.6$   $\mu\text{m}$ ) so there is no interference between diffraction from the steps during imaging. Image contrast from an individual step could therefore be studied in isolation.  $O(\mathbf{u})$  was then inserted into Eq. (13) to obtain  $\psi(\mathbf{u})$  and the image intensity  $I_\varepsilon(\mathbf{R})$  was evaluated from the modulus squared of the inverse Fourier transform of  $\psi(\mathbf{u})$  via Eq. (14). Care was taken to correctly sample all functions in real and reciprocal space to avoid numerical error (see Appendix).

A LEEM image simulation of the model step in Fig. 1(a) is contained in Fig. 3(a) for a monochromatic source, using Eq. (14) for  $\varepsilon = 0$ . The corresponding imaginary part of the LEEM transfer function  $T(\mathbf{u})$ —known as the phase contrast transfer function,<sup>8</sup> see Section —is shown in Fig. 4 for  $\Delta f = -3.0$   $\mu\text{m}$ . This defocus is the Scherzer defocus<sup>14</sup>  $\Delta f_{SC} = -1.2(C_S\lambda)^{1/2}$  which for weak phase objects balances the defocus term with the effect of spherical aberration in Eq. (12).<sup>21</sup> Under these conditions, the phase contrast TF retains a relatively constant value of near unity out to the first crossover of the zero axis (the point resolution limit).<sup>14</sup> In Fig. 3(a), the contrast displays a minimum in the vicinity of the step with numerous oscillations either side of the step for this monochromatic source. In order to take into account the finite energy spread of the electron source it is necessary to incoherently average such monochromatic contributions over defocus using Eq. (15). The resulting averaged intensity  $I_C(\mathbf{R})$  is displayed in Fig. 3(b) for an energy spread  $\Delta E = 0.3$  eV. Although the general form of the intensity resembles the monochro-

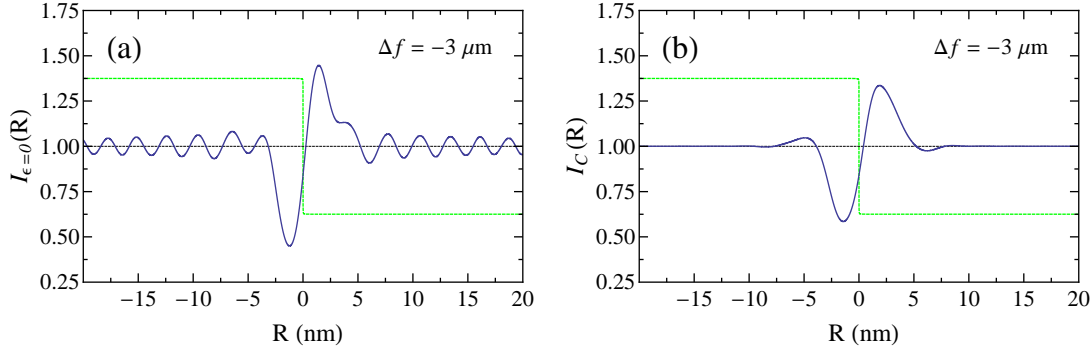


Figure 3: (a) Monochromatic image intensity  $I_{\epsilon=0}(\mathbf{R})$  evaluated for the superimposed step profile (dotted-line) and an associated phase change of  $(0.82 + 2\pi)$ . (b)  $I_C(\mathbf{R})$  for the same phase object in (a) showing chromatic damping of intensity oscillations.

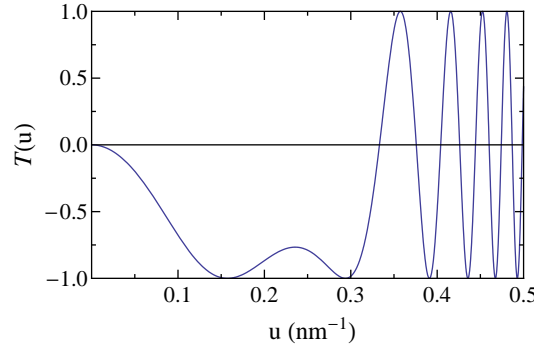


Figure 4: Imaginary part of the LEEM transfer function  $T(\mathbf{u})$ , including defocus and spherical aberration, at the Scherzer defocus of  $\Delta f = -3.0 \mu\text{m}$  (cf. Eq. (20)).

matic intensity contrast in Fig. 3(a), the fine fringes surrounding the step are smoothed out by the incoherent averaging process, Eq. (15). Such a localised step intensity profile is in general qualitative agreement with experimental observations.<sup>1,2,3,4</sup>

In Fig. 5 we explore the dependence of LEEM step contrast on objective lens defocus. As discussed by Chung *et al.*<sup>3,4</sup> it is possible to determine the up or down character of a step from the asymmetry of the LEEM intensity profile in the over or under focus condition provided it is known whether  $2n\pi < \phi(\mathbf{R}) < (2n+1)\pi$  or  $(2n+1)\pi < \phi(\mathbf{R}) < 2(n+1)\pi$  for integer  $n$ . In panels (a)–(c) we consider a step phase change of  $\phi(\mathbf{R}) = \pi/2 + 2\pi$ , which is achieved for the step of height  $a = 0.31 \text{ nm}$  by increasing the bias voltage  $V$  to 6.1 V. A phase object of  $\phi(\mathbf{R}) = \pi/2 + 2n\pi$  is identified as an optimum condition for the detection of intensity peak asymmetry.<sup>3,4</sup> As the defocus changes from negative underfocus values to positive overfocus conditions, the intensity maxima and minima swap position on either side of the step indicated by the inset dotted line. Hence it is possible to determine the sense of the step via the intensity asymmetry.<sup>3,4</sup> Note however that the contrast does not completely reverse either side of  $\Delta f = 0$  (i.e. the intensity patterns for  $\pm\Delta f$  are not mirror images of each other). This observation can be attributed to the presence of spherical aberration in the TF (see Eq. (12)) which does not change sign with

defocus. Spherical aberration also results in non-zero phase contrast at  $\Delta f = 0$ . Indeed, minimum contrast in the presence of aberrations is obtained using the minimum contrast defocus<sup>14</sup>  $\Delta f_m = -0.44(C_S\lambda)^{1/2}$ , which reduces to  $\Delta f_m = 0$  when  $C_S \rightarrow 0$ .

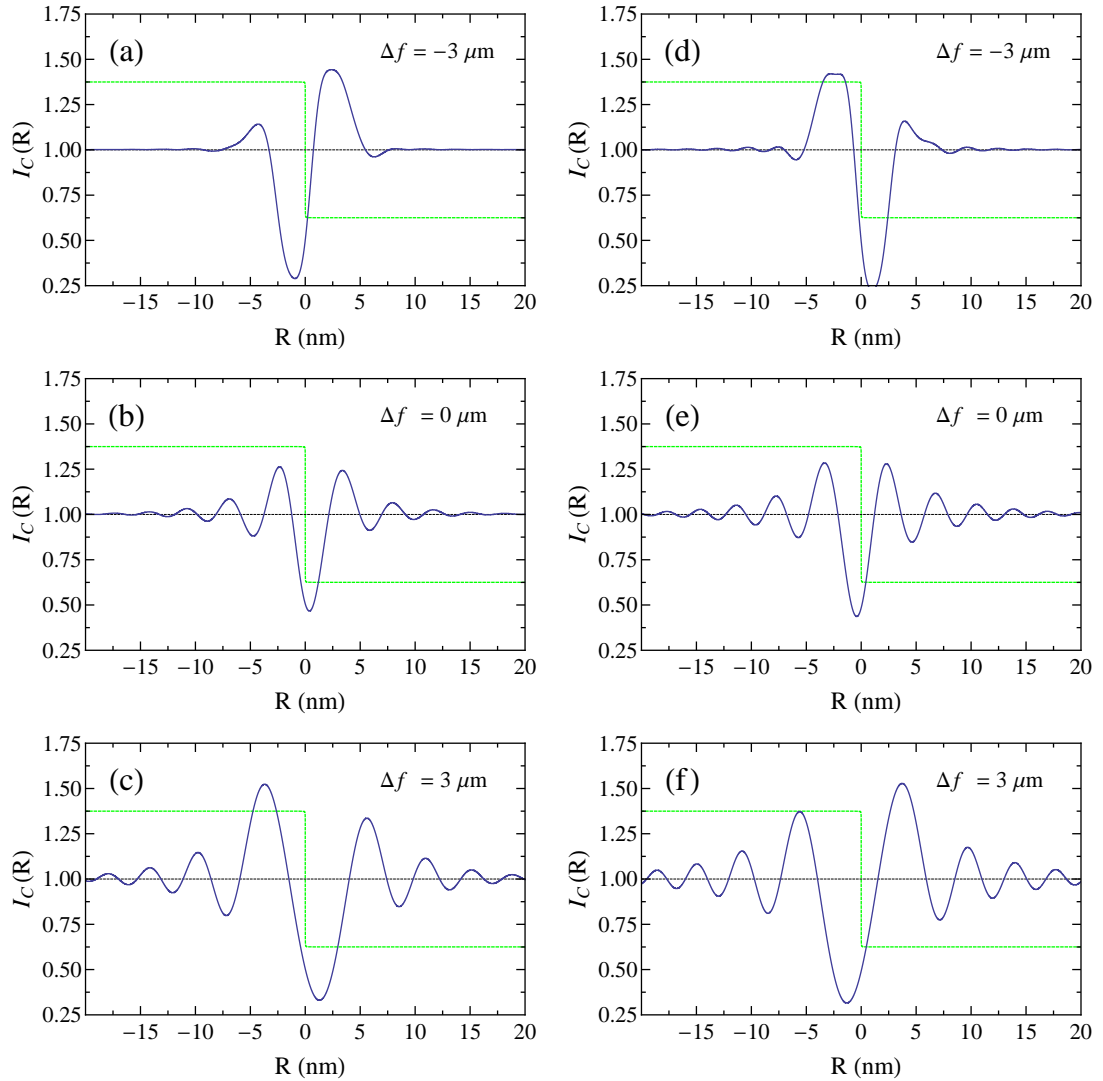


Figure 5:  $I_C(\mathbf{R})$  evaluated for superimposed step profile (dotted-line) of height  $a = 0.31$  nm with  $\Delta E = 0.3$  eV as a function of defocus  $\Delta f$ . The step phase change is  $(\pi/2 + 2\pi)$  in (a)–(c) and  $(3\pi/2 + 2\pi)$  in (d)–(f) which is achieved by adjusting the bias voltage.

The case of  $\phi(\mathbf{R}) = 3\pi/2 + 2\pi$  is considered for the same step in panels 5(d)–(f) by increasing the bias voltage  $V$  to 12 V. Again, this is an optimum condition for the detection of intensity peak asymmetry in the range  $(2n + 1)\pi < \phi(\mathbf{R}) < 2(n + 1)\pi$ .<sup>3,4</sup> The step contrast reverses sense as expected compared with  $\phi(\mathbf{R}) = \pi/2 + 2\pi$  (panels (a)–(c)) and the intensity maxima and minima swap position on either side of the step on going from underfocus to overfocus. Hence, again it is possible to determine the sense of the step via the intensity asymmetry for this phase object.<sup>3,4</sup> It is interesting to note that the

spherical and chromatic aberration coefficients of the uniform field are also dependent on bias voltage via Eqs. (3) and (4). This introduces additional oscillations in the intensity profile contained in panel (d) relative to panel (a). However, despite the complications introduced by aberrations, the method proposed by Chung *et al.*<sup>3,4</sup> for estimating step sense would still appear to be valid for the cases examined here. Finally, we note that the identification of the precise step edge position from the intensity profile requires an accurate knowledge of the step height phase difference (Eq. (1)) and the parameters of the imaging system.

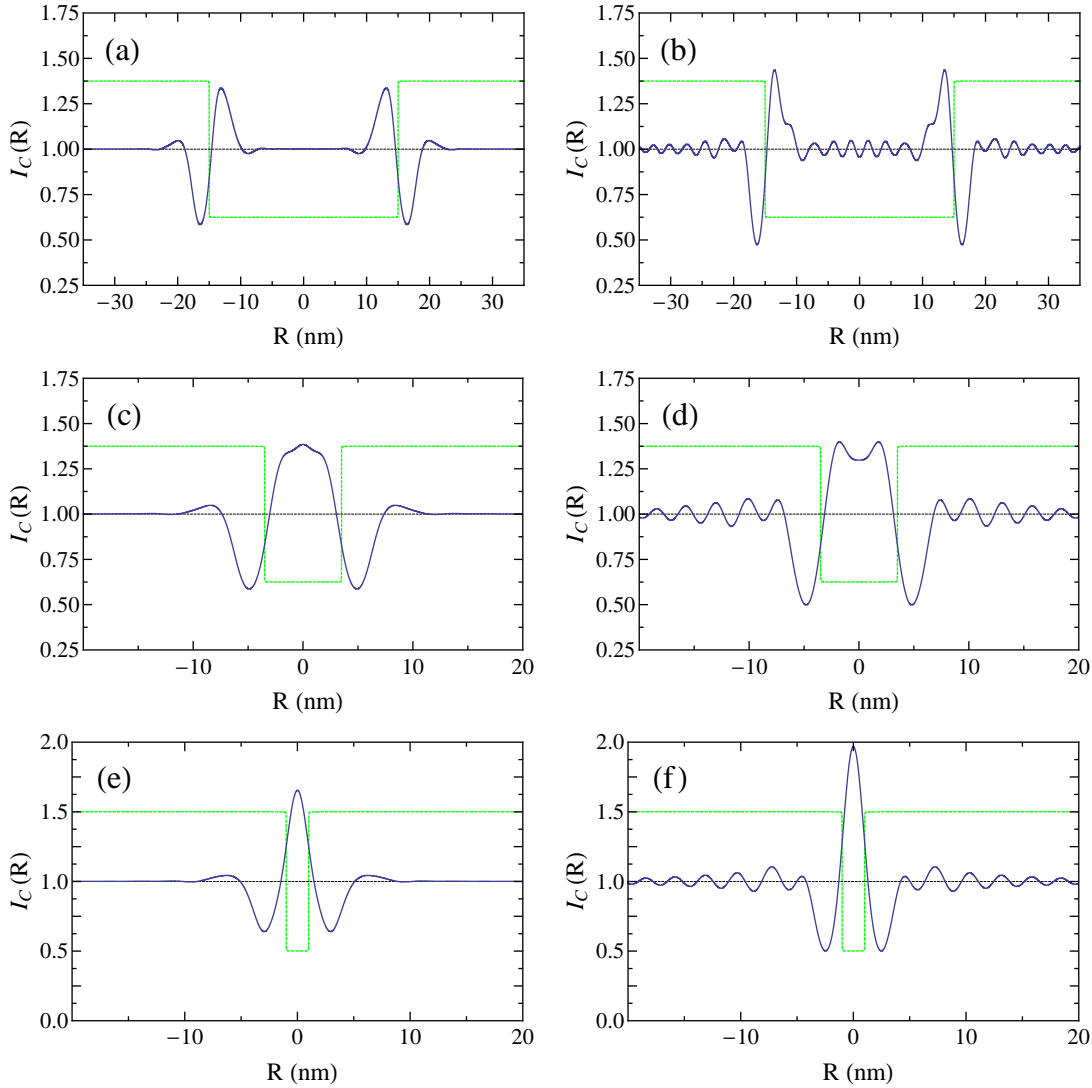


Figure 6:  $I_C(\mathbf{R})$  evaluated for two adjacent steps (dotted-line) which are (a)–(b) 30 nm, (c)–(d) 7 nm and (e)–(f) 2 nm apart.  $\Delta E = 0.3$  eV for (a), (c) and (e) and  $\Delta E = 0.1$  eV for (b), (d) and (f).

An important issue in LEEM is the ability to resolve closely spaced surface steps. This is particularly relevant since the use of aberration correction<sup>7</sup> and/or energy filtering may

make contrast interpretation at high resolution a significant issue. Here we use our simulation method to examine the contrast from a model pair of steps in close proximity as shown in Fig. 6 for energy spreads  $\Delta E = 0.3$  and  $0.1$  eV. For separation of 30 nm (panels (a),(b)) the step contrast is essentially independent with little interference between steps. However at separations of 7 nm (panels (c),(d)) and 2 nm (panels (e),(f)) there is strong constructive interference and a significant peak appears between the two steps. We emphasize that the latter separation is below the instrumental point resolution but the simulation indicates that in principle it is still possible to extract positional information through comparison of simulation with experiment.<sup>22</sup> Note that the reduced energy spread simulations in panels (b), (d) and (f) are associated with more fringes and less contrast localized at the steps. This results in enhanced interference between steps and provides additional features for comparison between experimental images and image simulations.

A wave-optical approach to simulating LEEM contrast from surface steps can be readily extended to two spatial dimensions, for the arrangement of monolayer-step-height circular and elliptical terraces shown in Fig. 7(a). The step phase difference is  $(0.82 + 2\pi)$ , placing it in the  $2n\pi < \phi(\mathbf{R}) < (2n+1)\pi$  interpretation regime. Therefore, in the image simulation shown in Fig. 7(b) the down nature of the outermost terrace produces opposite contrast to the up terraces as expected. As seen previously in Fig. 6, steps that are further apart (30 nm) are easily distinguished, whereas steps that are close together (less than 10 nm) produce more complicated interference patterns. In Fig. 7(b), bright regions of constructive interference are arrowed where the down and up steps are close together (between 10 nm and 5 nm) which complicates direct interpretation. We note that a 2D simulation capability may prove to be valuable in the interpretation of closely spaced step arrangements as well as in the high resolution study of wavy steps induced by instabilities.<sup>23,24,25</sup> To the same end, we note the possible utility of some recent work on phase retrieval using aberrated shift-invariant imaging systems.<sup>26,27</sup>

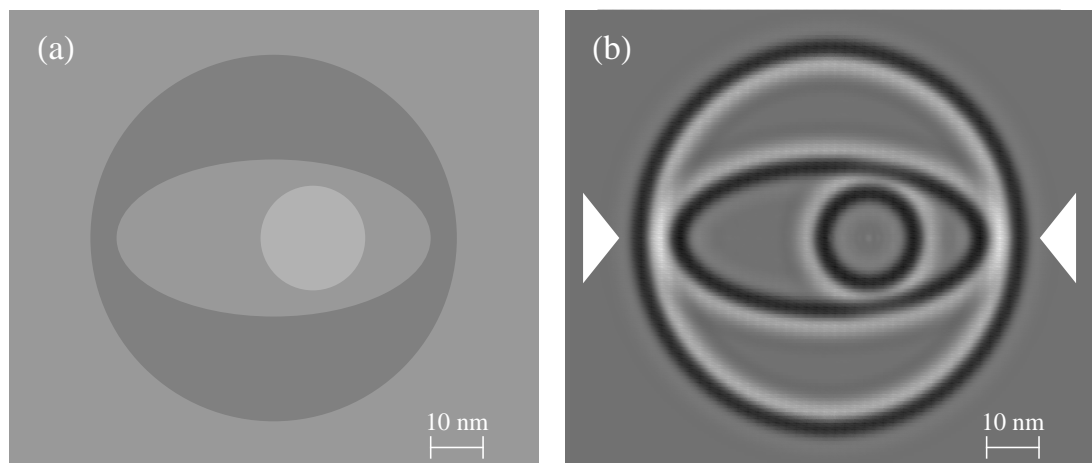


Figure 7: (a) Plan-view schematic of an arrangement of terraces separated by monolayer height steps. Lighter shading indicates increasing height. (b)  $I_C(\mathbf{R})$  evaluated for the phase object function corresponding to the step arrangement in (a). The phase change associated with each step is  $(0.82 + 2\pi)$  and  $\Delta E = 0.3$  eV. Bright regions of constructive interference where the steps are in close proximity are arrowed.

## 7. Weak Phase Object Approximation

In general, the phase changes involved during reflection of low energy electrons from surface steps are not weak (i.e. with maximum transverse phase differences that are small in magnitude relative to  $2\pi$ ). However, it is possible to tune the incident electron wavelength  $\lambda_i$  by adjusting the bias voltage  $V$  such that the phase difference is  $2n\pi + \delta$  for a small quantity  $\delta$  and  $n$  an integer. The step phase change from Eq. (1) is then  $\phi(\mathbf{R}) = \delta$  if  $z = -a$  and  $\phi(\mathbf{R}) = 0$  if  $z = 0$ . Under these conditions we therefore have a weak phase object (WPO) and we can expand the phase object function Eq. (2) to first order

$$O(\mathbf{R}) = 1 + i\phi(\mathbf{R}). \quad (18)$$

The advantage of the WPO approximation is that the form of the transfer function simplifies and it is instructive to examine its form for LEEM. Following the conventional WPO treatment we have the intensity<sup>8,14</sup>

$$I^W(\mathbf{R}) = 1 - 2\phi(\mathbf{R}) \otimes T^W(\mathbf{R}), \quad (19)$$

where  $T^W(\mathbf{R}) = \text{Im}\{T(\mathbf{R})\}$  and the phase contrast transfer function (CTF) in reciprocal space is given by

$$T^W(\mathbf{u}) = A(\mathbf{u}) \sin \chi(\mathbf{u}). \quad (20)$$

Rather than average the intensities over defocus via Eq. (15), it is customary in the WPO to include chromatic aberration effects in the form of a damping function  $E(\mathbf{u})$ .<sup>17</sup> In practice this should be limited to a restricted set of WPOs<sup>17</sup> but here we nevertheless adopt the approach for steps to evaluate the role of chromatic aberration in the LEEM transfer function. The chromatically damped CTF is then given by

$$T_C^W(\mathbf{u}) = A(\mathbf{u})E(\mathbf{u}) \sin \chi(\mathbf{u}). \quad (21)$$

The envelope function<sup>17</sup>

$$E(\mathbf{u}) = \exp(-\pi^2 \lambda^2 \sigma^2 u^4 / 2) \quad (22)$$

takes into account the full width half maximum spread in energy  $\Delta E$  of the electron gun. The WPO intensity, incorporating chromatic effects, is then given by

$$I_C^W(\mathbf{R}) = 1 - 2\phi(\mathbf{R}) \otimes T_C^W(\mathbf{R}). \quad (23)$$

In Fig. 8(a) we display  $T^W(\mathbf{u})$  for  $\Delta f = -3.0 \mu\text{m}$ . The chromatic damping envelope  $E(\mathbf{u})$  for  $\Delta E = 0.3 \text{ eV}$  is overlaid on the panel as a dashed line. Multiplication of these functions via Eq. (21) produces the chromatically damped CTF  $T_C^W(\mathbf{u})$  in Fig. 8(b). The resulting step contrast for the two CTFs is evaluated using Eqs. (19) and (23) and displayed in Figs. 8(c) and (d) respectively. The effect of the damped transfer function in Fig. 8(b) is to produce a step intensity profile in (d) with reduced fringe visibility compared with (c). For comparison, the intensity profile  $I_C(\mathbf{R})$  obtained from the full averaging process in Eq. (15) is displayed as a dashed line in Fig. 8(d), but is difficult to see as it is so close to  $I_C^W(\mathbf{R})$ . This shows that the use of an envelope function and evaluation of the intensity via Eq. (23) is an excellent approximation to the full treatment of Eq. (15). Furthermore, we have confirmed for a wide range of defocus and energy spread that the envelope function treatment provides good agreement with the full defocus averaging

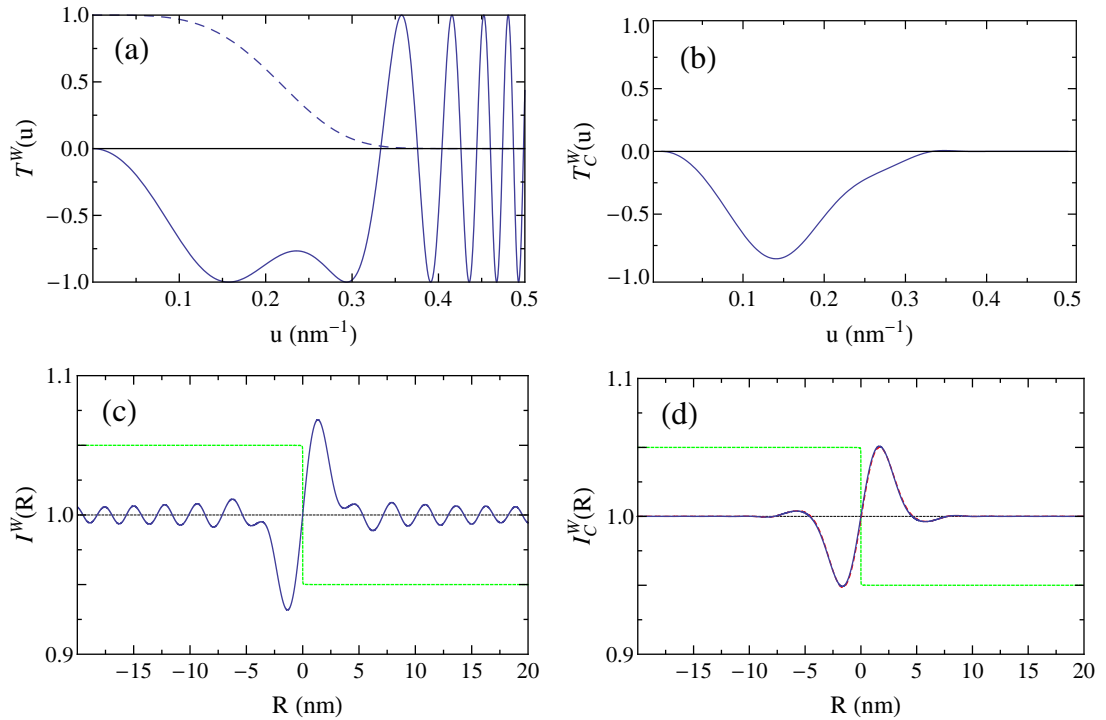


Figure 8: (a)  $T^W(\mathbf{u})$  for  $\Delta f = -3.0 \mu\text{m}$ . The chromatic envelope  $E(\mathbf{u})$  for  $\Delta E = 0.3$  eV is overlaid as a dashed-line. (b) Chromatically damped CTF  $T_C^W(\mathbf{u})$ . (c)  $I^W(\mathbf{R})$  evaluated for the dotted-line step profile shown and a WPO step phase change of 0.1. (d)  $I_C^W(\mathbf{R})$  (solid line) for a WPO step phase change of 0.1 radians. The intensity profile  $I_C(\mathbf{R})$  evaluated with the full incoherent averaging process is superimposed as a dashed line, but is difficult to see as it is so close to  $I_C^W(\mathbf{R})$ .

approach within the WPO regime.

Given the interpretive value of the envelope function approximation in Eq. (22) and its computational advantages over the full averaging approach in Eq. (15), it is interesting to examine its validity for strong phase objects. In such cases, a first order expansion in terms of  $\phi(\mathbf{R})$  (Eq. (2)) is not valid, but we can readily modify Eq. (9) to obtain the chromatically damped CTF

$$T_C^E(\mathbf{u}) = A(\mathbf{u})B(\mathbf{u})E(\mathbf{u}). \quad (24)$$

Eq. (13), the electron wavefunction in the back-focal plane of the effective objective lens, then becomes

$$\psi(\mathbf{u}) = O(\mathbf{u})A(\mathbf{u}) \exp(i\chi(\mathbf{u})) \exp(-\pi^2\lambda^2\sigma^2u^4/2). \quad (25)$$

The LEEM image contrast  $I_C^E(\mathbf{u})$ , which incorporates chromatic aberration via the envelope approximation, is then evaluated from the modulus squared of the inverse Fourier transform of  $\psi(\mathbf{u})$  given by Eq. (25).

In Fig. 9 we compare simulations of  $I_C^E(\mathbf{R})$  (solid line) evaluated via Eq. (25) with the defocused averaged  $I_C(\mathbf{R})$  (dashed line) evaluated via Eq. (15) for two non-WPO values

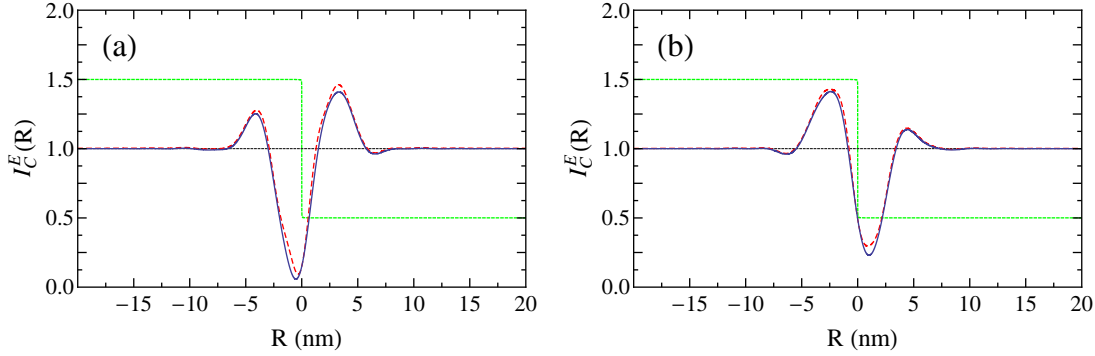


Figure 9: Comparison of intensity profile obtained via the chromatic envelope approximation  $I_C^E(\mathbf{R})$  (solid line) with the defocused averaged value  $I_C(\mathbf{R})$  (dashed line) for a step phase difference of (a)  $(3\pi/4 + 2\pi)$  and (b)  $(3\pi/2 + 2\pi)$ . In both cases the step profile is shown as a dotted-line.

of step phase difference. It can be seen that there is excellent agreement between the two methods. Indeed we have confirmed this is the case for a wide range of defocus and phase difference up to  $100\pi$ . This suggests that the computationally efficient damping envelope approach can be usefully applied to qualitatively simulate LEEM step contrast, even for the case of strong phase objects.

Given the intuitive interpretation of  $T_C^W(\mathbf{u})$  it is instructive to examine its general form as a function of defocus. In conventional high energy transmission electron microscopy of weak phase objects it is customary to optimise imaging conditions by using the Scherzer defocus  $\Delta f_{SC}$ .<sup>14</sup> Under these conditions, the CTF has nearly constant phase out to the first crossover which defines the instrument point resolution (see Fig. 8(a)).<sup>14</sup> However, it can be seen in Fig. 8(b) that for LEEM the chromatic aberration envelope  $E(\mathbf{u})$  significantly suppresses the form of  $T_C^W(\mathbf{u})$ , particularly at spatial frequencies close to the point resolution. Therefore, to enhance the visibility of WPOs it may be more appropriate to use greater values of defocus and tune the CTF passbands to specific spatial frequencies inherent in the WPO. Such higher defocus passbands can be observed in panels (a) and (b) of Fig. 10.

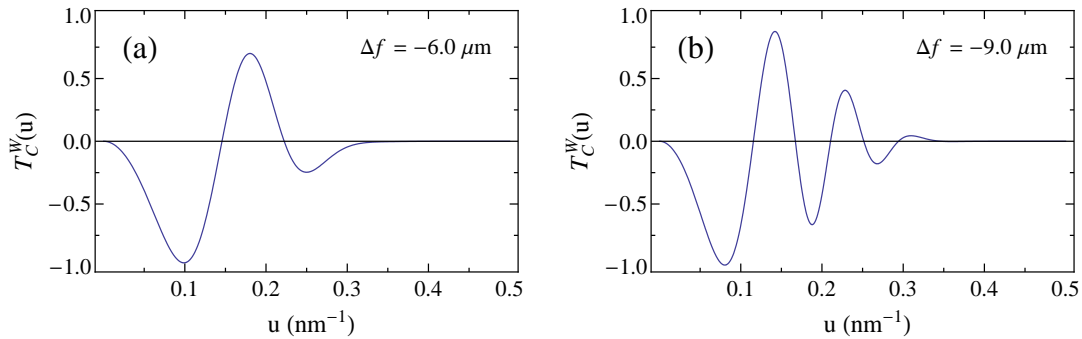


Figure 10:  $T_C^W(\mathbf{u})$  for defocus values (a)  $2\Delta f_{SC}$  and (b)  $3\Delta f_{SC}$  where  $\Delta f_{SC} = -3.0 \mu\text{m}$ .

## 8. Conclusions

We have presented a wave optical treatment of surface step contrast in LEEM. Although the method neglects contrast arising from step strain or electron penetration below the surface, it has the advantage that conventional transfer function theory can be applied and used to interpret the image contrast. In particular, the use of a damping envelope to treat chromatic aberration appears to provide a good approximation to the full treatment involving an incoherent averaging of intensities. The method is readily extended to 2D geometries and we anticipate an increased use of such simulations as aberration corrected LEEMs are developed.

## Acknowledgments

S.M.K. and N.E.S. acknowledge funding from the J. L. William Bequest. D.M.P. and D.E.J. acknowledge funding from the Australian Research Council.

## Appendix

In the methods discussed in this paper, we evaluate Fourier transforms numerically using a discrete array to represent the continuous phase variation across the cathode surface. As discussed by Press *et al.*<sup>20</sup> this array must cover a sufficiently large range of  $\mathbf{R}$  values in real space and  $\mathbf{u}$  values in reciprocal space to prevent aliasing.

We must also be careful to sample both real space ( $O(\mathbf{R})$ ) and reciprocal space functions ( $T(\mathbf{u})$ ) finely enough, that is, the interval size between array points ( $\Delta R$  in real space,  $\Delta u$  in reciprocal space) must be sufficiently small that any spatial variation in a function is accurately sampled by the discrete array.

This is particularly important in computing  $\psi(\mathbf{u})$  via Eq. (13), where we multiply the Fourier transform  $O(\mathbf{u})$  by  $B(\mathbf{u})$ . The real and imaginary components of  $B(\mathbf{u})$  vary between -1 and 1 at an increasingly rapid rate as  $\mathbf{u}$  increases, as seen in Fig. 4. With the contrast aperture in Eq. (10) set sufficiently high (i.e. beyond the point resolution), we find that the maximum reciprocal space gradient of  $\chi(\mathbf{u})$  (see Eq. (11)),  $\chi'_{max}$ , is typically at  $u_A$

$$\chi'_{max} = \left. \frac{d\chi(u)}{du} \right|_{u=u_A}. \quad (\text{A.1})$$

We note that a range of negative defocus values exists which produces a local minimum in  $\chi(\mathbf{u})$  close to  $u_A$ , moving  $\chi'_{max}$  to  $u < u_A$ . However for the aberration coefficients described in Eq. (12), this range is several microns either side of  $\Delta f = -C_S \lambda^2 u_A^2 \approx -20 \mu\text{m}$ , which is outside the typical defocus values used.

To properly sample the function  $\chi(\mathbf{u})$  and hence  $B(\mathbf{u})$ , we require that the interval size in reciprocal space  $\Delta u$  is small enough that the variation in  $\chi(\mathbf{u})$  is at most  $\pi$  between adjacent array points in one dimension<sup>20</sup>

$$\pi \geq \chi'_{max} \Delta u, \quad \Rightarrow \Delta u \leq \pi / \chi'_{max}, \quad (\text{A.2})$$

setting an upper limit for  $\Delta u$ . The real space interval size  $\Delta R$  is related to the reciprocal space interval via<sup>20</sup>

$$\Delta R = 1 / (n \Delta u), \quad (\text{A.3})$$

where  $n$  is the array size in real and reciprocal space in one dimension. The proper sampling of  $B(\mathbf{u})$  therefore requires

$$\Delta R \geq \chi'_{max}/(n\pi), \quad (\text{A.4})$$

setting a lower limit to the interval size in real space. To ensure the real space function  $O(\mathbf{R})$  is properly sampled, we may increase the array size  $n$  to reduce the allowed  $\Delta R$ , without introducing numerical artifacts by incorrectly sampling in reciprocal space.

Note also that  $n$  must be large enough to include the full range of  $T(\mathbf{u})$  up to  $u_A$ , which requires

$$n \geq u_A/\Delta u. \quad (\text{A.5})$$

Minimizing computation time is also important, for example a fast Fourier transform algorithm benefits from using an array of size  $2^m$  for some integer  $m$ .<sup>20</sup> We can use the above guidelines to choose appropriate array and interval sizes, whilst incorporating practical considerations to aid interpretation (e.g. interval sizes with one significant figure).

1. E. Bauer, *Rep. Prog. Phys.* **57**, 895 (1994)
2. R. M. Tromp and J. B. Hannon, *Surf. Rev. & Lett.* **9** 1565 (2002)
3. W. F. Chung and M. S. Altman, *Ultramicroscopy* **74** 237 (1998)
4. M. S. Altman, W. F. Chung and C. H. Liu, *Surf. Rev. Lett.* **5** 1129 (1998)
5. G. F. Rempfer and O. H. Griffith, *Ultramicroscopy* **47** 35 (1992)
6. R. M. Tromp and M. C. Reuter, *Ultramicroscopy* **50** 171 (1993)
7. R. Fink *et al.*, *J. Elect. Spectrosc. Relat. Phenom.* **84** 231 (1997)
8. J. M. Cowley, *Diffraction Physics* third revised ed. (North-Holland, Amsterdam, 1995)
9. S. A. Nepijko, N. N. Sedov, G. Schönhense, M. Escher, X. Bao and W. Huang, *Ann. Phys.* **9** 441 (2000)
10. D. E. Jesson, K. M. Pavlov, M. J. Morgan and B. F. Usher, *Phys. Rev. Lett.* **99** 016103 (2007)
11. E. Bauer, *Ultramicroscopy* **17** 51 (1985)
12. Z. Shao and A. V. Crewe, *Ultramicroscopy* **31** 199 (1989)
13. J. W. Goodman, *Introduction to Fourier Optics* third ed. (Roberts & Company Publishers, Greenwood Village, Colorado, 2005)
14. D. B. Williams and C. B. Carter, *Transmission Electron Microscopy* (Plenum Press, New York, 1996) pp. 459 - 469
15. J. C. H. Spence, *Experimental High Resolution Electron Microscopy* third ed. (Oxford University Press, Oxford, 2003)
16. D. F. Lynch, A. F. Moodie and M. A. O'Keefe, *Acta Cryst.* **A31** 300 (1975)
17. P. L. Fejes, *Acta Cryst.* **A33** 109 (1977)
18. L. Reimer and H. Kohl, *Transmission Electron Microscopy* 5th ed. (Springer-Verlag, Berlin, 2008)
19. R. S. Becker, J. A. Golovchenko, E. G. McRae and B. S. Swartzentruber, *Phys. Rev. Lett.* **55** 2028 (1985)
20. W. H. Press, S. A. Teukolsky, W. T. Vetterling and B. P. Flannery, *Numerical Recipes* third ed. (Cambridge University Press, New York, 2007)
21. O. Scherzer, *J. Appl. Phys.* **20** 20 (1948)
22. G. Toraldo Di Francia, *J. Opt. Soc. Am.* **45** 497 (1955)
23. G. S. Bales and A. Zangwill, *Phys. Rev. B* **41** 5500 (1990)
24. T. Frisch and A. Verga, *Phys. Rev. Lett.* **96** 166104 (2006)
25. K. M. Chen, D. E. Jesson, S. J. Pennycook, M. Mostoller, T. Kaplan, T. Thundat and R. M. Warmack, *Phys. Rev. Lett.* **75** 1582 (1995)
26. L. J. Allen, M. P. Oxley and D. M. Paganin, *Phys. Rev. Lett.* **87** 123902 (2001)
27. D. M. Paganin and T. E. Gureyev, *Opt. Commun.* **281** 965 (2008)

---

## Phase retrieval low energy electron microscopy

This chapter is an author generated post print of the article

R. P. Yu, S. M. Kennedy, D. M. Paganin and D. E. Jesson, 'Phase retrieval low energy electron microscopy,' *Micron*, **41** (2010) 232–238, available electronically at <http://www.elsevier.com/locate/micron> or via doi:10.1016/j.micron.2009.10.010.



## Declaration for thesis chapter 'Phase retrieval low energy electron microscopy.'

### Declaration by candidate

For this chapter, the nature and extent of my contribution to the work was the following:

Nature of contribution	Extent of contribution (%)
Provided the parameters and model (i.e. the contrast transfer function) for the forward problem, co-wrote and provided technical expertise.	30

The following co-authors contributed to the work. Co-authors who are students at Monash University must also indicate the extent of their contribution in percentage terms:

Name	Nature of contribution	Extent of contribution (%) for student co-authors only
Rotha Yu	Applied phase retrieval methods to the model, performed the phase retrieval calculations, produced the majority of the images, co-wrote the paper.	(first author)
David Paganin	Co-wrote, produced the first two images, and provided technical expertise.	
David Jesson	Co-wrote and provided technical expertise.	

Candidate's Signature		Date 23/8/10
-----------------------	---	--------------

### Declaration by co-authors

The undersigned hereby certify that:

- (1) the above declaration correctly reflects the nature and extent of the candidate's contribution to this work, and the nature of the contribution of each of the co-authors.
- (2) they meet the criteria for authorship in that they have participated in the conception, execution, or interpretation, of at least that part of the publication in their field of expertise;
- (3) they take public responsibility for their part of the publication, except for the responsible author who accepts overall responsibility for the publication;
- (4) there are no other authors of the publication according to these criteria;
- (5) potential conflicts of interest have been disclosed to (a) granting bodies, (b) the editor or publisher of journals or other publications, and (c) the head of the responsible academic unit; and
- (6) the original data are stored at the following location(s) and will be held for at least five years from the date indicated below:

Location(s)

Signature 1		Date 23/8/10
Signature 2		26/8/2010
Signature 3		26-8-10



# Phase Retrieval Low Energy Electron Microscopy

R. P. Yu, S. M. Kennedy, D. M. Paganin, and D. E. Jesson

*School of Physics, Monash University, Victoria 3800, Australia*

---

## Abstract

We consider the utility of phase-retrieval methods in low energy electron microscopy (LEEM). Computer simulations are presented, demonstrating recovery of the terraced height profile of atomic steps. This recovery uses phase retrieval to decode a single LEEM image, incorporating the effects of defocus, spherical aberration and chromatic aberration. The ability of the method, to obtain temporal sequences of evolving step profiles from a single LEEM movie, is discussed.

*Key words:* Low energy electron microscopy (LEEM), phase contrast imaging, phase retrieval

*PACS:* 42.30.Rx, 61.72.Ff

---

## 1. Introduction

Numerous phase-retrieval methods have been developed which enable reconstruction of the phase and/or amplitude of a two-dimensional coherent complex scalar wavefield, given a series of one or more intensity maps that are output by a specified optical imaging system. Examples of such well-established phase-retrieval techniques include the recovery of a two-dimensional stationary-state complex scalar electron wavefunction from a through-focal-series of transmission electron microscope (TEM) images (Op de Beeck et al., 1996; Meyer et al., 2000; Allen and Oxley, 2001), phase-amplitude retrieval using the transport-of-intensity equation (Teague, 1983; Paganin and Nugent, 1998; Bajt et al., 2000), coherent diffractive imaging (Miao et al., 1999; Spence, 2007), Fourier holography (Eisebitt et al., 2004) and ptychography (Faulkner and Rodenburg, 2004; Rodenburg 2004).

Such phase-retrieval methods may be generally viewed as serving to decode the phase and/or amplitude of a given input coherent field  $\psi_{\text{in}}(\mathbf{R}, t)$  ( $\mathbf{R}$  denotes spatial coordinates perpendicular to the optic axis, and  $t$  denotes time),

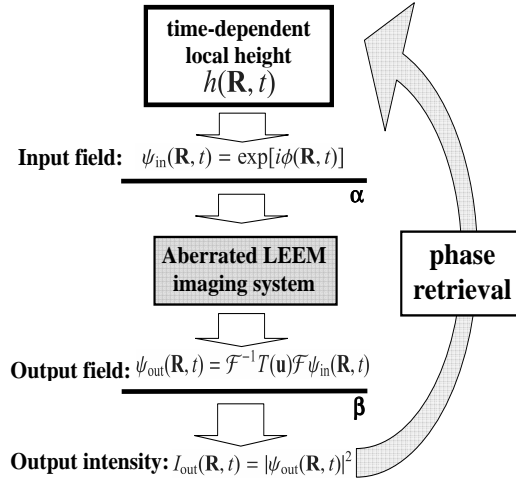


Figure 1: Flowchart for LEEM phase retrieval. The time-dependent local crystal-surface step height  $h(\mathbf{R}, t)$  yields the complex field  $\psi_{\text{in}}(\mathbf{R}, t)$  that is input into a LEEM imaging system. The aberrations of the LEEM are quantified via the transfer function  $T(\mathbf{u})$  [see Eq. (3)]. The squared modulus of the output complex field  $\psi_{\text{out}}(\mathbf{R}, t)$  is the measured LEEM movie  $I_{\text{out}}(\mathbf{R}, t)$ . Phase retrieval seeks to invert the above process of image formation, by obtaining  $h(\mathbf{R}, t)$  as a function of both  $I_{\text{out}}(\mathbf{R}, t)$ , and the known aberrations (defocus, spherical aberration, chromatic aberration *etc.*) of the LEEM system.

which is encrypted in the series  $\{|\psi_{\text{out}}^{(1)}(\mathbf{R}, t)|^2, |\psi_{\text{out}}^{(2)}(\mathbf{R}, t)|^2, \dots\}$  of one or more output intensities that are measured using a given optical system. Having recovered the phase and amplitude of  $\psi_{\text{in}}(\mathbf{R}, t)$ , one may then consider the second inverse problem of what information this yields regarding a sample of interest that lies upstream of  $\psi_{\text{in}}(\mathbf{R}, t)$  (cf. Fig. 1).

Importantly, the effects of aberrations (defocus, spherical aberration, astigmatism, chromatic aberration *etc.*) may also be incorporated into phase-retrieval algorithms, as such aberrations may be considered to merely alter the means by which the phase and amplitude, of the input field  $\psi_{\text{in}}(\mathbf{R}, t)$  over the plane  $\alpha$ , is coded in the corresponding output intensity map(s)  $I_{\text{out}}(\mathbf{R}, t)$  over the plane  $\beta$  (Allen *et al.*, 2001; Paganin and Gureyev, 2008) (see Fig. 1).

Indeed, the aberrations of a coherent imaging system may be viewed in a positive light: if the input wavefield is transversely uniform in intensity, so that it may be written as  $\psi_{\text{in}}(\mathbf{R}, t) = A \exp[i\phi(\mathbf{R}, t)]$  for constant amplitude  $A$  and (real) phase  $\phi(\mathbf{R}, t)$ , then aberrations are *necessary* to visualize input phase variations  $\phi(\mathbf{R}, t)$  as intensity variations of the resulting output maps,

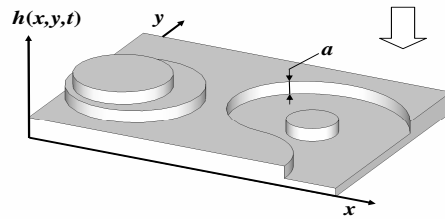


Figure 2: Schematic of atomic-height terraced steps on a crystalline surface. The height of a single step is denoted by  $a$ , with the local height of the surface denoted by  $h(x, y, t) \equiv h(\mathbf{R}, t)$ . Direction of incident electrons given by white arrow.

since a “perfect” imaging system would merely reproduce the featureless intensity of the input field (see e.g. Paganin and Gureyev, 2008; cf. Urban, 2009). A classic example of this is the very low contrast observed in focussed bright-field optical micrographs of colorless transparent objects; the contrast of such images may be greatly increased by the deliberate constructive introduction of “aberrations” such as those furnished by back-focal-plane filters (e.g. in Zernike phase contrast or Schlieren imaging), or by defocus (Zernike, 1942).

In parallel with and in isolation from the above developments, low energy electron microscopy (LEEM) has emerged as a tool routinely used to image the dynamics of terraced steps on crystal surfaces (Bauer, 1994) (see Fig. 2). Although the typical lateral resolution of LEEM is around 5 nm, atomic-layer high surface steps can be imaged via phase contrast methods which exploit the variation in phase of the incident electron wave as it is reflected in the vicinity of the step edge (Chung and Altman, 1998). Surface steps underpin many phenomena in surface science and the capability of LEEM to image step positions in real-time has made major contributions to understanding epitaxial growth (Świąch and Bauer, 1991), surface thermodynamics (Bartelt et al., 1994) and morphological evolution (Tanaka et al., 1997).

It is timely that the concepts and methods of phase retrieval be applied to surface electron microscopy. We demonstrate the utility of this union, by exploring the use of phase-retrieval methods to determine both the positions and heights of step edges directly from LEEM images. Our aim is to examine the possibility of extracting information for a single LEEM imaging

parameter-set (e.g. particular fixed values of defocus, spherical aberration, chromatic aberration etc.) so as to facilitate the systematic quantitative reconstruction of dynamic events from LEEM movies. Applying a variant of the Gerchberg–Saxton (GS) method (Gerchberg and Saxton, 1972) to an idealized LEEM system, we demonstrate how a system of steps and terraces can be reconstructed from a single aberrated LEEM image. We discuss factors limiting the resolution of the reconstruction method in typical cases and potential applications to image reconstruction from energy filtered images.

## 2. LEEM imaging system and transfer function

To describe LEEM step contrast we follow the wave-optical approach of Kennedy et al. (2009) in which an arrangement of steps and terraces is represented by a phase object function which transversely modulates the phase but not the amplitude of the reflected electrons, the phase modulation being proportional to the negative of the local height of the probed surface (cf. Chung and Altman, 1998; Pang et al., 2009).

For specimens having a local surface (step) height  $h(\mathbf{R}, t)$ , and assuming normally-incident plane-wave illumination, reflected electrons experience a relative transverse phase shift given by

$$\phi(\mathbf{R}, t) = -\frac{4\pi}{\lambda_i}h(\mathbf{R}, t) \equiv \frac{4\pi a}{\lambda_i}S(\mathbf{R}, t). \quad (1)$$

Here,  $a$  is the step height,  $\lambda_i$  is the wavelength of the incident electron field, and  $S(\mathbf{R}, t)$  is a shape-function indicating the number of steps the wavefield at position  $\mathbf{R}$  experiences when reflected from the surface. Note that in this paper our shape function will consist only of integer values for the idealized, but often typical, case of one type of step of height  $a$ ; however, our phase-retrieval model is not reliant on this and can work with surfaces consisting of steps of different height. Note also that an increased height  $h(\mathbf{R}, t)$  implies a reduced phase  $\phi(\mathbf{R}, t)$  in the reflected electrons (see e.g., Kennedy et al., 2009).

Under the above approximations, the wavefield reflected from the surface is

$$\psi_{\text{in}}(\mathbf{R}, t) = \exp[i\phi(\mathbf{R}, t)], \quad (2)$$

where we have ignored a trivial phase factor that is linear in time. The field  $\psi_{\text{in}}(\mathbf{R}, t)$ , which constitutes the input wavefield for the LEEM imaging system

(cf. Fig. 1), is assumed to be a pure phase object, i.e., a complex object with unit amplitude.

The cathode immersion lens and the objective lens of the LEEM imaging system modify this input wavefield. Under the assumption that the LEEM is a linear shift-invariant imaging system (Goodman, 2005), the input spatial wavefunction  $\psi_{\text{in}}(\mathbf{R})$  at some fixed time, and henceforth dropping explicit functional  $t$  dependence, may be related to the output wavefunction  $\psi_{\text{out}}(\mathbf{R})$  via (see e.g. Paganin and Gureyev, 2008)

$$\psi_{\text{out}}(\mathbf{R}) = \mathcal{F}^{-1}T(\mathbf{u})\mathcal{F}\psi_{\text{in}}(\mathbf{R}). \quad (3)$$

Here,  $\mathbf{u}$  is the Fourier-space coordinate dual to  $\mathbf{R}$ ,  $\mathcal{F}$  is the two-dimensional Fourier transform operator,  $\mathcal{F}^{-1}$  is the corresponding inverse Fourier transformation,  $T(\mathbf{u})$  is the transfer function (the Fourier transform of the complex point spread function), and all operators are assumed to act from right to left. The output intensity is then

$$I_{\text{out}}(\mathbf{R}) = |\psi_{\text{out}}(\mathbf{R})|^2. \quad (4)$$

For the LEEM imaging system, the transfer function can be written as (see e.g. Cowley, 1995)

$$T(u) = \mathcal{E}(u) \exp(i\pi\Delta f \lambda u^2 + i\pi C_S \lambda^3 u^4 / 2). \quad (5)$$

Here,  $u \equiv |\mathbf{u}|$ ,  $\Delta f$  is the defocus,  $\lambda$  is the free-space electron wavelength,  $C_S$  is the spherical aberration coefficient, and  $\mathcal{E}(u)$  is the chromatic-aberration damping envelope

$$\mathcal{E}(u) = \exp(-\pi^2 \lambda^2 \sigma^2 u^4 / 2). \quad (6)$$

Here,

$$\sigma = \frac{C_C \Delta E}{E \sqrt{8 \ln 2}}, \quad (7)$$

$C_C$  is the chromatic aberration coefficient,  $E$  is the incident electron energy,  $\Delta E$  is the full width at half maximum of the electron energy distribution, and  $\sigma$  is the corresponding standard deviation (see e.g. Kennedy et al., 2009).

Note that the uniform accelerating field, objective imaging and anode aperture components of the cathode immersion lens will make separate contributions to the combined chromatic- and spherical-aberration coefficients that

quantify the effective transfer function  $T(u)$  of the LEEM. These combined aberration coefficients are (Rempfer and Griffith, 1992; Kennedy et al., 2009)

$$C_S = C_S^U + (3/2)^4 C_S^O, \quad (8)$$

$$C_C = C_C^U + (3/2)^2 C_C^O, \quad (9)$$

where a  $U$  superscript denotes the contribution of the cathode immersion lens (due to the uniform electric field in the vicinity of the imaged surface) to the combined aberration coefficients, with an  $O$  superscript denoting the contribution of the objective imaging lens.

### 3. Surface-step reconstruction using the Gerchberg-Saxton phase retrieval method

Here we employ one of the simplest phase-retrieval methods, the Gerchberg–Saxton (GS) method (Gerchberg and Saxton, 1972). In its original form, the GS algorithm uses two intensity patterns, the input intensity  $I_{\text{in}}(\mathbf{R}) = |\psi_{\text{in}}(\mathbf{R})|^2$  and the output intensity  $I_{\text{out}}(\mathbf{R}) = |\psi_{\text{out}}(\mathbf{R})|^2$  (cf. Fig. 1). While Gerchberg and Saxton originally considered the output complex field (over the plane  $\beta$ ) to be the Fourier transform of the input field (plane  $\alpha$ ), here we consider these fields to be related by the more general formula in Eq. (3). Since our input wavefield is a pure phase object, we do not need to measure  $I_{\text{in}}(\mathbf{R})$ , since we can take it to be unity.

The modified GS method starts with an initial guess for the output-plane phase of zero, yielding a first estimate  $\psi_{\text{out}}^{[1]}(\mathbf{R}) = \sqrt{I_{\text{out}}(\mathbf{R})}$  for the complex field over the detector. We then map this first iterate for the output field to a first iterate for the input field, by transforming back to the input plane  $\alpha$  using the following regularized inverse of Eq. (3):

$$\psi_{\text{in}}^{[1]}(\mathbf{R}) = \mathcal{P}\mathcal{F}^{-1}T_{\gamma}^{-1}(u)\mathcal{F}\psi_{\text{out}}^{[1]}(\mathbf{R}). \quad (10)$$

Here, the operator  $\mathcal{P}$  replaces the modulus of the function, upon which it acts, with unity. The operator  $T_{\gamma}^{-1}(u)$  is a regularized form of  $1/T(u)$ , as discussed in the closing paragraphs of this section.

Having used Eq. (10) to obtain  $\psi_{\text{in}}^{[1]}(\mathbf{R})$ , we then use Eq. (3), with  $\psi_{\text{in}}(\mathbf{R})$  replaced by  $\psi_{\text{in}}^{[1]}(\mathbf{R})$ , to map back to the output plane  $\beta$ . The resulting field then has its modulus replaced with the measured modulus  $\sqrt{I_{\text{out}}(\mathbf{R})}$ , to yield the second iterate  $\psi_{\text{out}}^{[2]}(\mathbf{R})$  for the object-plane complex field.

The above process cycles between input and output planes, imposing the known intensity in each plane, together with any other suitable constraints. This can be recursed until the current iterate for  $\psi_{\text{in}}^{[j]}(\mathbf{R})$  converges ( $j$  is an integer). A natural criterion for convergence is that the normalized root-mean-square intensity error, between the measured output intensity and the estimate  $|\mathcal{F}^{-1}T(u)\mathcal{F}\psi_{\text{in}}^{[j]}(\mathbf{R})|^2$  for this output intensity at the  $j$ th iteration, reaches an acceptably small value. The phase of the reconstructed input wavefield can then be used to estimate the height field  $h(\mathbf{R})$ , using Eq. (1).

In the context of phase-retrieval LEEM imaging of terraced steps, one may utilize the *a priori* knowledge that one is imaging steps. This constraint may then be chosen to quantize the retrieved input height map  $h(\mathbf{R})$  in the following manner: (i) construct a histogram of the height profile from the retrieved input height map; (ii) apply a maximum search algorithm on every pixel in the retrieved input height map using the height profile histogram as a search path. The maximum search algorithm is applied to a particular height value  $h(\mathbf{R})$  as follows. The height value  $h(\mathbf{R})$  corresponds to a point in the histogram of height values. We compare the point with the neighboring points in the histogram. If the point is not a local maximum, we replace it by the neighboring point that has the larger number of counts, and repeat the comparison until reaching a local maximum (this is a peak in the height histogram). We then replace the height value at  $\mathbf{R}$  with the new height value. The maximum search algorithm is applied to all pixels in the simulation frame of the retrieved input height map.

The regularized inverse transfer function  $T_\gamma^{-1}(u)$  in Eq. (10) is given by:

$$T_\gamma^{-1}(u) = \exp\left[\frac{\gamma\Lambda u^4}{\gamma + \Lambda u^4}\right] \exp(-i\pi\Delta f\lambda u^2 - i\pi C_S \lambda^3 u^4/2), \quad (11)$$

where  $\gamma^{-1}$  is a non-negative real regularization parameter and  $\Lambda \equiv \pi^2 \lambda^2 \sigma^2/2$ . Note the following limit cases of  $T_\gamma^{-1}(u)$ :

$$\lim_{\gamma \rightarrow \infty} T_\gamma^{-1}(u) = 1/T(u), \quad (12)$$

$$\lim_{\gamma \rightarrow 0^+} T_\gamma^{-1}(u) = \exp(-i\pi\Delta f\lambda u^2 - i\pi C_S \lambda^3 u^4/2). \quad (13)$$

In contrast to the unbounded operator  $T^{-1}(u)$  (whose modulus diverges with increasing  $u$  as  $\exp(\Lambda u^4)$ ), the modulus of the regularized inverse transfer function  $T_\gamma^{-1}(u)$  asymptotes to  $\exp(\gamma)$  for arbitrarily large  $u$ . This regularized deconvolution mitigates an otherwise catastrophic divergence of  $T^{-1}(u)$

with large  $u$ , the physical origin of which is an irretrievable loss of physical resolution due to the chromatic damping envelope  $\mathcal{E}(u)$ .

We close with a discussion of the choice of regularization parameter  $\gamma^{-1}$ , in light of the above comments regarding height quantization. The simplest first choice for this parameter corresponds to  $\gamma = 0$ , i.e., to the limit given by Eq. (13). This choice optimises the stability of our algorithm but it must also inevitably introduce over-smoothing since the inverse of the chromatic damping envelope  $\mathcal{E}(u)$  is ignored. However, through computational trial-and-error, we find that the post-phase-retrieval step which imposes the *a priori* knowledge that step height is quantized more than compensates for this loss of resolution. We therefore adopt  $\gamma = 0$  in our reconstruction scheme.

#### 4. Computer modelling

Here we present the results of our computer modelling, demonstrating the utility of phase retrieval in the interpretation of LEEM images. Section 4.1 models the forward problem of LEEM image formation of terraced crystalline steps in the presence of defocus, spherical aberration and chromatic aberration. Section 4.2 treats the corresponding inverse problem of using phase retrieval to decode these LEEM phase-contrast images to yield the stepped surface profile which results from the measured image contrast.

##### 4.1. The forward problem: LEEM image simulation

Our computer model uses the following parameters, with the reader referred to Kennedy et al. (2009) for details on how these parameters relate to the geometry of a contemporary LEEM system:  $\lambda = 0.0086$  nm (corresponding to  $E = 20$  keV at the objective lens),  $\lambda_i = 0.55$  nm (corresponding to electron energy 5.0 eV at sample surface),  $a = 0.036$  nm (modulo  $\lambda_i/2$ ),  $\Delta f = -3.0$   $\mu\text{m}$ ,  $C_S = 0.72$  m,  $C_C = 0.15$  m, and  $\Delta E = 0.3$  eV (Case 1, corresponding to  $\sigma = 0.93$   $\mu\text{m}$ ) or  $\Delta E = 0.05$  eV (Case 2, corresponding to  $\sigma = 0.16$   $\mu\text{m}$ ). The field of view is 100 nm  $\times$  100 nm, corresponding to 256 pixels by 256 pixels. The input stepped height profile  $h(\mathbf{R})$  is shown in Fig. 3. Here, black, gray and white respectively denote steps heights of  $-a$ , 0, and  $a$ . Using Eq. (1) implies the transverse phase modulation of the reflected electron wavefield to have a jump of magnitude 0.82 radians (modulo  $2\pi$ ) between adjacent steps, with increased height implying reduced phase. The wavefield  $\psi_{\text{in}}(\mathbf{R})$  is then computed using Eq. (2), with the corresponding image-plane intensity  $I_{\text{out}}(\mathbf{R})$  calculated using Eqs (3) and (4). To model the detection

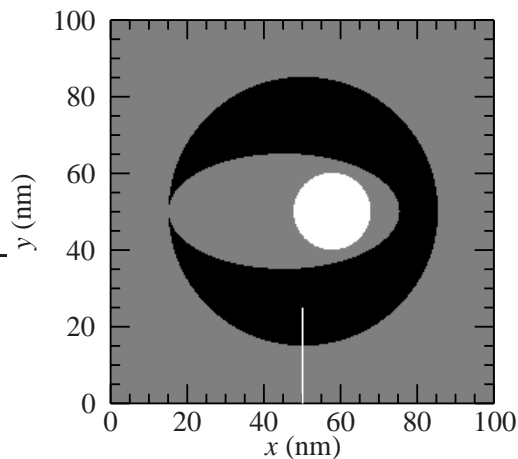


Figure 3: Terrace height-profile used as the basis for LEEM image simulation. Three surface step heights are shown: black regions correspond to  $h(\mathbf{R}) = -a$  (modulo  $\lambda_i/2$ ) and a phase value of 0.82 radians (modulo  $2\pi$ ); gray indicates  $h(\mathbf{R}) = 0$  and a phase value of 0.0 radians; white indicates  $h(\mathbf{R}) = a$  and a phase value of  $-0.82$  radians. The vertical white line, near the bottom of the figure, parametrizes the abscissae of the line profiles in Fig. 5.

process, simulated output intensity maps are degraded using pseudo-random multiplicative Poisson noise, corresponding to 5% noise in the maximum-intensity pixel. Such a noise level might typically correspond to averaging a number of sequential images, in a LEEM movie of surface dynamics which evolve significantly more slowly than the frame-capture rate. Figures 4(a) and 4(b) respectively denote the resulting output LEEM intensity maps for Case 1 and Case 2.

*Case 1.* In Fig. 4(a) a characteristic single black–white fringe is associated with surface steps, with the effects of diffraction serving to peak the intensity in the vicinity of closely-spaced steps near the left side of the figure (one of these steps is marked with white arrow  $\alpha$ ). The precise position of the closely-spaced steps, near the top and bottom of the smaller circular terrace, is also difficult to discern directly from the image due to interference (see arrow  $\beta$ ). We speak of these Case 1 simulations (with  $\Delta E = 0.3$  eV) as corresponding to a “direct edge detection regime”.

*Case 2.* In Fig. 4(b), a larger number of fringes become evident, with a bright spot formed in the center of the smaller circular terrace, on account of constructive wave interference at this point (indicated by arrow  $\gamma$  in Fig. 4(b)).

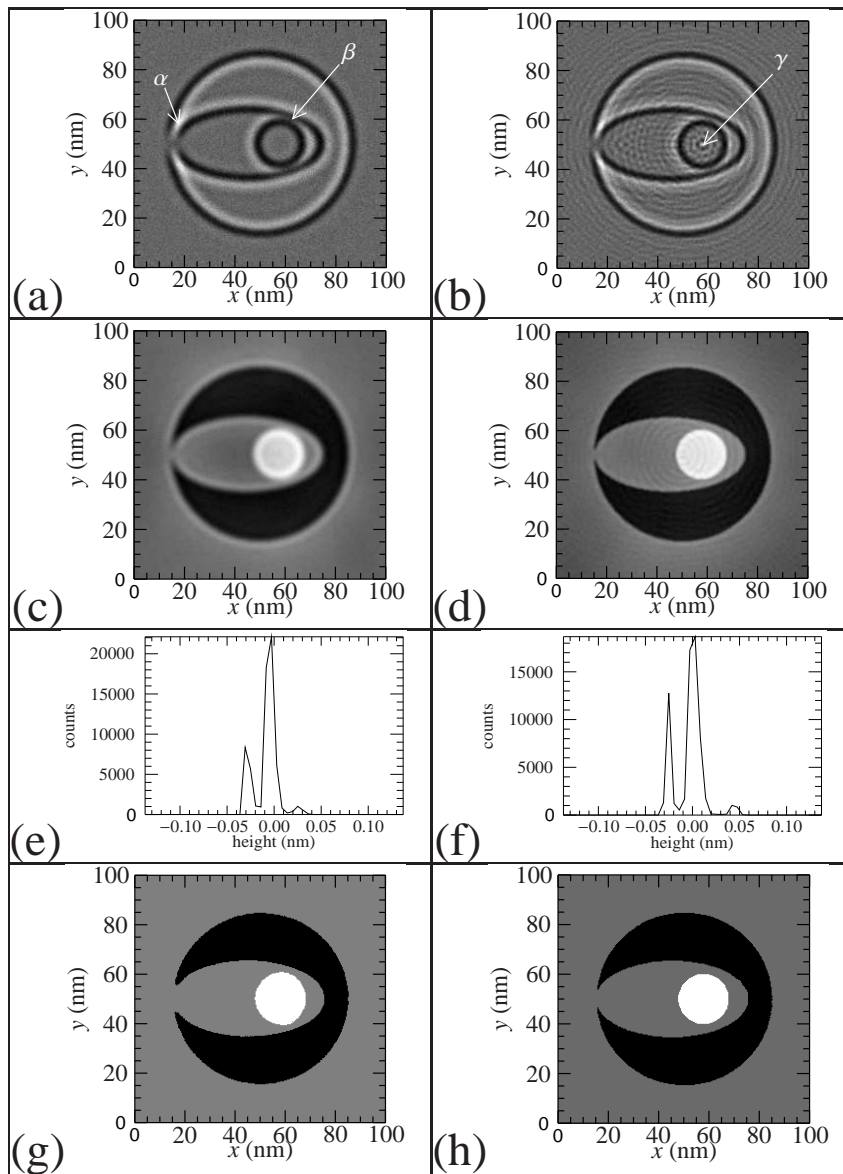


Figure 4: Simulated noisy LEEM images obtained for (a) “edge detection regime” [Case 1] and (b) “energy-filtered regime” [Case 2]—see main text for details. Taking either of these intensity maps as input, 2000 iterations of phase retrieval yielded the corresponding height reconstructions in (c) and (d), respectively. Gray-level histograms of (c, d) are given in (e, f); these histograms are then used to obtain the respective “quantized” step-height reconstructions in (g, h).

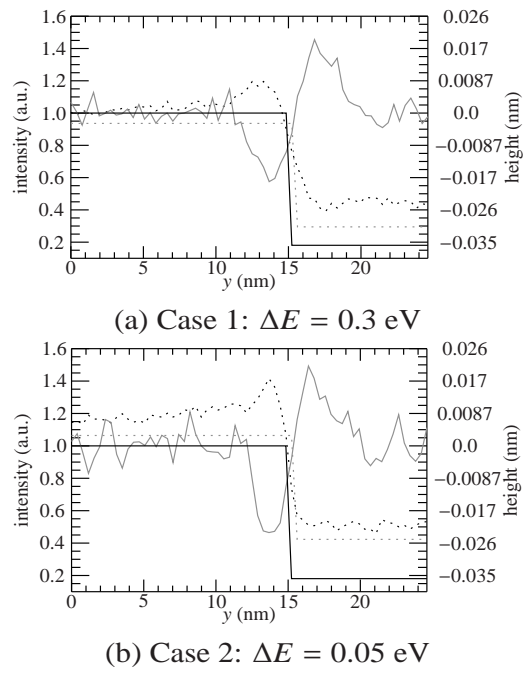


Figure 5: One-dimensional cross sections corresponding to vertical white line in Fig. 3, for (a) Case 1; (b) Case 2. In both plots, the solid black line denotes input height, the solid gray line denotes the LEEM phase-contrast image, dotted black lines denote retrieved height before quantization, and dotted gray lines denote retrieved height after quantization.

We speak of this Case 2 image (with  $\Delta E = 0.05$  eV) as corresponding to the “energy-filtered” regime. Figure 4(b) may also be interpreted as a LEEM inline hologram, in which the multiple fringes are due to the interference between the unscattered “reference” electron beam, and the scattered “object” beam.

#### 4.2. *The inverse problem: LEEM phase retrieval using the Gerchberg–Saxton algorithm*

Two thousand iterations of the phase-retrieval strategy outlined in Sec. 3 (without utilization of the *a priori* knowledge that step height is quantized) were applied to the simulated LEEM images in Figs 4(a) and (b). This yielded the input phase maps which are converted to the corresponding input height maps in Figs 4(c) and (d), respectively, using Eq. (1). The blurring of the reconstructed edges in Fig. 4(c) is commensurate with the width of the single black–white fringe in the corresponding intensity map (a), with a faint halo artefact evident in the vicinity of each of the reconstructed terrace boundaries. The situation changes for reconstruction (d) obtained using the “energy-filtered regime” image in (b); in this latter reconstruction, the resolution of the reconstructed step locations has been improved via the algorithm’s implicit utilization of the higher-spatial-frequency information that is contained in the additional diffraction fringes radiating from each of the terrace edges in (b). In particular, the cusped feature at the left of the image (corresponding to  $\alpha$  in Fig. 4(a)) is more accurately reconstructed in the energy-filtered-regime map (d). A salient point, here, is that while Fig. 4(a) contains more directly-interpretable surface morphology than Fig. 4(b), the situation is reversed on considering the corresponding phase-retrieval reconstructions in Figs 4(c) and (d), respectively.

We may proceed further with each of these reconstructions if we make use of the *a priori* knowledge that the step height is quantized. To this end, Figs 4(e) and (f) give histograms of the gray levels in Figs 4(c) and (d), respectively. Each of these histograms displays three distinct peaks, corresponding to the three different step heights in each of the phase-retrieved reconstructions. If the gray level in each pixel of the retrieved height map is replaced by the value at the local maximum in the histogram peak into which it falls, one obtains the step-height reconstructions in (g) and (h), corresponding to Case 1 and Case 2 respectively. These quantized reconstructions are comparable in the quality of their reconstruction of both terrace edges and heights,

with the exception that Case 2 provides a better reconstruction of the cusps corresponding to feature  $\alpha$  in Fig. 4(a).

Figures 4(b) and (d) illustrate the principle that LEEM phase retrieval allows one to reconstruct complex wavefield information out to the resolution limit of the imaging system, corresponding to the largest radial spatial frequency transmitted to the image plane. One is thereby able to go beyond the output-intensity information limit of directly interpretable image resolution (Paganin and Gureyev, 2008).

A related issue is the question of super-resolution, in the context of localizing step-edge positions in phase-retrieval LEEM. Comparing Fig. 3 to Figs 4(c) and (g), it is evident that quasi-super-resolution has been effected via the image-quantization procedure outlined at the end of Sec. 3. This super-resolution is more evident in the one-dimensional traces of Fig. 5(a), which use the vertical white line of Fig. 3 as abscissae. In Fig. 5(a), which corresponds to the Case 1 energy spread of  $\Delta E = 0.3$  eV, we have: a solid black line denoting the input height across a terrace, a solid gray line denoting the corresponding LEEM phase-contrast intensity, a dotted black line denoting the retrieved height, and a dotted gray line for the retrieved height after imposing the step-quantization constraint. Figure 5(b) gives the corresponding traces for the Case 2 energy spread of  $\Delta E = 0.05$  eV. In Fig. 5, it is instructive to compare the LEEM intensity contrast and the retrieved height before quantization across the terrace for Case 1 and 2. The smearing in this intensity contrast is wider for Case 1 than Case 2, implying better pre-quantization localization/resolution of the step position for Case 2. Note that the smearing blur kernel width  $\Delta$  can be estimated as the reciprocal of the half-width at half maximum of the envelope in Eq. (6), giving  $\Delta \approx 1.6 \sqrt{\lambda\sigma}$ . This yields  $\Delta = 4.6$  nm and 1.9 nm, for Case 1 and Case 2, respectively. These quantities can be compared directly with the measured blurring width obtained using the retrieved quantized step-height in Figs 4(g) and (h). By examining the blunted cusp corresponding to feature  $\alpha$  in Fig. 4(a), Figs 4(g) and (h) yield super-resolution blurring widths of 1.6 nm and 0.66 nm, for Cases 1 and 2 respectively. We see that these quantities are significantly better than the previous calculations of  $\Delta$  using the half-width at half maximum of the chromatic blurring envelopes.

Phase-retrieval LEEM is able to measure the phase step  $(4\pi a/\lambda_i)_{\text{mod}2\pi}$  associated with a terrace. For example, the Case 1 simulations yield a average phase-step of 0.64 radians, with the Case 2 simulations giving an average phase-step height of 0.77 radians. This compares favorably to the input phase-

step height of 0.82 radians, that was assumed in our model.

## 5. Discussion

The use of phase-retrieval methods to quantitatively analyze LEEM images is not restricted to the particular Gerchberg–Saxton type approach explored here. For example, if a pair of images is obtained using closely-spaced values of defocus, then transport-of-intensity (TIE) phase-retrieval methods may be applicable (see e.g. Paganin and Nugent, 1998; together with the application of the method derived there to TEM in Bajt et al., 2000). Through-focal series (TFS) of three or more images may also be used to improve the robustness of the reconstruction relative to TIE methods (Misell, 1973; Op de Beeck et al., 1996; Allen and Oxley, 2001; Gureyev et al., 2004). Importantly, such multiple-image phase-retrieval methods are able to reconstruct both the phase and the amplitude of the input field, rendering them applicable to LEEM scenarios where  $\psi_{\text{in}}(\mathbf{R})$  is not uniform in modulus (cf. Fig.1 and Eq. (2)). Having said this, a particular utility of the approach considered in the present paper is that it is able to separately analyze each frame of a phase-contrast LEEM movie, which could be directly applicable to quantitative imaging of surface step dynamics.

The phase-retrieval methodology presented in this paper directly incorporates the effects of aberrations such as spherical aberration that are intrinsic to the immersion lens of the particular LEEM system modelled in this paper (see Kennedy et al., 2009; together with references therein, for details). This raises the question as to the potential role of phase retrieval for aberration-corrected LEEM (Wichtendahl et al., 1998). In this context, we note that TEM has recently entered an “aberration corrected era”, on account of the commercial availability of spherical aberration correctors (Batson et al., 2002). The role of phase retrieval in this new TEM era has been heightened on account of the constructive use of deliberately-introduced defocus and spherical aberrations. These are used to yield a focal series input into reconstruction algorithms capable of producing both the phase and the amplitude of the exit-surface wavefunction (Urban, 2009). Similarly, we anticipate that the possible importance of phase retrieval in LEEM will not be negated by advances in the correction of LEEM aberrations.

When the approximations of Eqs (1) and (2) are invalid, requiring a more complex means for modelling the passage from the object surface to the reflected field, phase–amplitude retrieval may still be of utility in determining

the complex wavefield  $\psi_{\text{in}}(\mathbf{R})$  that is imaged by the LEEM. Such a situation may arise for example where adjacent surface structures have different reflection coefficients producing wavefield amplitude contrast (Pang et al., 2009). Having reconstructed  $\psi_{\text{in}}(\mathbf{R})$  in both phase and amplitude, e.g. using one of the multiple-image phase retrieval strategies outlined at the beginning of this section, one then has the second inverse problem of relating this complex wavefield to the surface structure which created it. Again, this idea has a direct analogue in TEM phase retrieval, where the problem of exit-wave reconstruction is to some extent independent of the complexity of the dynamical scattering processes upstream of the sample's exit surface. Finally, we note that in performing LEEM phase retrieval on a temporal sequence of phase-contrast images, any two temporally-adjacent images will be similar if the characteristic timescale of the surface evolution is significantly smaller than the frame capture rate. In this case, the phase–amplitude reconstruction of a given image can be used to seed phase retrieval for the subsequent image in the temporal sequence. This will assist the convergence of the phase retrieval.

## 6. Conclusion

Phase-retrieval concepts provide a systematic means of decoding phase-contrast LEEM images to yield quantitative maps of the surfaces which result in such images. To demonstrate this, we have shown with computer modelling that one can reconstruct the step-height profile of terraced crystalline surfaces using a single output intensity pattern from a LEEM imaging system, in which aberrations are treated using the transfer-function formalism. This opens up the potential application of phase retrieval methods to real experimental data. Only a single phase-contrast LEEM image is required for the reconstruction, facilitating the quantitative measurement of surface dynamics.

## Acknowledgments

R. P. Y. , D. M. P. , and D. E. J. acknowledge financial support from the Australian Research Council. S. M. K. acknowledges funding from the J. L. William Bequest.

## References

Allen, L. J., Oxley, M. P., 2001. Phase retrieval from series of images obtained by defocus variation. *Opt. Commun.* 199, 65–75.

- Allen, L. J., Oxley, M. P., Paganin, D. M., 2001. Computational aberration correction for an arbitrary linear imaging system. *Phys. Rev. Lett.* 87, 123902.
- Bajt, S., Barty, A., Nugent, K. A., McCartney, M., Wall, M., Paganin, D., 2000. Quantitative phase-sensitive imaging in a transmission electron microscope. *Ultramicroscopy* 83, 67–73.
- Bartelt, N. C., Tromp, R. M., Williams, E. D., 1994. Step capillary waves and equilibrium island shapes on Si(001). *Phys. Rev. Lett.* 73, 1656–1659.
- Batson, P. E., Dellby, N., Krivanek, O. L., 2002. Sub-ångstrom resolution using aberration corrected electron optics. *Nature* 418, 617–620.
- Bauer, E., 1994. Low energy electron microscopy. *Rep. Prog. Phys.* 57, 895–938.
- Chung, W. F., Altman, M. S., 1998. Step contrast in low energy electron microscopy. *Ultramicroscopy* 74, 237–246.
- Cowley, J. M., 1995. *Diffraction Physics*, third ed. North-Holland, Amsterdam.
- Eisebitt, S., Lüning, J., Schlotter, W. F., Lörger, M., Hellwig, O., Eberhardt, W., Stöhr, J., 2004. Lensless imaging of magnetic nanostructures by X-ray spectro-holography. *Nature* 432, 885–888.
- Faulkner, H. M. L., Rodenburg, J. M., 2004. Movable aperture lensless transmission microscopy: A Novel Phase Retrieval Algorithm. *Phys. Rev. Lett.* 93, 023903.
- Gerchberg, R. W., Saxton, W. O., 1972. A practical algorithm for the determination of the phase from image and diffraction plane pictures. *Optik* 35, 237–246.
- Goodman, J. W., 2005. *Introduction to Fourier Optics*, third ed. Roberts & Company Publishers, Greenwood Village.
- Gureyev, T. E., Pogany, A., Paganin, D. M., Wilkins, S. W., 2004. Linear algorithms for phase retrieval in the Fresnel region. *Opt. Commun.* 231, 53–70.

- Kennedy, S. M., Schofield, N. E., Paganin, D. M., Jesson, D. E., 2009. Wave optical treatment of surface step contrast in low energy electron microscopy. *Surf. Rev. & Lett.* 16 (in press).
- Meyer, R. R., Sloan, J., Dunin-Borkowski, R. E., Kirkland, A. I., Novotny, M. C., Bailey, S. R., Hutchison, J. L., Green, M. L. H., 2000. Discrete atom imaging of one-dimensional crystals formed within single-walled carbon nanotubes. *Science* 289, 1324–1326.
- Miao, J., Charalambous, P., Kirz, J., Sayre, D., 1999. Extending the methodology of X-ray crystallography to allow imaging of micrometre-sized non-crystalline specimens. *Nature* 400, 342–344.
- Misell, D. L., 1973. An examination of an iterative method for the solution of the phase problem in optics and electron optics: I. Test calculations. *J. Phys. D* 6, 2200–2216.
- Op de Beeck, M., Dyck, D. V., Coene, W., 1996. Wave function reconstruction in HRTEM: the parabola method. *Ultramicroscopy* 64, 167–183.
- Paganin, D. M., Gureyev, T. E., 2008. Phase contrast, phase retrieval and aberration balancing in shift-invariant linear imaging systems. *Opt. Commun.* 281, 965–981.
- Paganin, D. M., Nugent, K. A., 1998. Noninterferometric phase imaging with partially coherent light. *Phys. Rev. Lett.* 80, 2586–2589.
- Pang, A. B., Müller, T., Altman, M. S., Bauer, E., 2009. Fourier optics of image formation in LEEM. *J. Phys.: Condens. Matter* 21, 314006.
- Rempfer, G. F., Griffith, O. H., 1992. Emission microscopy and related techniques: resolution in photoelectron microscopy, low energy electron microscopy and mirror electron microscopy. *Ultramicroscopy* 47, 35–54.
- Rodenburg, J. M., Hurst, A. C., Cullis, A. G., Dobson, B. R., Pfeiffer, F., Bunk, O., David, C., Jefimovs, K., Johnson, I., 2007. Hard-x-ray lensless imaging of extended objects. *Phys. Rev. Lett.* 98, 034801.
- Spence, J. C. H., 2007. Diffractive (Lensless) Imaging, in: Hawkes, P. W., Spence, J. C. H. (Eds.), *Science of Microscopy*. Springer, New York, pp. 1196–1227.

- Świąch, W., Bauer, E., 1991. The Growth of Si on Si(100): a video-LEEM study. *Surface Sci.* 255, 219–228.
- Tanaka, S., Bartelt, N. C., Umbach, C. C., Tromp, R. M., Blakely, J. M., 1997. Step permeability and the relaxation of biperiodic gratings on Si(001). *Phys. Rev. Lett.* 78, 3342–3345.
- Teague, M. R., 1983. Deterministic phase retrieval: a Green's function solution. *J. Opt. Soc. Am.* 73, 1434–1441.
- Urban, K. W., 2009. Is science prepared for atomic-resolution electron microscopy? *Nature Mat.* 8, 260–262.
- Wichtendahl, R., Fink, R., Kühlenbeck, H., Preikszas, D., Rose, H., Spehr, R., Hartel, P., Engel, W., Schlgl, R., Freund, H.-J., Bradshaw, A., Lilienkamp, G., Schmidt, T., Bauer, E., Brenner, G., Umbach, E., 1998. SMART - an aberration-corrected XPEEM/LEEM with energy filter. *Surf. Rev. & Lett.* 5, 1249–1256.
- Zernike, F., 1942. Phase contrast, a new method for the microscopic observation of transparent objects. *Physica* 9, 686–698.

## 5.1 Addendum for phase retrieval with unknown aberration coefficients

Chapter 5 considers phase retrieval when the values of  $C_S$  and defocus are known. If the values of these and further aberration coefficients are only known within a range, the phase retrieval algorithm can be run for each parameter set, producing a series of alternate reconstructions. This may provide useful qualitative information on the specimen surface, such as upper and lower bounds of the reconstruction. Furthermore, *a priori* knowledge of the specimen may be used to narrow the range of acceptable reconstructions.

If the aberration coefficients are completely unknown, a recent paper by Yu and Paganin (2010) outlines how a through-focus series of three intensity images may be used to recover a complex coherent scalar wavefield (and hence a phase object) for a linear shift-invariant optical imaging system with unknown aberrations. This is not directly applicable to a LEEM movie sequence of images at fixed defocus, since only one defocused image is produced at each time interval. However it is suitable for dynamic events that occur on a longer time scale than that required to obtain three defocus images, as well as static specimen surfaces.

## 5.2 Addendum for the uniqueness of phase retrieval of step transitions

The results of chapter 4 and Pang et al. (2009) indicate that if a step transition or edge is very sharp, the image contrast (and hence phase retrieval) is sensitive to phase differences modulo  $2\pi$ , so that a  $\pi/2$  object is equivalent to a  $-3\pi/2$  object. However if the step edge or transition (e.g. step bunch) has a finite width or broadness, and the resolution is sufficient to detect this, then the image contrast and phase retrieval should be sensitive to the full phase difference of the surface. This is because the intermediate phase difference values across the step transition will differ for a  $\pi/2$  object and a  $-3\pi/2$  object, producing different image contrast and enabling unique phase retrieval. So in principle, for a finite step transition and sufficient resolution, phase retrieval should be unique. In lower resolution cases, however, phase retrieval of very sharp step transitions may lack uniqueness.

In general a through-focus series or energy-dependent imaging may be necessary to uniquely retrieve the phase object of the surface. In addition, since the electric field above the specimen will be uniquely different for a  $\pi/2$

object and a  $-3\pi/2$  object, MEM should distinguish between the two step transitions even if they are very sharp.

---

## Transition between short and long wavelength limits in quantum mechanical reflection from a linear potential

This chapter is an author generated post print of the article

S. M. Kennedy, D. M. Paganin, and D. E. Jesson, 'Transition between short and long wavelength limits in quantum mechanical reflection from a linear potential,' *Am. J. Phys.*, **76** (2008) 158–162, available electronically at <http://scitation.aip.org/ajp/> or via doi:10.1119/1.2805240.



### Declaration for thesis chapter 'Transition between short and long wavelength limits in quantum mechanical reflection from a linear potential.'

#### Declaration by candidate

For this chapter, the nature and extent of my contribution to the work was the following:

Nature of contribution	Extent of contribution (%)
Developed the model used in the paper, performed the image simulations, co-wrote the paper.	85

The following co-authors contributed to the work. Co-authors who are students at Monash University must also indicate the extent of their contribution in percentage terms:

Name	Nature of contribution	Extent of contribution (%) for student co-authors only
David Paganin	Co-wrote, including all of section VI, helped develop the model and provided technical expertise.	
David Jesson	Co-wrote, helped develop the model and provided technical expertise.	

Candidate's Signature



Date 26/8/10

#### Declaration by co-authors

The undersigned hereby certify that:

- (1) the above declaration correctly reflects the nature and extent of the candidate's contribution to this work, and the nature of the contribution of each of the co-authors.
- (2) they meet the criteria for authorship in that they have participated in the conception, execution, or interpretation, of at least that part of the publication in their field of expertise;
- (3) they take public responsibility for their part of the publication, except for the responsible author who accepts overall responsibility for the publication;
- (4) there are no other authors of the publication according to these criteria;
- (5) potential conflicts of interest have been disclosed to (a) granting bodies, (b) the editor or publisher of journals or other publications, and (c) the head of the responsible academic unit; and
- (6) the original data are stored at the following location(s) and will be held for at least five years from the date indicated below:

Location(s) School of Physics, Monash University, Clayton

Signature 1



Date 26/8/2010

Signature 2



26-8-10



## Transition between short and long wavelength limits in quantum mechanical reflection from a linear potential

S. M. Kennedy,\* D. M. Paganin, and D. E. Jesson  
*School of Physics, Monash University, Victoria, 3800, Australia*

The phase changes experienced by a wave reflected from an interface are a familiar fixture in introductory physics courses. Examples include the  $\pm\pi$  phase shift acquired upon reflection from a hard mirror (for example, in thin film interference patterns and Newton's rings), and the  $-\pi/2$  phase shift studied in soft mirror reflections (for example, in mirage ray paths and the WKB connection formulas). We focus on the transition between these two limits, where the phase change upon reflection evolves continuously between the limiting cases of  $-\pi$  and  $-\pi/2$ . We study a simple quantum system that exhibits this transition: a one-dimensional free electron reflected from a linear potential.

### I. INTRODUCTION

One-dimensional (1D) systems provide useful insight into a number of quantum mechanical phenomena such as wave packet dynamics,<sup>1,2</sup> barrier penetration and tunnelling,<sup>3,4</sup> and resonance effects.<sup>4,5</sup> These systems typically encapsulate the essential physical principles yet are sufficiently simple to be analyzed analytically. In this paper we explore the phase changes that occur in a wave function as it undergoes quantum mechanical reflection.

The reflection of an optical, classical, and quantum mechanical field can change the phase of the reflected wave with respect to the incident wave. This phase change is different in the long and short wavelength limits and is equal to  $\pm\pi$  and  $-\pi/2$ , respectively.

In the long wavelength limit, reflection occurs over a characteristic length scale which is much smaller than the wavelength. Such "hard mirror" reflection is exhibited by many optical systems,<sup>6</sup> such as the reflection of visible light at the sharp interface between two isotropic dielectric materials with different refractive indices. When the incident and reflected waves are both in the medium of lower refractive index, a phase shift of  $-\pi$  is acquired upon reflection.<sup>7,8</sup> Conversely, when the incident and reflected waves are both in the medium of higher refractive index, no phase change occurs upon reflection. These well known phase factors are important for understanding thin film interference in oil slicks and soap bubbles,<sup>7</sup> Newton's rings, and Lloyd's mirror.<sup>9</sup> In quantum mechanics we may consider the reflection of a plane 1D stationary state wave function from an infinitely high potential step. The solution of the time independent Schrödinger equation gives a reflection coefficient of  $-1 = \exp(\pm i\pi)$ , again yielding the hard mirror phase shift of  $\pm\pi$ .

In the short wavelength limit the wave is turned around gradually over a distance scale that is much larger than the wavelength. A phase of  $-\pi/2$  occurs upon reflection. This "soft mirror" phase shift is acquired, for example, along the curved mirage-type ray paths of glancing incidence sunlight reflected by the refractive index gradient in the air above a hot road. In a quantum context, such reflection induced phase changes occur in the connection formulas associated with the Wentzel-Brillouin-Kramers (WKB) method.<sup>6,10,11</sup> More generally, the short wavelength reflection limit is related to reflection from a slowly increasing refractive index (or potential),<sup>12</sup> with the geometrical optics or classical point particle picture predicting a high-intensity (caustic) sheet as the ray (or point

particle) is turned around.<sup>13</sup>

Between the long wavelength and short wavelength limits, there is a transition regime where the wave is reflected over a length scale comparable to the wavelength. In this transition region, the phase change upon reflection varies continuously between the soft mirror limit of  $-\pi/2$  and the hard mirror limit of  $-\pi$ .<sup>14,15</sup>

In this paper we present a 1D calculation for a mono-energetic electron reflected by a linear potential with a variable gradient. The calculation is accessible to students in a course on elementary quantum mechanics and demonstrates the richness of both the long and short wavelength limits and the transition between them.

## II. REFLECTION FROM A LINEAR POTENTIAL

Consider a free electron of energy  $\varepsilon$  and charge  $e$ , confined to one spatial dimension  $z$  that is incident from the left on the truncated linear potential

$$V(z) = \begin{cases} eEz, & z \geq 0, \\ 0, & \text{otherwise.} \end{cases} \quad (1)$$

The region  $z \geq 0$  corresponds to a uniform electric field of magnitude  $E > 0$ . The classical turning point  $z_0$  for the electron is given by

$$z_0 = \varepsilon/eE. \quad (2)$$

The classical turning point  $z_0$  gives a lower bound for the depth to which the electron wave function penetrates the region  $z \geq 0$ . We scale  $z_0$  by the reduced vacuum de Broglie wavelength of the electron,

$$\lambda_0 = \frac{\hbar}{\sqrt{2m\varepsilon}}, \quad (3)$$

where  $\hbar \equiv h/2\pi$ ,  $h$  is Planck's constant, and  $m$  is the electron mass. The scaled penetration depth defines the dimensionless parameter  $s$ , which we term the "softness" of the quantum mirror defined by Eq. (1):

$$s \equiv \frac{z_0}{\lambda_0}. \quad (4)$$

We shall see that  $s$  is the only parameter that determines the reflection coefficient for the potential in Eq. (1).

To obtain the reflection coefficient as a function of  $s$ , recall that the stationary state complex spatial wave function  $\psi(z)$  in the field-free region  $z < 0$  can be expressed as a sum of incident and reflected plane waves of energy  $\varepsilon$ :

$$\psi(z < 0) = A \exp(iz/\lambda_0) + B \exp(-iz/\lambda_0), \quad (5)$$

where  $A$  and  $B$  are the probability amplitudes of the incident and reflected plane waves, respectively. The harmonic dependence,  $\exp(-i\varepsilon t/\hbar)$ , on the time  $t$  is suppressed throughout.

For  $z \geq 0$  the electron wave function can be found by solving the time independent Schrödinger equation,<sup>16</sup>

$$\left[ \frac{d^2}{dz^2} - \frac{1}{\lambda_0^2} \left( \frac{z}{z_0} - 1 \right) \right] \psi(z \geq 0) = 0. \quad (6)$$

Because Eq. (6) is an Airy-type differential equation, the solution can be expressed as a linear combination of the Airy functions Ai and Bi.<sup>17-19</sup> The solution Bi grows without bound as  $z \rightarrow \infty$  and is unphysical, hence we have<sup>17</sup>

$$\psi(z \geq 0) = F \text{Ai} \left( s^{2/3} \left( \frac{z}{z_0} - 1 \right) \right), \quad (7)$$

where the amplitude  $F$  is complex.

We require continuity of both the wave function and its first derivative at the boundary  $z = 0$  of the two regions, and thus solve for the reflection coefficient  $B/A$  giving

$$B/A = \exp(i\phi), \quad (8)$$

where

$$\phi = 2 \tan^{-1} \left( \frac{1}{s^{1/3}} \frac{\text{Ai}'(-s^{2/3})}{\text{Ai}(-s^{2/3})} \right) \quad (9)$$

is the phase difference between the incident and reflected plane waves; a dash denotes differentiation with respect to the argument of Ai.

Equation (9) shows that the phase shift  $\phi$  is a function only of the mirror softness  $s$ , which is the classical penetration depth  $z_0$  of the mirror scaled by the reduced vacuum wavelength  $\lambda_0$  of the incident electron plane wave. A plot of  $\phi$  (modulo  $2\pi$ ) versus  $s$  is given in Fig. 1. Three distinct reflection regimes are evident: (a) the hard mirror limit where  $s \ll 1$ , (b) the soft mirror limit where  $s \gg 1$ , and (c) a transition region where  $s \approx 1$ . We examine each regime in the following sections.

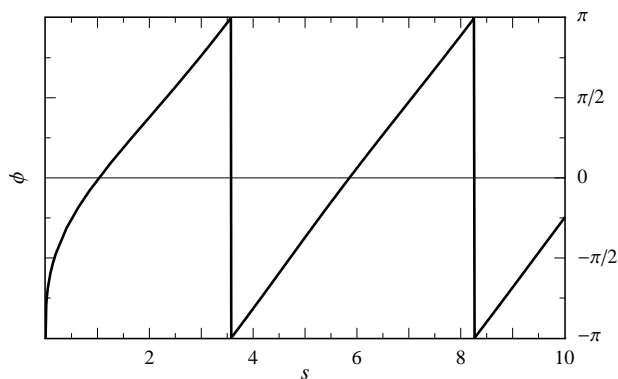


FIG. 1: Total phase shift  $\phi$  (modulo  $2\pi$ ) for plane waves reflected from the potential in Eq. (1) as a function of the softness  $s$  (see Eq. (9)).

### III. THE HARD REFLECTION LIMIT

If  $s \ll 1$ , the electron is reflected over a length scale that is short compared to its reduced vacuum de Broglie wavelength. In this long wavelength (hard reflection) limit, we see from Fig. 1 that the phase change between the incident and reflected plane waves goes to  $-\pi$  as  $s \rightarrow 0$ . This phase change of  $-\pi$  is consistent with the phase shift caused by reflection from an infinitely high step potential, to which the linear potential reduces as  $s \rightarrow 0$ . The hard reflection limit is also exemplified by the probability density in Fig. 2, calculated using Eqs. (5) and (7) for  $s = 10^{-5}$ . In this case the probability density approaches that of an electron reflected from an infinitely high step potential, where there is negligible penetration of the potential. Physically, the condition that the wave function must vanish at the mirror's edge for hard reflection is satisfied by the reflection coefficient  $B/A$  which goes to  $\exp(-i\pi) = -1$  as  $s \rightarrow 0$ , thereby yielding total destructive interference between the incident and reflected plane waves in the infinitesimal  $z < 0$  vicinity of the edge  $z = 0$  of the hard mirror.

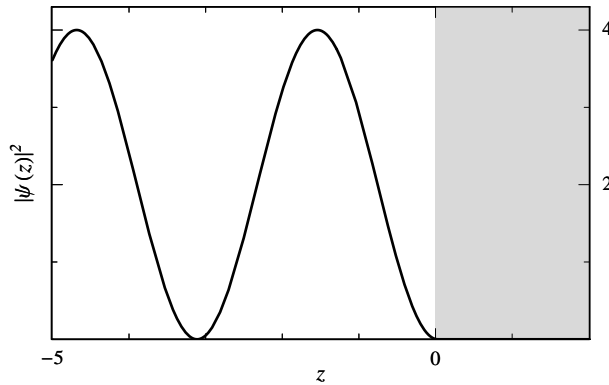


FIG. 2: Probability density of an electron reflected by a linear potential (shaded region) in the long wavelength limit, with  $s = 10^{-5}$ . The variable  $z$  is in units of  $\lambda_0$ .

### IV. THE SOFT REFLECTION LIMIT

#### A. Asymptotic expression

If  $s \gg 1$ , the electron is gradually turned around over a distance of the order of  $z_0$  which is many times larger than  $\lambda_0$ . In this short wavelength (soft reflection) limit, we see from Fig. 1 that  $\phi$  appears to vary linearly with  $s$ , modulo  $2\pi$ . More precisely, we make the approximations<sup>18</sup>

$$\text{Ai}(-\Delta) \rightarrow \pi^{-1/2} \Delta^{-1/4} \sin\left(\frac{2}{3}\Delta^{3/2} + \frac{\pi}{4}\right) \quad (10)$$

and

$$\text{Ai}'(-\Delta) \rightarrow -\pi^{-1/2} \Delta^{1/4} \cos\left(\frac{2}{3}\Delta^{3/2} + \frac{\pi}{4}\right), \quad (11)$$

corresponding to the limit  $\Delta \rightarrow \infty$ . If we use the identity

$$\tan\left(\frac{2s}{3} - \frac{\pi}{4}\right) = -1/\tan\left(\frac{2s}{3} + \frac{\pi}{4}\right), \quad (12)$$

Eq. (9) reduces to

$$\phi \rightarrow \frac{4s}{3} - \frac{\pi}{2}, \quad (s \gg 1). \quad (13)$$

We see that the total phase shift  $\phi$  in the short wavelength limit is indeed well approximated by a term varying linearly with  $s$  plus a constant shift of  $-\pi/2$ .

In contrast to hard reflection, soft reflection allows the wave function to enter the linear potential, both in the classically allowed region  $z \leq z_0$  and in the small amount of penetration beyond the classical turning point  $z > z_0$ . The oscillation of the wave function as it propagates inside the linear potential contributes to the overall returning phase of the wave function,  $\phi$  (Eq. (9)), just as the optical path length of light rays contributes to the overall phase change in the light reflected from oil slicks and soap bubbles.<sup>7</sup> We may estimate this “propagation based” contribution to the returning phase by considering the electron semi-classically with a local reduced de Broglie wavelength  $\lambda(z)$ . We invoke energy conservation and write

$$\varepsilon = \frac{(\hbar/\lambda(z))^2}{2m} + V(z). \quad (14)$$

We solve for  $\lambda(z)$  and make use of Eqs. (1)–(3) to yield

$$\lambda(z) = \frac{\lambda_0}{\sqrt{1 - (z/z_0)}}. \quad (15)$$

The accumulated phase  $\phi_p$ , due to propagation of the electron along the semi-classical path from  $z = 0$  to  $z = z_0$  and back to  $z = 0$ , is equal to  $2\pi$  times the number of local wavelengths  $\lambda(z) \equiv 2\pi\lambda(z)$  which fit into this path. Hence

$$\phi_p = 2 \int_0^{z_0} \frac{dz}{\lambda(z)} = \frac{4s}{3}, \quad (16)$$

where the last equality follows from Eqs. (4) and (15); the factor of 2 accounts for the fact that the path from  $z = 0$  to  $z = z_0$  is traversed twice. This simple argument reproduces the first term on the right-hand side of the approximate phase Eq. (13), indicating that this term is caused by the propagation of the wave function inside the potential, a “propagation based” phase change.

The factor of  $-\pi/2$  in Eq. (13) is an additional phase factor acquired upon soft reflection, which we shall call a “reflection based” phase change, and is commonly encountered in WKB semi-classical approximations for 1D quantum mechanical reflection.<sup>6,14,15,20</sup> It is instructive to discuss this additional phase change in the context of a caustic.

## B. Caustic surfaces

In classical optics caustics are the infinities of the intensity that are predicted when light rays cross one another, or at the edge of an envelope of overlapping rays.<sup>21</sup> Familiar examples include the point focus of a perfect lens and the pattern of bright lines that dance about the floor of a swimming pool on a clear sunny day. The ray theory of light predicts an infinite intensity in the vicinity of such caustics, but the infinite intensity constitutes a singularity of the theory rather than a singularity of nature. These singularities may be “tamed” by passing from

the ray theory of light to a wave theory.<sup>22</sup> In the latter the intensity of the light over the caustic regions is high and strongly peaked, but not infinite.

We now consider the classical mechanics of an ensemble of point-like electrons of energy  $\varepsilon$ , incident on the linear potential in Eq. (1). The classical particle density for this case is inversely proportional to the particle velocity as shown as the solid gray curve in Fig. 3. This curve is a fold caustic,<sup>21</sup> with the particle density approaching infinity in the vicinity of the classical turning point  $z = z_0$ .

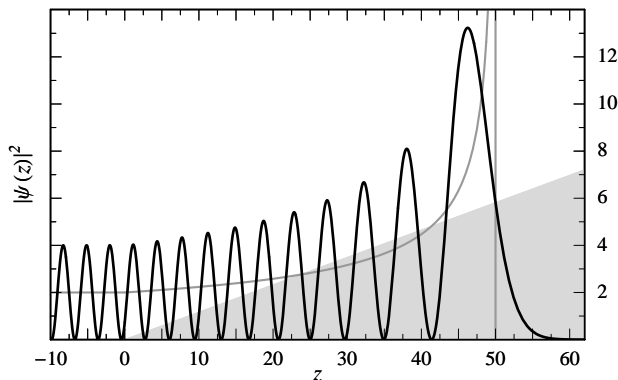


FIG. 3: Probability density of an electron reflected by a linear potential (shaded region) in the short wavelength limit, with  $s = 50$  (solid black line). The classical particle density caustic corresponding to  $s = 50$  is shown in gray, and the variable  $z$  is in units of  $\lambda_0$ .

In analogy with the transition from a ray theory to a wave theory of light, the classical density caustic is “softened” upon passage from classical point-particle mechanics to the corresponding Schrödinger wave mechanics, where the electron de Broglie wavelength is non-zero.<sup>23</sup> This softening yields the peaked probability density shown as the solid line in Fig. 3. The large peak close to  $z = z_0$  is characteristic of soft reflection from the linear potential. Figure 3 also exhibits a number of peaks between  $z = 0$  and  $z = z_0$ , which increase in height as  $z = z_0$  is approached (much as the classical density increases as seen in Fig. 3), culminating in the largest peak or softened caustic surface close to  $z = z_0$ .

### C. Soft reflection phase shift

To bring together our discussion of caustic surfaces with the soft reflection phase shift of  $-\pi/2$ , we next introduce the “confinement induced phase shift,” which is well known in quantum and classical physics. Examples include the Lévy-Leblond phase shift, in which a phase shift is induced by transversely confining a propagating wave function using a narrow tube,<sup>24,25</sup> and the Gouy phase shift for which a phase shift is induced by the transverse confinement of a collapsing spherical wave function passing through its focus.<sup>26–29</sup> The essence of such confinement induced phase shifts is contained in the position-momentum uncertainty principle,<sup>8,29,30</sup> whereby spatial confinement influences the allowed momentum distribution, in turn affecting the phase of the wave function.

The caustic surface associated with the soft reflection limit, as shown in Fig. 3, causes a high degree of longitudinal confinement of the wave function near  $z = z_0$ ,

which becomes more pronounced as  $s$  increases. It is tempting to attribute the spatial confinement at the caustic surface as the physical cause of the “reflection based” phase change of  $-\pi/2$  for the soft reflection limit. It is surprising that although the relation between the uncertainty principle and the confinement induced phase shift can be readily formalized in two spatial dimensions,<sup>24–29</sup> there appears to be no obvious analogous application in one dimension for the linear potential.

## V. THE TRANSITION REGIME

If  $s \approx 1$ , the electron is turned around over a distance of the order of its reduced vacuum de Broglie wavelength. In this transition regime between the long and short wavelength limits, we see from Fig. 1 that the phase change  $\phi$  deviates from a linear dependence on  $s$  in the short wavelength limit and continuously approaches  $-\pi$  as  $s \rightarrow 0$ .

For  $s \approx 1$  we cannot use the asymptotic expressions for the Airy functions that gave Eq. (13). It remains useful to express  $\phi$  as a sum of two terms: a propagation based or “counting wavelengths” contribution  $\phi_p = 4s/3$ , which represents the phase accumulated due to propagation within the classically allowed region of the linear potential, and  $\phi - \phi_p$ , which represents the reflection based contribution to the phase shift. The latter contribution is influenced by the softness of the reflection and is shown in Fig. 4. Figure 4 demonstrates the large  $s$  behavior of  $\phi - \phi_p$  as it asymptotically approaches the soft reflection limit of  $-\pi/2$ , the rapid approach to the hard reflection limit of  $-\pi$  as  $s \rightarrow 0^+$ , and the transition regime around  $s = 1$ .

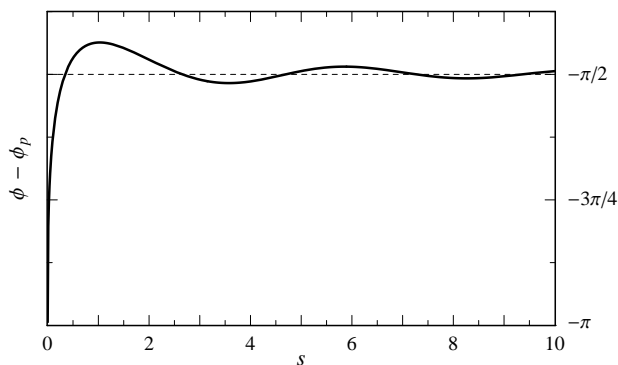


FIG. 4: Reflection based contribution to the phase  $\phi - \phi_p$  acquired upon reflection from a linear potential as a function of the softness  $s$ .

We can understand the transition regime by approaching it from the hard ( $s \ll 1$ ) and soft ( $s \gg 1$ ) reflection limits. From the hard reflection limit, small values of  $s$  allow the wave function to slightly penetrate the linear potential and relaxes the requirement for total destructive interference at  $z = 0$  (see Fig. 2). The reflection based contribution to the phase therefore varies from the hard reflection phase change of  $-\pi$  as shown in Fig. 4. From the soft reflection limit, the peak probability density in the vicinity of  $z = z_0$  decreases as  $s$  decreases, as shown in Fig. 5 for the reflections corresponding to  $s = 2$ ,  $s = 1$ , and  $s = 0.25$ . The largest

peak or caustic surface evident in Fig. 3 for  $s = 50$  is still prominent for  $s = 4$  (see Fig. 5), and note that  $\phi - \phi_p$  for  $s = 4$  is still close to the soft reflection limit of  $-\pi/2$ . This caustic “dissolves” when  $s$  becomes progressively smaller because the probability density is reduced and ejected from the potential due to the increased energy penalty inside the harder mirror. The dissolution of the caustic surface heralds a departure from the soft reflection limit of  $-\pi/2$ .

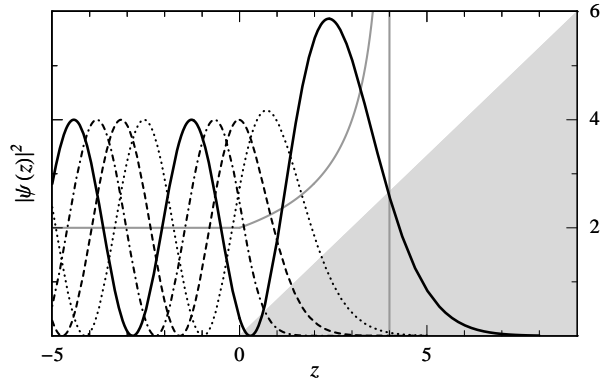


FIG. 5: Probability density of an electron in a linear potential (shaded region) for  $s = 4$  (solid black line),  $s = 2$  (dotted line),  $s = 1$  (dashed line), and  $s = 0.25$  (dot dash line). The classical particle density caustic corresponding to  $s = 4$  is shown in gray, and the variable  $z$  is in units of  $\lambda_0$ .

As well as linking the hard and soft reflection limits from a fundamental perspective, the existence of a continuous transition between the hard and soft reflection limits has interesting implications whenever a wave is reflected over length scales comparable with its wavelength. For example, the soft reflection (short wavelength) phase shift of  $-\pi/2$  appears in the connection formulas of the WKB method.<sup>6,10,11</sup> The existence of a continuous transition between hard and soft reflections suggests that the use of phase shifts between  $-\pi/2$  and  $-\pi$  may serve to significantly improve the accuracy of the WKB approximation when the electron is reflected over spatial dimensions comparable to its wavelength.<sup>14,15</sup>

## VI. SUGGESTED PROBLEMS

*Problem 1.* The linear potential in Eq. (1) may be used to describe the mirror electron microscopy mode of a low energy electron microscope.<sup>17</sup> Suppose that electrons with energy  $\varepsilon = 20$  keV are incident on a linear potential produced by an electric field of magnitude  $E = 10^7$  V/m. (a) Classically, over what distance will the electrons be “turned around” by the electric field? (b) What is the softness  $s$  of the quantum mechanical mirror associated with this system? (c) Does this value of  $s$  correspond to a soft or a hard mirror regime? (d) Quantum mechanically, how much further do the electrons penetrate the linear potential beyond the classical turning point? (e) How might the linear potential be constructed in practice? (f) Calculate the value of the amplification factor  $\Upsilon$ , defined as the ratio of the maximum probability density to the peak probability density in the region  $z < 0$  (cf. Fig. 3). (g) What incident electron energy would be required for the system to be in the transition region between the soft and hard reflection regimes?

*Problem 2.* (a) Express the time independent 1D Schrödinger equation in the presence of a real scalar potential  $V(z)$  with the spatial wave function in the polar form  $|\psi(z)|e^{i\phi(z)}$ . Separate the imaginary and real parts of the resulting expression to arrive at the equations:

$$(|\psi(z)|^2\phi'(z))' = 0, \quad (17)$$

$$\frac{(\hbar\phi'(z))^2}{2m} + V(z) - \varepsilon = \frac{\hbar^2(|\psi(z)|)''}{2m|\psi(z)|}, \quad (18)$$

where a dash denotes differentiation with respect to  $z$ . (b) Show that Eq. (17) expresses the local conservation of probability density. (c) Show that the probability current vanishes everywhere for the linear potential in Eq. (1). What is the meaning of this result? (d) Show that the right-hand side of Eq. (18) vanishes in the classical limit. The resulting expression is the Hamilton-Jacobi equation of classical mechanics for the classical action  $S(z) = \hbar\phi(z)$ .<sup>31,32</sup> This expression was key to Schrödinger’s development of wave mechanics.<sup>33</sup> (e) Use the expression from part (d) to obtain an alternative derivation for Eq. (14) to that given in Sec. IV A. Note that  $\phi(z)$  is the phase of the incident or reflected wave function, rather than the phase of the total wave function.

*Problem 3.* Instead of considering a propagating mono-energetic electron wave function that is reflected from a single linear potential of the form given by Eq. (1), consider a bound mono-energetic electron confined within a pair of soft wall linear potentials of the form

$$V(z) = \begin{cases} eE_1(z - A), & z \geq A, \\ eE_2(z + A), & z \leq -A, \\ 0, & \text{otherwise.} \end{cases} \quad (19)$$

$2A$  is a positive real number corresponding to the separation between the entry points  $z = -A$  and  $z = +A$  of the respective linear potentials, which are generated by the electric fields  $E_1 > 0$  and  $E_2 < 0$ . (a) Generalize the analysis of Secs. II–V to this case. (b) Show that the expected limit cases are recovered when either or both of  $E_1, E_2$  are infinite in magnitude, and when either or both  $E_1, E_2$  are zero. (c) Investigate the limiting case as  $A \rightarrow 0^+$ .

### Acknowledgments

S. M. K. acknowledges funding from the J. L. William Bequest. D. E. J. acknowledges funding from the Australian Research Council. All authors acknowledge useful discussions with T. E. Gureyev and K. M. Pavlov and very useful comments from the anonymous referees.

---

\* Electronic address: [Shane.Kennedy@monash.edu](mailto:Shane.Kennedy@monash.edu)

- <sup>1</sup> A. Edgar, "Reflection of wave packets from a quantum well with a tunnelling transmission resonance," *Am. J. Phys.* **63**, 136–141 (1995).
- <sup>2</sup> J. O. Hirschfelder, A. C. Christoph, and W. E. Palke, "Quantum mechanical streamlines. 1. Square potential barrier," *J. Chem. Phys.* **61**, 5435–5455 (1974).
- <sup>3</sup> N. T. Maitra and E. J. Heller, "Barrier tunnelling and reflection in the time and energy domains: The battle of the exponentials," *Phys. Rev. Lett.* **78**, 3035–3038 (1997).
- <sup>4</sup> A. P. Stamp and G. C. McIntosh, "A time-dependent study of resonant tunnelling through a double barrier," *Am. J. Phys.* **64**, 264–276 (1996).
- <sup>5</sup> R. C. Greenhow and J. A. D. Matthew, "Continuum computer solutions of the Schrödinger equation," *Am. J. Phys.* **60**, 655–663 (1992).
- <sup>6</sup> M. V. Berry and K. E. Mount, "Semiclassical approximations in wave mechanics," *Rep. Prog. Phys.* **35**, 315–397 (1972).
- <sup>7</sup> D. Halliday, R. Resnick, and J. Walker, *Fundamentals of Physics* (John Wiley & Sons, New York, 1997), 5th ed., pp. 912–913.
- <sup>8</sup> H. Römer, *Theoretical Optics* (Wiley-VCH, Weinheim, 2005), pp. 72, 156–158.
- <sup>9</sup> E. Hecht, *Optics* (Addison-Wesley Longman, Reading MA, 1998), 3rd ed., pp. 397–399.
- <sup>10</sup> B. H. Bransden and C. J. Joachain, *Quantum Mechanics* (Pearson, Sydney, 2000), 2nd ed., pp. 412–415.
- <sup>11</sup> A. Messiah, *Quantum Mechanics* (Dover, Mineola, 1999), pp. 234–239.
- <sup>12</sup> B. E. Allman, A. G. Klein, K. A. Nugent, and G. I. Opat, "Lloyd's mirage: A variant of Lloyd's mirror," *Eur. J. Phys.* **14**, 272–276 (1993).
- <sup>13</sup> D. Marcuse, "Elementary derivation of the phase shift at a caustic," *Appl. Opt.* **15**, 2949–2950 (1976).
- <sup>14</sup> H. Friedrich and J. Trost, "Nonintegral Maslov indices," *Phys. Rev. A* **54**, 1136–1145 (1996).
- <sup>15</sup> H. Friedrich and J. Trost, "Phase loss in WKB due to reflection by a potential," *Phys. Rev. Lett.* **76**, 4869–4873 (1996).
- <sup>16</sup> S. Flügge, *Practical Quantum Mechanics* (Springer-Verlag, Berlin, 1971), pp. 105–107.
- <sup>17</sup> S. M. Kennedy, D. E. Jesson, M. J. Morgan, A. E. Smith, and P. F. Barker, "Phase sensitivity of slow electrons to interactions with weak potentials," *Phys. Rev. A* **74**, 044701-1–4 (2006).
- <sup>18</sup> M. Abramowitz and I. A. Stegun, *Handbook of Mathematical Functions* (National Bureau of Standards, Washington, 1964), pp. 446–449.
- <sup>19</sup> A. S. Davydov, *Quantum Mechanics* (Pergamon Press, Oxford, 1976), 2nd ed., pp. 76–77, 113–114.
- <sup>20</sup> D. J. Griffiths, *Introduction to Quantum Mechanics* (Prentice Hall, Upper Saddle River NJ, 1995), Chap. 8.
- <sup>21</sup> J. F. Nye, *Natural Focusing and Fine Structure of Light: Caustics and Wave Dislocations* (Institute of Physics, Bristol, 1999), pp. 9–11, 46–48.
- <sup>22</sup> M. V. Berry, "Much ado about nothing: Optical dislocations lines (phase singularities, zeros, vortices ...)," in *Singular Optics*, SPIE Proceedings **3487**, edited by M. S. Soskin (SPIE International Society for Optical Engineering, Bellingham, WA, 1998), pp. 1–5.
- <sup>23</sup> M. V. Berry, "Singularities in waves and rays," in *Physics of Defects*, Les Houches, Session XXXV, edited by R. Balian, M. Kléman, and J. P. Poirier (North-Holland Press, Elsevier, 1980), pp. 453–543.

- <sup>24</sup> J.-M. Lévy-Leblond, “A geometrical quantum phase effect,” *Phys. Lett. A* **125**, 441–442 (1987).
- <sup>25</sup> D. M. Greenberger, “A new non-local effect in quantum mechanics,” *Physica B* **151**, 374–377 (1988).
- <sup>26</sup> L. G. Gouy, “Sur une propriété nouvelle des ondes lumineuses,” *Acad. Sci. Comptes Rendus* **110**, 1251–1253 (1890).
- <sup>27</sup> A. Rubinowicz, “On the anomalous propagation of phase in the focus,” *Phys. Rev.* **54**, 931–936 (1938).
- <sup>28</sup> E. H. Linfoot and E. Wolf, “Phase distribution near focus in an aberration-free diffraction image,” *Proc. Phys. Soc. London B* **69**, 823–832 (1956).
- <sup>29</sup> P. Hariharan and P. A. Robinson, “The Gouy phase shift as a geometrical quantum effect,” *J. Mod. Opt.* **43**, 219–221 (1996).
- <sup>30</sup> S. Feng and H. G. Winful, “Physical origin of the Gouy phase shift,” *Opt. Lett.* **26**, 485–487 (2001).
- <sup>31</sup> J. J. Sakurai, *Modern Quantum Mechanics* (Addison-Wesley, Reading MA, 1994), revised ed., pp. 103–105.
- <sup>32</sup> L. D. Landau and E. M. Lifshitz, *Quantum Mechanics: Non-Relativistic Theory* (Pergamon Press, Oxford, 1977), 3rd ed., pp. 51–52.
- <sup>33</sup> E. Schrödinger, “An undulatory theory of the mechanics of atoms and molecules,” *Phys. Rev.* **28**, 1049–1070 (1926).



---

## Phase sensitivity of slow electrons to interactions with weak potentials

This chapter is an author generated post print of the article

S. M. Kennedy, D. E. Jesson, M. J. Morgan, A. E. Smith, and P. F. Barker, 'Phase sensitivity of slow electrons to interactions with weak potentials,' *Phys. Rev. A* **74** (2006) 044701, available electronically at <http://pra.aps.org/> or via [doi:10.1103/PhysRevA.74.044701](https://doi.org/10.1103/PhysRevA.74.044701).



### Declaration for thesis chapter 'Phase sensitivity of slow electrons to interactions with weak potentials.'

#### Declaration by candidate

For this chapter, the nature and extent of my contribution to the work was the following:

Nature of contribution	Extent of contribution (%)
Developed the model used in the paper, performed the image simulations, co-wrote the paper.	80

The following co-authors contributed to the work. Co-authors who are students at Monash University must also indicate the extent of their contribution in percentage terms:

Name	Nature of contribution	Extent of contribution (%) for student co-authors only
David Jesson	Co-wrote, helped develop the model and provided technical expertise.	
Michael Morgan	Co-wrote, helped develop the model and provided technical expertise.	
Andrew Smith	Helped develop the model and provided technical expertise.	
Peter Barker	Provided technical expertise.	

Candidate's Signature

 Date 25/8/10

#### Declaration by co-authors

The undersigned hereby certify that:

- (1) the above declaration correctly reflects the nature and extent of the candidate's contribution to this work, and the nature of the contribution of each of the co-authors.
- (2) they meet the criteria for authorship in that they have participated in the conception, execution, or interpretation, of at least that part of the publication in their field of expertise;
- (3) they take public responsibility for their part of the publication, except for the responsible author who accepts overall responsibility for the publication;
- (4) there are no other authors of the publication according to these criteria;
- (5) potential conflicts of interest have been disclosed to (a) granting bodies, (b) the editor or publisher of journals or other publications, and (c) the head of the responsible academic unit; and
- (6) the original data are stored at the following location(s) and will be held for at least five years from the date indicated below:

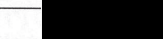
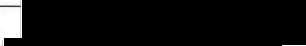
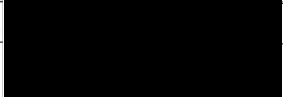
Location(s)

Signature 1

Signature 2

Signature 3

Signature 4

	Date 26-8-10
	26/08/2010
	26/8/2010
 for Prof. Barker who is a staff member at UCL (UK).	26/08/2010



## Phase sensitivity of slow electrons to interactions with weak potentials

S. M. Kennedy, D. E. Jesson,\* M. J. Morgan, and A. E. Smith  
*School of Physics, Monash University,  
Victoria, 3800, Australia.*

P. F. Barker  
*Department of Physics, School of Engineering and Physical Sciences,  
Heriot-Watt University, Edinburgh, EH144AS, UK.*

The interaction of very slow electrons with weak potentials is investigated in an exactly soluble, one-dimensional quantum mechanical model. Slow electrons are produced by a decelerating ramp potential, as in experimental mirror electron microscopy, so the electrons can interact with a weak field as they slow and reverse direction. Our model provides a wave mechanical interpretation of this turning point region and suggests the possibility of imaging optical fields utilising the phase of electron matter waves.

PACS numbers: 41.85.-p, 07.78.+s, 68.37.Nq

The phase sensitivity of very slow electrons to extremely weak potentials is of both fundamental and practical significance. It is well appreciated that a variation in phase of an electron wavefunction can be readily converted to intensity variations in the image using phase contrast electron microscopy [1]. The resulting phase change of an electron matter wave on encountering a region of uniform potential is proportional to its wavelength (see, for example [2]), which increases with decreasing electron velocity. One might therefore anticipate that slow, near stationary, electrons would have an enhanced sensitivity to very weak potentials, which may provide a basis for imaging weak fields using phase contrast methods.

In this report we consider the production of slow electrons via the well-known technique of mirror electron microscopy (MEM) [3–5]. Electrons with energy  $\sim 20$  keV are transferred from an electron source to the back focal plane of the objective lens via a magnetic sector which deflects the beam. The objective lens is the heart of the MEM system, and combines a magnetic focusing field inside the lens, with an electrostatic field between the lens and a planar cathode sample (typically a semiconductor wafer) as shown in Fig. 1. The sample, at  $z = L$ , is maintained at a potential which is slightly more negative than the electron source potential. The objective lens anode, located at  $z = 0$ , is at ground potential. The incident beam therefore traverses the magnetic part of the lens at a relatively high voltage ( $\sim 20$  kV) but is decelerated in the typically 2 mm gap between objective lens and sample until it is reflected in front of the specimen surface at  $z = z_0$ . The anode aperture has a radius which is small compared with the anode-cathode distance  $L$ , so that the electric field between the anode and cathode can be assumed uniform. Image contrast results from small perturbations in the otherwise homogeneous applied electric field between the objective lens anode and the sample cathode. This can result from surface topography or electric field variations across the sample if  $z_0$  is close enough to the sample. Following the low energy interaction and reflection from the near-sample surface region, the electrons are re-accelerated to the gun energy on their return

---

\*Electronic address: David.Jesson@monash.edu

to the objective lens, which significantly reduces lens aberrations in the imaging column so that high spatial resolution can be obtained [6]. The magnetic sector then deflects the electrons into the projector column where an image is formed.

We now consider the feasibility of imaging light beams with electrons by introducing an optical field in the proximity of the electron reflection turn around region at  $z = z_0$ . If a sufficient phase shift is induced in the slow electron matter wave then a light field can be imaged in MEM by phase contrast. The key issue is, therefore, to evaluate the phase change in the electron wave as a function of optical field strength. To investigate this we employ a simple one-dimensional quantum mechanical model which is analytically tractable. This allows for a matter wave interpretation of the classical electron turning point in MEM and facilitates the analysis of weak fields in the vicinity of the turning point using perturbation theory. We evaluate the phase change in the reflected electron matter wave as a function of field strength to provide an estimate of phase sensitivity.

The accelerating part of the MEM immersion lens consisting of a homogeneous electric field, as represented schematically in Fig. 1, can be treated separately from the (usually magnetic) imaging part [6], and this optical configuration is the basis of our imaging model. Consider an electron, of kinetic energy  $\varepsilon$  at  $z = 0$ , moving at normal incidence to the negatively charged cathode plate at  $z = L$ . Classically, the incident electron slows as it moves along the  $z$  axis towards the cathode, with the electron subject to a ramp-shaped potential energy barrier as shown in Fig. 1. The voltage difference between anode and cathode is  $\Delta V$ , so provided  $\varepsilon < e\Delta V$  (where  $e$  is the electronic charge), a classical turning point exists where the electron kinetic energy inside the potential energy barrier is zero. This occurs when the initial electron kinetic energy is equal to the potential energy of the barrier, i.e., at the point  $z_0 = \varepsilon L / e\Delta V$ , where  $0 \leq z_0 \leq L$ . Classically,  $z_0$  is the maximum distance an electron can penetrate into the potential barrier before being reaccelerated back towards the anode, with an infinite probability of finding the electron at this point because it is stationary. This suggests that slow electrons will be most susceptible to the influence of external fields near the turning point because they spend a longer time in this region. However, it remains to investigate the electron behaviour and the phase sensitivity to weak fields in the region of the turning point using wave mechanics. Consider the non-relativistic quantum mechanical behaviour of an electron of kinetic energy  $\varepsilon$  incident on a one-dimensional ramp potential energy barrier (Fig. 1). The time-independent Schrödinger equation is used to describe the incident electron [7],

$$-\frac{\hbar^2}{2m_e} \frac{d^2}{dz^2} \psi(z) + \frac{e\Delta V}{L} z \psi(z) = \varepsilon \psi(z), \quad (1)$$

where  $m_e$  is the (non-relativistic) electron mass and  $\psi(z)$  is the electron wavefunction. In a MEM experiment, it is expected that all incident electrons will turn around before the cathode, resulting in zero probability density for  $z > L$ . To solve Eq. (1) for the ramp potential it is necessary to invoke appropriate boundary conditions. So in Region III ( $z > L$ ), we choose to terminate the ramp by the constant potential shown in Fig. 1. This shape will not influence the behaviour of the electron in the vicinity of the classical turning point,  $z = z_0$ .

In Region I ( $z < 0$ ), the potential energy is zero, so the solutions to the time-independent Schrödinger equation (1) are plane waves. Assuming that the incident electron beam can be described by a single incident plane wave, the wavefunction

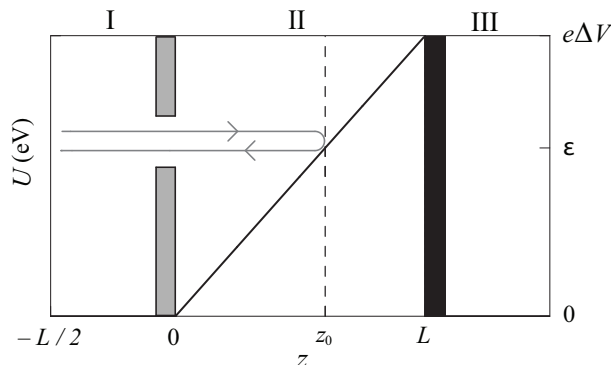


FIG. 1: Schematic of the path of an electron of energy  $\varepsilon$  in the electrostatic field region of a mirror electron microscope, from anode ( $z = 0$ ) towards a negatively charged cathode ( $z = L$ ). The potential energy barrier  $U$  experienced by the electron is also shown (solid line), and is linear with gradient  $e\Delta V/L$  and maximum height  $e\Delta V$ . At the point  $z = z_0$  the potential energy is equal to the initial kinetic energy of the electron.

in Region I is given by

$$\psi_I(z) = A \exp\left(i\frac{\sqrt{2m_e\varepsilon}}{\hbar}z\right) + B \exp\left(-i\frac{\sqrt{2m_e\varepsilon}}{\hbar}z\right), \quad z < 0, \quad (2)$$

where  $A$  and  $B$  are the probability amplitudes of the incident and reflected electron plane waves, respectively.

In Region III ( $z > L$ ), the potential is zero. It is assumed that the only source of electrons is to the left of the potential barrier ( $z < 0$ ), so there is no plane wave in Region III travelling in the negative  $z$  direction, hence

$$\psi_{III}(z) = C \exp\left(i\frac{\sqrt{2m_e\varepsilon}}{\hbar}z\right), \quad z > L, \quad (3)$$

where  $C$  is the corresponding probability amplitude.

In Region II ( $0 \leq z \leq L$ ), the time-independent Schrödinger equation (1) can be rearranged to give

$$\frac{d^2\psi_{II}(z)}{dz^2} - \frac{2m_e e\Delta V}{\hbar^2 L} \left(z - \frac{\varepsilon L}{e\Delta V}\right) \psi_{II}(z) = 0. \quad (4)$$

This differential equation has solutions consisting of two linearly independent Airy functions  $\text{Ai}(\zeta)$  and  $\text{Bi}(\zeta)$  [8], so that

$$\psi_{II}(\zeta) = F \text{Ai}(\zeta) + G \text{Bi}(\zeta), \quad (5)$$

with probability amplitudes  $F$  and  $G$ , and

$$\zeta = \left(\frac{2m_e e\Delta V}{\hbar^2 L}\right)^{1/3} \left(z - \frac{\varepsilon L}{e\Delta V}\right). \quad (6)$$

The behaviour of the linearly independent Airy functions is dictated by the proximity to  $\zeta = 0$ , which corresponds to the classical turning point  $z_0 = \varepsilon L/e\Delta V$ . The probability amplitudes are determined by demanding continuity of the wavefunction and its derivative across the boundaries at  $z = 0$

and  $z = L$ . The resulting equations make it possible to obtain expressions for  $B$ ,  $F$ ,  $G$ , and  $C$  in terms of the probability amplitude of the incident plane wave  $A$ .

We now interpret the classical electron turning point quantum mechanically using parameters which are relevant to the experimental MEM geometry. An electron with an initial kinetic energy of 20 keV, incident on a cathode held at 21 kV over a distance of  $L = 2$  mm, has a classical turning point at  $z_0 = 1.9048$  mm. The probability amplitudes of the un-normalised wavefunction are then given by  $B = \exp(-i0.773)$ ,  $F = 118\exp(-i0.387)$  and  $G = C = 0$ , where for convenience we have set  $A = 1$ . As  $C = 0$ , the electron wavefunction is zero in Region III and thus there is total reflection of the electron. In Region I, the magnitudes of the probability amplitudes  $A$  and  $B$  are equal, which produces a probability density in the form of a standing wave, with a wavelength of the order of  $10^{-12}$  m.

The probability density of the electron wavefunction close to the classical turning point ( $z = z_0$ ) is depicted in Fig. 2, which shows an increase in the wavelength as the electron approaches the classical turning point. The peak heights of the probability density are much larger than those in Region I. This represents the increased probability of finding an electron near the classical turning point, due to the lower electron velocities in this region. Interestingly, the most probable location of the electron is just before  $z = z_0$ . This is in contrast to the classical behaviour of the electron, where there is an infinite probability density at the classical turning point itself. A second departure from the classical probability

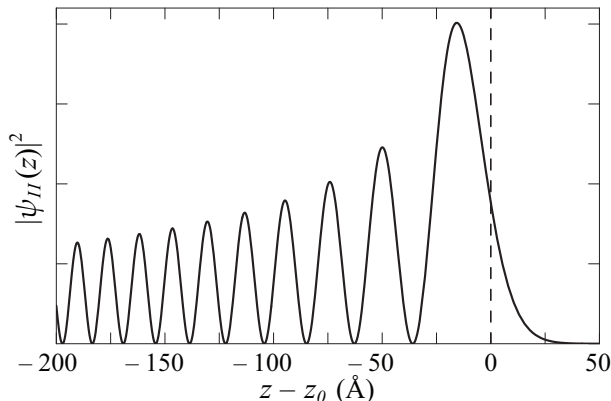


FIG. 2: The probability density of a 20 keV electron incident on a cathode held at 21 kV. The region 200 Å from the classical turning point  $z_0 = 1.9048$  mm is shown.

density is the penetration of the electron wavefunction into the potential energy barrier beyond the classical turning point. This is evident in the non-zero probability density for  $z > z_0$  in Fig. 2. However, the rapid decay of the function to zero, over a distance of 50 Å, indicates that there is a negligible probability of finding the electron well past the classical turning point and in particular, beyond the potential barrier itself, i.e.,  $z > L$ .

To investigate the phase sensitivity of the electron wavefunction to weak fields we now superpose a square perturbation of amplitude  $U_0$  on the linear potential energy barrier (see Fig. 3). This might represent a region of electrostatic or optical potential and facilitates a comparison of the phase of the electron wavefunction with the unperturbed case. The wavefunction corresponding to the situation in Fig. 3 can be written in a manner analogous to the earlier formulation. Imposing

continuity of the wavefunction and its derivative across Regions I to V yields eight equations. From these the relevant probability amplitudes can be obtained in terms of the incident amplitude,  $A$ .

The important quantity for detecting  $U_0$  by phase contrast imaging methods is

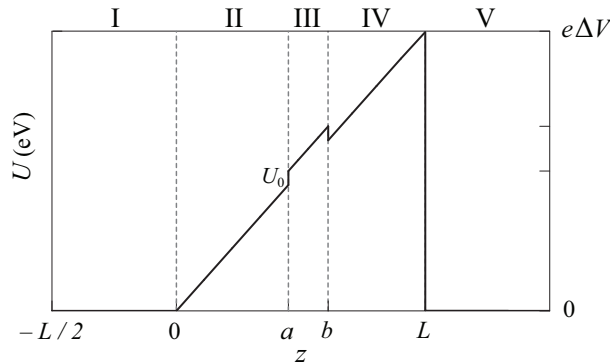


FIG. 3: One-dimensional square perturbation, of height  $U_0$ , superposed on the linear potential energy barrier. The perturbation begins at  $z = a$  and ends at  $z = b$ .

the phase of the returning electron wavefunction,  $\phi_B$ , which is obtained from the probability amplitude  $B$  in Eq. (2), where

$$B = |B|\exp(i\phi_B). \quad (7)$$

We find the greatest phase sensitivity occurs where the electron is slowest, near the classical turning point. The total phase change is therefore optimized if the back edge of the perturbation is close to  $z = z_0$ . In Fig. 4 we plot  $\phi_B$  against the perturbation amplitude  $U_0$  for such an arrangement, with a perturbation width of  $10 \mu\text{m}$ . Assuming sufficient phase contrast is attainable for  $\phi_B = 0.1 \text{ rad}$  (see, for example, [9]), MEM imaging should be sensitive to perturbations of the order of  $10 \mu\text{eV}$ . This is a remarkable result suggesting the possibility of using low energy electron microscopy to image very weak potentials.

As a specific example of imaging a weak potential, we consider the introduction of a focused pulsed laser field into the proximity of the electron turn-around region at  $z = z_0$ . Pulsed lasers require the gating or blanking of the electron beam so that only phase changes produced when the beams are present are recorded. This timing, readily attainable using standard synchronization methods, is required so that the optical potential, and thus the electron phase shift, is uniform during the imaging process. Practically, it is feasible to image 100 ns of a 200 ns pulse. Our calculations indicate that the major shift in phase occurs within a narrow region associated with the turning point. We can therefore relate the maximum laser pulse intensity  $I_{max}$  to perturbation amplitude  $U_0$  via the relation  $U_0 = e^2 I_{max} / 2m_e \omega^2 \varepsilon_0 c$  [10], where  $\varepsilon_0$  is the permittivity of free space,  $c$  is the velocity of light in vacuum and  $\omega$  is the angular frequency of the light beam. The laser pulse energy  $E$  is then given by  $E = I_{max} \sigma_t \sigma^2 (2\pi)^{3/2}$ , where  $\sigma_t$  is the temporal pulse width (200 ns) and  $\sigma$  is the beam waist (standard deviation) of  $10 \mu\text{m}$ . If we consider a light wavelength of 532 nm then for  $U_0 \approx 10 \mu\text{eV}$  we obtain a pulse energy of approximately 1 mJ. This suggests that it should be possible to image pulse energies in the  $100 \mu\text{J}$  regime for smaller beam waists and shorter pulse widths. Higher energy pulses, in the 10 mJ range, correspond to a perturbation of amplitude  $U_0 \approx 0.1 \text{ meV}$  which will produce a phase change of  $\phi_B \approx \pi/3$ , so that an intense laser field will act as a strong phase object for

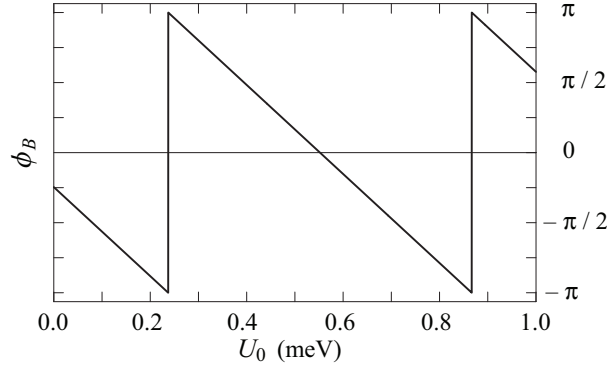


FIG. 4: Phase sensitivity  $\phi_B$  of the returning electron wavefunction, as a function of perturbation height,  $U_0$ . The  $10\ \mu\text{m}$  perturbation is positioned with the back edge adjacent to the (unperturbed) classical turning point.

imaging. This important result indicates that the electron microscopy of light is indeed feasible and that electrons will multiply scatter within a region exhibiting optical interference.

In imaging two and three dimensional perturbations, the diffraction of the electron wave will produce a spatially varying electron interference pattern in the near field. The typical lens system of a MEM allows the diffraction plane to be imaged, which facilitates the formation of both diffraction and phase contrast images. Factors restricting the imaging of optical interference patterns include the thermal spread of electron energies and beam divergence which is known to limit the ideal MEM resolution to  $15\ \text{nm}$  [11]. However, this is more than adequate to resolve typical light grating spacings of  $270\ \text{nm}$ , for example. A further consideration is the existence of patch fields resulting from spatial variations of the cathode surface [12, 13]. The patch potential may be determined by solving the corresponding Dirichlet problem for a half space [14]. For semiconductor wafers consisting of monatomic steps, we model the potential variation at the surface with a sinusoidal roughness function of amplitude  $20\ \text{nm}$  and period  $1\ \mu\text{m}$ . For a typical MEM electric field of  $\sim 10^7\ \text{V/m}$ , this produces a potential at the classical turning point of  $\ll 1\ \text{nV}$ , which is orders of magnitude smaller than the proposed optical perturbation  $U_0/e$ .

In summary, we have demonstrated the feasibility of using low energy electron microscopy to image very weak potentials by exploiting the phase sensitivity of slow electrons in the vicinity of their classical turning point. This suggests a new basis for studying fundamental interactions of electrons with optical potentials by combining light optics and electron wave optics. In particular, it should be possible to study the diffraction and Bragg regimes of electron scattering through the simulation of real space experimental MEM images of the actual spatial and angular distribution of laser light, which is presently a major short-fall in the quantification of this scattering [10]. More generally, the application of electron phase and diffraction contrast methods will provide a new means of studying fundamental aspects of the Kapitza–Dirac effect [10, 15–18].

We are grateful to Alexis Bishop for valuable discussions. S. M. K. is the recipient

of a J. L. William Postgraduate Research Scholarship. D. E. J. and M. J. M. acknowledge support from the ARC.

---

- [1] J. M. Cowley, *Diffraction physics (2nd Ed.)* (North-Holland Publishing Company, Amsterdam, 1981).
- [2] J. C. H. Spence, *Experimental high-resolution electron microscopy (3rd Ed.)* (Oxford University Press, Oxford, 1981).
- [3] A. E. Luk'yanov, G. V. Spivak, and R. S. Gvozdover, *Sov. Phys. Usp.* **16**, 529 (1974).
- [4] A. B. Bok, *Diffraction and imaging techniques in materials science (2nd Ed.)* (North-Holland, Amsterdam, 1978), vol. 2, p. 761.
- [5] M. E. Barnett and W. C. Nixon, *Optik (Stuttgart)* **26**, 310 (1967).
- [6] E. Bauer, *Ultramicroscopy* **17**, 51 (1985).
- [7] S. Flügge, *Practical quantum mechanics* (Springer-Verlag, Berlin, 1971), pp. 105–107.
- [8] M. Abramowitz and I. A. Stegun, *Handbook of mathematical functions with formulas, graphs, and mathematical tables* (United States Department of Commerce and National Bureau of Standards, 1964).
- [9] J. M. Cowley, 'Principles of image formation' in *Principles of analytical electron microscopy* (Plenum Press, New York, 1986), p. 98.
- [10] D. L. Freimund and H. Batelaan, *Phys. Rev. Lett.* **89**, 283602 (2002).
- [11] E. Bauer, *Rep. Prog. Phys.* **57**, 894 (1994).
- [12] C. Herring and M. H. Nichols, *Rev. Mod. Phys.* **21**, 185 (1949).
- [13] C. C. Speake and C. Trenkel, *Phys. Rev. Lett.* **90**, 160403 (2003).
- [14] S. A. Nepijko, N. N. Sedov, G. Schönhense, M. Escher, X. Bao, and W. Huang, *Ann. Phys. (Leipzig)* **9**, 441 (2000).
- [15] P. L. Kapitza and P. A. Dirac, *Proc. Cam. Phil. Soc.* **29**, 297 (1933).
- [16] D. L. Freimund, K. Aflatooni, and H. Batelaan, *Nature* **413**, 142 (2001).
- [17] D. L. Freimund, H. Batelaan, O. Smirnova, and M. Ivanov, *Phys. Rev. Lett.* **92**, 223601 (2004).
- [18] X. Li, J. Zhang, Z. Xu, P. Fu, D.-S. Guo, and R. R. Freeman, *Phys. Rev. Lett.* **92**, 233603 (2004).

## 7.1 Addendum for spatial coherence and the sensitivity to a finite electron energy spread

The perturbing step potential used in chapter 7 for an electron inside a standing light wave is an effective time-averaged potential known as the Ponderomotive potential (Batelaan, 2007). The Ponderomotive potential produced by a standing wave is typically proportional to  $\cos^2(k_L y)$ , where  $k_L = 2\pi/\lambda_L$ ,  $\lambda_L$  is the wavelength of the light, and the light beam propagates along the  $y$  axis. For the one dimensional case of chapter 7, we take the maximum value of this spatial variation,  $y = 0$ , as the size of the step potential  $U_0$  introduced into the MEM system.

The electron beam in MEM will typically vary in incident energy  $\epsilon$ . For the system in chapter 7, the  $10\ \mu\text{m}$  long step potential is placed with the far edge  $0.2\ \text{nm}$  before the classical turning point for  $\epsilon = 20\ \text{keV}$ . When keeping the perturbation in the same spot on the  $z$  axis, varying the incident energy  $\epsilon$  by  $\pm 10\ \text{eV}$  changes the phase sensitivity by less than 1%. Thus the phase sensitivity prediction of chapter 7 remains valid in the presence of a typical incident energy spread.

Phase contrast imaging of an optical field typically requires that the spatial coherence or coherence width of the electron beam is comparable to, or larger than, the spatial variation of the Ponderomotive potential (Spence, 2003). For light of wavelength  $532\ \text{nm}$ , a Ponderomotive potential that is proportional to  $\cos^2(k_L y)$  has peaks that are  $266\ \text{nm}$  apart. This is several times larger than a typical coherence width of  $50\ \text{nm}$  (Altman, 2010), so successful phase contrast imaging of this optical field is questionable. However, since the returning phase is proportional to  $\cos^2(k_L y)$ , over a spatial distance of  $50\ \text{nm}$  it continuously varies between 5 – 30 % of the maximum, depending on the region imaged, which may be sufficient to produce a phase contrast image of part of the Ponderomotive potential. It is also possible to reduce the scale of the spatial variations, e.g. by directing the counter propagating light beams at an angle, rather than directing them anti-parallel. This would produce a more complex interference pattern but one that varies on a length scale smaller than the electron coherence width.

---

## Conclusions and future work

The central aim of this thesis was to develop an improved understanding of image contrast in MEM and LEEM, addressing both the forward problem of how surface features and properties create image contrast, and the inverse problem of how we may use this understanding to recover information on the specimen from experimental images.

We have developed a comprehensive model of MEM image contrast, using Laplacian imaging theory for small and/or slowly varying surface features, and using caustic imaging theory for strongly scattering surfaces. Both methods enable the quantitative recovery of surface topography from experimental images.

We have developed a wave optical treatment of LEEM, which uses a complex transfer function and accounts for the aberrations of the LEEM system. Along with the work of Pang et al. (2009), this method has recently been extended by Schramm et al. (2010) to include higher order aberrations. We have applied phase retrieval techniques to simulated LEEM images, to demonstrate that phase and/or amplitude retrieval of the electron wave is both possible and beneficial.

We have returned to MEM to consider a wave optical description of MEM image contrast, examining the behaviour of the electron wave in the immersion lens, and observing the phase variation that occurs in the turn around region. Finally, we have considered the application of MEM beyond the study of surfaces, to the imaging of weak potentials such as that created by a light field.

As briefly discussed in section 1.5 and chapter 5, wave optical methods and phase–amplitude retrieval rely on connecting the electron wave function

with surface features and topography. The better the understanding of this connection, the more accurate both the forward and inverse problems of wave optical methods will be. Thus as wave optical models are applied to increasingly complex specimens, and in developing a general and complete wave optical treatment of MEM, it is likely that this connection will need to be investigated rigorously. The ray trajectory method of chapter 3 may prove useful in this study for MEM and PEEM. For example, each trajectory may be given the same initial phase, and then by integrating along each distinct path and accounting for the phase changes associated with caustics, a phase difference between ray trajectories will accumulate. This would produce an estimate of the electron wave function's phase across a plane parallel to the cathode surface, opening up the direct application of transfer function theory.

Additional future work building upon this thesis includes incorporating objective lens aberrations into the caustic imaging theory, and developing a fully wave optical MEM model, including one that is applicable well away from the cathode to image weak light field potentials. Phase and/or amplitude retrieval methods could and should be applied to experimental LEEM images from the new generation of aberration corrected instruments to extract high resolution structural information.

Finally, the methods and techniques developed here are directly applicable to the investigation and understanding of PEEM image contrast.

---

## Bibliography

- Abramowitz M and Stegun I A (1964). *Handbook of mathematical functions with formulas, graphs, and mathematical tables, second printing*. Ch. 17, pages 446–449, 589–592, Washington: United States Department of Commerce and National Bureau of Standards (also available online).
- Allen L J and Oxley M P (2001). Phase retrieval from series of images obtained by defocus variation. *Opt. Commun.* **199**, 65–75, doi:10.1016/S0030-4018(01)01556-5.
- Allen L J, Oxley M P and Paganin D M (2001). Computational aberration correction for an arbitrary linear imaging system. *Phys. Rev. Lett.* **87**, 123902, doi:10.1103/PhysRevLett.87.123902.
- Allman B E, Klein A G, Nugent K A and Opat G I (1993). Lloyd's mirage: A variant of Lloyd's mirror. *Eur. J. Phys.* **14**, 272–276, doi:10.1088/0143-0807/14/6/008.
- Altman M S (2005). Low energy electron microscopy of quantum well resonances in Ag films on W(110). *J. Phys.: Condens. Matter* **17**, S1305, doi:10.1088/0953-8984/17/16/001.
- Altman M S (2010). Trends in low energy electron microscopy. *J. Phys.: Condens. Matter* **22**, 084017, doi:10.1088/0953-8984/22/8/084017.
- Altman M S, Cai Q, Chung W F, Luo E Z, Pinkvos H and Bauer E (1995). Role of surface steps in thin film growth and properties studied by LEEM. In B Demczyk, E Garfunkel, B Clemens, E Williams and J Cuomo, editors, *Evolution of thin-film and surface structure and morphology*, volume 355, page 235. Pittsburgh, PA: Mat. Res. Soc. Symp. Proc.
- Altman M S, Chung W F, He Z Q, Poon H C and Tong S Y (2001). Quantum size effect in low energy electron diffraction of thin films. *Appl. Surf. Sci.* **169–170**, 82–87, doi:10.1016/S0169-4332(00)00644-9.
- Altman M S, Chung W F and Liu C H (1998). LEEM phase contrast. *Surf. Rev. Lett.* **5**, 1129–1141, doi:10.1142/S0218625X98001468.
- Arnol'd V I (1999). Catastrophe theory. In V I Arnol'd, V S Afrajmovich, Y S Il'yashenko, L P Shil'nikov and N Kazarinoff, editors, *Bifurcations and catastrophe theory*, chapter 2. Berlin: Springer-Verlag.
- Bajt S, Barty A, Nugent K A, McCartney M, Wall M and Paganin D (2000). Quantitative phase-sensitive imaging in a transmission electron microscope. *Ultramicroscopy* **83**, 67–73, doi:10.1016/S0304-3991(99)00174-6.
- Bales G S and Zangwill A (1990). Morphological instability of a ter-

- race edge during step-flow growth. *Phys. Rev. B* **41**, 5500–5508, doi:10.1103/PhysRevB.41.5500.
- Barnett M E and Nixon W C (1967a). Electrical contrast in mirror electron microscopy. *Optik* **26**, 310–325.
- Barnett M E and Nixon W C (1967b). A mirror electron microscope using magnetic lenses. *J. Sci. Instrum.* **44**, 893–897, doi:10.1088/0950-7671/44/11/302.
- Barrett N, Zagonel L F, Renault O and Bailly A (2009). Spatially resolved, energy-filtered imaging of core level and valence band photoemission of highly p and n doped silicon patterns. *J. Phys.: Condens. Matter* **21**, 314015, doi:10.1088/0953-8984/21/31/314015.
- Bartelt N C, Tromp R M and Williams E D (1994). Step capillary waves and equilibrium island shapes on Si(001). *Phys. Rev. Lett.* **73**, 1656–1659, doi:10.1103/PhysRevLett.73.1656.
- Batelaan H (2007). Illuminating the Kaptiza-Dirac effect with electron matter optics. *Rev. Mod. Phys.* **79**, 929–941, doi:10.1103/RevModPhys.79.929.
- Batson P E, Dellby N and Krivanek O L (2002). Sub-ångstrom resolution using aberration corrected electron optics. *Nature* **418**, 617–620, doi:10.1038/nature00972.
- Bauer E (1962). Low energy electron reflection microscopy. In S S Breese Jr, editor, *Fifth international congress for electron microscopy*, volume 1, pages D–11. New York: Academic Press.
- Bauer E (1985). The resolution of the low energy electron reflection microscope. *Ultramicroscopy* **17**, 51–56, doi:10.1016/0304-3991(85)90176-7.
- Bauer E (1991). Low-energy electron microscopy of surface processes. *Appl. Surf. Sci.* **60–61**, 350–358, doi:10.1016/0169-4332(92)90443-2.
- Bauer E (1994). Low energy electron microscopy. *Rep. Prog. Phys.* **57**, 895–938, doi:10.1088/0034-4885/57/9/002.
- Bauer E (1998). LEEM basics. *Surf. Rev. Lett.* **5**, 1275–1286, doi:10.1142/S0218625X98001614.
- Bauer E (2007). LEEM and SPLEEM. In P W Hawkes and J C H Spence, editors, *Science of microscopy*, volume I, pages 605–656. New York: Springer doi:10.1007/978-0-387-49762-4\_8.
- Becker R S, Golovchenko J A, McRae E G and Swartzentruber B S (1985). Tunneling images of atomic steps on the Si(111)7 × 7 surface. *Phys. Rev. Lett.* **55**, 2028–2031, doi:10.1103/PhysRevLett.55.2028.
- Berry M V (1981). Singularities in waves and rays. In R Balian, M Kléman and J P Poirier, editors, *Physics of defects, les houches lecture series session XXXV*, pages 453–543. Amsterdam: North-Holland.
- Berry M V (1998). Much ado about nothing: Optical dislocations lines (phase singularities, zeros, vortices ...). In M S Soskin, editor, *Singular optics, SPIE*

- proceedings*, volume 3487, pages 1–5. Bellingham, WA: SPIE International Society for Optical Engineering.
- Berry M V (2006). Oriental magic mirrors and the Laplacian image. *Eur. J. Phys.* **27**, 109–118, doi:10.1088/0143-0807/27/1/012.
- Berry M V and Mount K E (1972). Semiclassical approximations in wave mechanics. *Rep. Prog. Phys.* **35**, 315–397, doi:10.1088/0034-4885/35/1/306.
- Bok A B (1978). Mirror electron microscopy theory and applications. In S Amelinckx, R Gevers and J Van Landuyt, editors, *Diffraction and imaging techniques in material science, 2nd rev. edn.*, volume 2, pages 761–788. Amsterdam: North-Holland.
- Born M and Wolf E (2006). *Principles of optics, 7th (expanded) edn.* pages 120–125, Cambridge: Cambridge University Press.
- Borwein J M and Borwein P B (1987). *Pi and the AGM, a study in analytic number theory and computational complexity.* Volume 4, pages 7–9, New York: John Wiley & Sons.
- Boudjelkha M T and Diaz J B (1972). Half space and quarter space Dirichlet problems for the partial differential equation. *Appl. Anal.* **1**, 297–324, doi:10.1080/00036817208839020.
- Bransden B H and Joachain C J (2000). *Quantum mechanics, 2nd edn.* pages 412–415, Sydney: Pearson.
- Breuer H P and Petruccione F (2001). Destruction of quantum coherence through emission of bremsstrahlung. *Phys. Rev. A* **63**, 032102, doi:10.1103/PhysRevA.63.032102.
- Bucksbaum P H, Schumacher D W and Bashkansky M (1988). High-intensity Kapitza-Dirac effect. *Phys. Rev. Lett.* **61**, 1182–1185, doi:10.1103/PhysRevLett.61.1182.
- Chelaru L I and Meyer zu Heringdorf F J (2007). In situ monitoring of surface plasmons in single-crystalline Ag-nanowires. *Surf. Sci.* **601**, 4541–4545, doi:10.1016/j.susc.2007.04.146.
- Chen K M, Jesson D E, Pennycook S J, Mostoller M, Kaplan T, Thundat T and Warmack R M (1995). Step instabilities: A new kinetic route to 3D growth. *Phys. Rev. Lett.* **75**, 1582–1585, doi:10.1103/PhysRevLett.75.1582.
- Chung W F and Altman M S (1998). Step contrast in low energy electron microscopy. *Ultramicroscopy* **74**, 237–246, doi:10.1016/S0304-3991(98)00043-6.
- Chung W F, Feng Y J, Poon H C, Chan C T, Tong S Y and Altman M S (2003). Layer spacings in coherently strained epitaxial metal films. *Phys. Rev. Lett.* **90**, 216105, doi:10.1103/PhysRevLett.90.216105.
- Cowley J M (1986). Principles of image formation. In D C Joy, A D Romig Jr and J I Goldstein, editors, *Principles of analytical electron microscopy*, page 98. New York: Plenum Press.

- Cowley J M (1995). *Diffraction physics, 3rd rev. edn.* pages 26–35, 59–63, Amsterdam: North-Holland.
- Davydov A S (1976). *Quantum mechanics, 2nd edn.* pages 76–77, 113–114, Oxford: Pergamon Press.
- de la Figuera J, Puerta J M, Cerda J I, El Gabaly F and McCarty K F (2006). Determining the structure of Ru(0001) from low-energy electron diffraction of a single terrace. *Surf. Sci.* **600**, L105–L109, doi:10.1016/j.susc.2006.02.027.
- Duden T and Bauer E (1998). Spin-polarized low energy electron microscopy of ferromagnetic layers. *J. Electron Microsc.* **47**, 379–385.
- Dupuy J C, Sibai A and Vilotitch B (1984). Mirror electron microscopy (MEM): Work function and imaging of an electron beam biased junction of silicon (100). *Surf. Sci.* **147**, 191–202, doi:10.1016/0039-6028(84)90175-4.
- Dyukov V G, Nepijko S A and Sedov N N (1991). *Electron microscopy of local potentials.* pages 10–12, 28–35, 45–51, 63–66, 73–76, Kiev: Naukova Dumka (in Russian).
- Edgar A (1995). Reflection of wave packets from a quantum well with a tunnelling transmission resonance. *Am. J. Phys.* **63**, 136–141, doi:10.1119/1.17970.
- Eisebitt S, Lüning J, Schlotter W F, Lörngen M, Hellwig O, Eberhardt W and Stöhr J (2004). Lensless imaging of magnetic nanostructures by X-ray spectro-holography. *Nature* **432**, 885–888, doi:10.1038/nature03139.
- Faulkner H M L and Rodenburg J M (2004). Movable aperture lensless transmission microscopy: a novel phase retrieval algorithm. *Phys. Rev. Lett.* **93**, 023903, doi:10.1103/PhysRevLett.93.023903.
- Fejes P L (1977). Approximations for the calculation of high-resolution electron-microscope images of thin films. *Acta Cryst.* **A33**, 109–113, doi:10.1107/S0567739477000230.
- Feng S and Winful H G (2001). Physical origin of the Gouy phase shift. *Opt. Lett.* **26**, 485–487, doi:10.1364/OL.26.000485.
- Finazzi M, Brambilla A, Biagioni P, Graf J, Gweon G H, Scholl A, Lanzara A and Duò L (2006). Interface coupling transition in a thin epitaxial antiferromagnetic film interacting with a ferromagnetic substrate. *Phys. Rev. Lett.* **97**, 097202, doi:10.1103/PhysRevLett.97.097202.
- Fink R, Weiss M R, Umbach E, Preikszas D, Rose H, Spehr R, Hartel P, Engel W, Degenhardt R, Wichtendahl R, Kuhlenbeck H, Erlebach W, Ihmann K, Schlögl R, Freund H J, Bradshaw A M, Lilienkamp G, Schmidt T, Bauer E and Benner G (1997). SMART: a planned ultrahigh-resolution spectro-microscope for BESSY II. *J. Elect. Spectrosc. Relat. Phenom.* **84**, 231–250, doi:10.1016/S0368-2048(97)00016-9.
- Flügge S (1971). *Practical quantum mechanics.* pages 105–107, Berlin: Springer-Verlag.

- Freimund D L, Aflatooni K and Batelaan H (2001). Observation of the Kapitza-Dirac effect. *Nature* **413**, 142–143, doi:10.1038/35093065.
- Freimund D L and Batelaan H (2002). Bragg scattering of free electron using the Kapitza-Dirac effect. *Phys. Rev. Lett.* **89**, 283602, doi:10.1103/PhysRevLett.89.283602.
- Freimund D L, Batelaan H, Smirnova O and Ivanov M (2004). Kapitza-Dirac diffraction without standing waves: diffraction without a grating? *Phys. Rev. Lett.* **92**, 223601, doi:10.1103/PhysRevLett.92.223601.
- Friedrich H and Trost J (1996a). Nonintegral Maslov indices. *Phys. Rev. A* **54**, 1136–1145, doi:10.1103/PhysRevA.54.1136.
- Friedrich H and Trost J (1996b). Phase loss in WKB due to reflection by a potential. *Phys. Rev. Lett.* **76**, 4869–4873, doi:10.1103/PhysRevLett.76.4869.
- Frisch T and Verga A (2006). Effect of step stiffness and diffusion anisotropy on the meandering of a growing vicinal surface. *Phys. Rev. Lett.* **96**, 166104, doi:10.1103/PhysRevLett.96.166104.
- Gerchberg R W and Saxton W O (1972). A practical algorithm for the determination of the phase from image and diffraction plane pictures. *Optik* **35**, 237–246.
- Godehardt R (1995). Mirror electron microscopy. *Adv. Imag. Elect. Phys.* **94**, 81–150, doi:10.1016/S1076-5670(08)70144-7.
- Goodman J W (2005). *Introduction to Fourier optics, 3rd edn.* Greenwood Village, Colorado: Roberts & Company Publishers.
- Gouy L G (1890). Sur une propriété nouvelle des ondes lumineuses. *Acad. Sci. Comptes Rendus* **110**, 1251–1253.
- Grant I S and Phillips W R (1990). *Electromagnetism, 2nd edn.* pages 100–103, Chichester: John Wiley & Sons.
- Greenberger D M (1988). A new non-local effect in quantum mechanics. *Physica B* **151**, 374–377.
- Greenhow R C and Matthew J A D (1992). Continuum computer solutions of the Schrödinger equation. *Am. J. Phys.* **60**, 655–663, doi:10.1119/1.17121.
- Griffith O H and Engel W (1991). Historical perspective and current trends in emission microscopy, mirror electron microscopy and low-energy electron microscopy. *Ultramicroscopy* **36**, 1–28, doi:10.1016/0304-3991(91)90135-S.
- Griffiths D J (1995). *Introduction to quantum mechanics.* Ch. 8, Upper Saddle River NJ: Prentice Hall.
- Günther S, Kaulich B, Gregoratti L and Kiskinova M (2002). Photoelectron microscopy and applications in surface and materials science. *Prog. Surf. Sci.* **70**, 187–260, doi:10.1016/S0079-6816(02)00007-2.
- Gureyev T E and Nugent K A (1997). Rapid quantitative phase imaging using the transport of intensity equation. *Opt. Commun.* **133**, 339–346, doi:10.1016/S0030-4018(96)00454-3.

- Gureyev T E, Pogany A, Paganin D M and Wilkins S W (2004). Linear algorithms for phase retrieval in the Fresnel region. *Opt. Commun.* **231**, 53–70, doi:10.1016/j.optcom.2003.12.020.
- Hackermüller L, Hornberger K, Brezger B, Zeilinger A and Arndt M (2004). Decoherence of matter waves by thermal emission of radiation. *Nature* **427**, 711–714, doi:10.1038/nature02276.
- Halliday D, Resnick R and Walker J (1997). *Fundamentals of physics, 5th edn.* pages 912–913, New York: John Wiley & Sons.
- Hannon J B, Meyer zu Heringdorf F J, Tersoff J and Tromp R M (2001). Phase coexistence during surface phase transitions. *Phys. Rev. Lett.* **86**, 4871–4874, doi:10.1103/PhysRevLett.86.4871.
- Hannon J B, Sun J, Pohl K and Kellogg G L (2006). Origins of nanoscale heterogeneity in ultrathin films. *Phys. Rev. Lett.* **96**, 246103, doi:10.1103/PhysRevLett.96.246103.
- Hariharan P and Robinson P A (1996). The Gouy phase shift as a geometrical quantum effect. *J. Mod. Opt.* **43**, 219–221, doi:10.1080/09500349608232735.
- Hartel P, Preikszas D, Spehra R, Müller H and Rose H (2003). Mirror corrector for low-voltage electron microscopes. *Adv. Imag. Elect. Phys.* **120**, 41–133, doi:10.1016/S1076-5670(02)80034-9.
- Hawkes P W and Kasper E (1994). *Principles of Electron Optics*, volume 2. pages 882–886, London: Academic Press.
- Hecht E (1998). *Optics, 3rd edn.* pages 397–399, Reading MA: Addison-Wesley Longman.
- Hecht F, Pironneau O, Hyaric A L and Morice J (accessed June 2010). FreeFem++ version 3.9-0, available from <http://www.freefem.org/ff++/>.
- Hermans A J and Petterson J A (1970). A quantum mechanical treatment of the mirror electron microscope. *J. Eng. Math.* **4**, 141–154, doi:10.1007/BF01535086.
- Herring C and Nichols M H (1949). Thermionic emission. *Rev. Mod. Phys.* **21**, 185–270, doi:10.1103/RevModPhys.21.185.
- Hibino H and Watanabe Y (2005). Growth of twinned epitaxial layers on Si(111)  $\sqrt{3} \times \sqrt{3}$ -B studied by low-energy electron microscopy. *Jpn. J. Appl. Phys.* **44**, 358–364, doi:10.1143/JJAP.44.358.
- Hilner E, Zakharov A A, Schulte K, Kratzer P, Andersen J N, Lundgren E and Mikkelsen A (2009). Ordering of the nanoscale step morphology as a mechanism for droplet self-propulsion. *Nano Lett.* **9**, 2710–2714, doi:10.1021/nl9011886.
- Hirschfelder J O, Christoph A C and Palke W E (1974). Quantum mechanical streamlines. I. Square potential barrier. *J. Chem. Phys.* **61**, 5435–5455, doi:10.1063/1.1681899.

- Jackson J D (1999). *Classical electrodynamics, 3rd edn.* pages 34–35, 111–112, New York: John Wiley & Sons.
- Jesson D E, Pavlov K M, Morgan M J and Usher B F (2007). Imaging surface topography using Lloyd's mirror in photoemission electron microscopy. *Phys. Rev. Lett.* **99**, 016103, doi:10.1103/PhysRevLett.99.016103.
- Kan H C and Phaneuf R J (2001). Focusing of low energy electrons by submicrometer patterned structures in low energy electron microscopy. *J. Vac. Sci. Technol. B* **19**, 1158–1163, doi:10.1116/1.1385688.
- Kapitza P L and Dirac P A (1933). The reflection of electrons from standing light waves. *Proc. Cam. Phil. Soc.* **29**, 297–300, doi:10.1017/S0305004100011105.
- Kellogg G L and Bartelt N C (2005). Surface-diffusion-limited island decay on Rh(001). *Surf. Sci.* **577**, 151–157, doi:10.1016/j.susc.2005.01.003.
- Kennedy S M, Jesson D E, Morgan M J, Smith A E and Barker P F (2006). Phase sensitivity of slow electrons to interactions with weak potentials. *Phys. Rev. A* **74**, 044701, doi:10.1103/PhysRevA.74.044701.
- Kennedy S M, Paganin D M and Jesson D E (2008). Transition between short and long wavelength limits in quantum mechanical reflection from a linear potential. *Am. J. Phys.* **76**, 158–162, doi:10.1119/1.2805240.
- Kennedy S M, Schofield N E, Paganin D M and Jesson D E (2009). Wave optical treatment of surface step contrast in low energy electron microscopy. *Surf. Rev. Lett.* **16**, 855–867, doi:10.1142/S0218625X09013402.
- Kennedy S M, Zheng C X, Tang W X, Paganin D M and Jesson D E (2010). Laplacian image contrast in mirror electron microscopy. *Proc. R. Soc. A* **466**, 2857–2874, doi:10.1098/rspa.2010.0093 and *ibid.* Addendum, submitted in 2010.
- Kennedy S M, Zheng C X, Tang W X, Paganin D M and Jesson D E (2011). Caustic imaging of gallium droplets using mirror electron microscopy. *Ultramicroscopy* **111**, 356–363, doi:10.1016/j.ultramic.2011.01.019.
- Ko Y U and Joy D C (2002). Simulation of imaging in projection microscope using multi-beam probes. *Proc. SPIE* **4689**, 565–575, doi:10.1117/12.473497.
- Könenkamp R, Jones T, Elstner J, Word R, Rempfer G, Dixon T, Almaraz L and Skoczylas W (2008). Image properties in an aberration-corrected photoemission electron microscope. *Phys. Procedia* **1**, 505–511, doi:10.1016/j.phpro.2008.07.132.
- Krömker B, Escher M, Funnemann D, Hartung D, Engelhard H and Kirschner J (2008). Development of a momentum microscope for time resolved band structure imaging. *Rev. Sci. Instrum.* **79**, 053702, doi:10.1063/1.2918133.
- Landau L D and Lifshitz E M (1977). *Quantum mechanics: non-relativistic theory, 3rd edn.* pages 51–52, Oxford: Pergamon Press.

- Lévy-Leblond J M (1987). A geometrical quantum phase effect. *Phys. Lett. A* **125**, 441–442, doi:10.1016/0375-9601(87)90180-0.
- Lewis Jr H R (1966). Computation of electrostatic and rapidly pulsed magnetic fields. *J. Appl. Phys.* **37**, 2541–2550, doi:10.1063/1.1782081.
- Li X, Zhang J, Xu Z, Fu P, Guo D S and Freeman R R (2004). Theory of the Kapitza-Dirac diffraction effect. *Phys. Rev. Lett.* **92**, 233603, doi:10.1103/PhysRevLett.92.233603.
- Linfoot E H and Wolf E (1956). Phase distribution near focus in an aberration-free diffraction image. *Proc. Phys. Soc. London B* **69**, 823–832, doi:10.1088/0370-1301/69/8/307.
- Luk'yanov A E, Spivak G V and Gvozdover R S (1974). Mirror electron microscopy. *Sov. Phys. Usp.* **16**, 529–552, doi:10.1070/PU1974v016n04ABEH005299.
- Lynch D F, Moodie A F and O'Keefe M A (1975). n-beam lattice images. V. The use of the charge-density approximation in the interpretation of lattice images. *Acta Cryst.* **A31**, 300–307, doi:10.1107/S0567739475000642.
- Maitra N T and Heller E J (1997). Barrier tunnelling and reflection in the time and energy domains: The battle of the exponentials. *Phys. Rev. Lett.* **78**, 3035–3038, doi:10.1103/PhysRevLett.78.3035.
- Man K L, Feng Y J, Chan C T and Altman M S (2007a). Vibrational entropy-driven dealloying of Mo(100) and W(100) surface alloys. *Surf. Sci.* **601**, L95–L101, doi:10.1016/j.susc.2007.06.027.
- Man K L, Guo Q L and Altman M S (2006). Growth and oxidation of Cr films on the W(100) surface. *Surf. Sci.* **600**, 1060–1070, doi:10.1016/j.susc.2005.12.030.
- Man K L, Pang A B and Altman M S (2007b). Kinetic length and step permeability on the Si(111)(1×1) surface. *Surf. Sci.* **601**, 4669–4674, doi:10.1016/j.susc.2007.05.039.
- Man K L, Qiu Z Q and Altman M S (2004). Kinetic limitations in electronic growth of Ag films on Fe(100). *Phys. Rev. Lett.* **93**, 236104, doi:10.1103/PhysRevLett.93.236104.
- Marcuse D (1976). Elementary derivation of the phase shift at a caustic. *Appl. Opt.* **15**, 2949–2950, doi:10.1364/AO.15.002949.
- Massies J, Etienne P, Dezaly F and Linh N T (1980). Stoichiometry effects on surface properties of GaAs{100} grown in situ by MBE. *Surf. Sci.* **99**, 121–131, doi:10.1016/0039-6028(80)90582-8.
- McCarty K F, Nobel J A and Bartelt N C (2001). Vacancies in solids and the stability of surface morphology. *Nature* **412**, 622–625, doi:10.1038/35088026.
- Messiah A (1999). *Quantum mechanics*. pages 234–239, Mineola: Dover.
- Meyer R R, Sloan J, Dunin-Borkowski R E, Kirkland A I, Novotny M C, Bailey S R, Hutchison J L and Green M L H (2000). Discrete atom imaging of

- one-dimensional crystals formed within single-walled carbon nanotubes. *Science* **289**, 1324–1326, doi:10.1126/science.289.5483.1324.
- Meyer zu Heringdorf F and Buckanie N (2010). Nonlinear photoemission microscopy with surface plasmon polaritons. *Microsc. Microanal.* **16**, 502–503, doi:10.1017/S1431927610057557.
- Miao J, Charalambous P, Kirz J and Sayre D (1999). Extending the methodology of X-ray crystallography to allow imaging of micrometre-sized non-crystalline specimens. *Nature* **400**, 342–344, doi:10.1038/22498.
- Misell D L (1973). An examination of an iterative method for the solution of the phase problem in optics and electron optics: I. Test calculations. *J. Phys. D* **6**, 2200–2216, doi:10.1088/0022-3727/6/18/305.
- Morin C, Hitchcock A P, Cornelius R M, Brash J L, Urquhart S G, Scholl A and Doran A (2004). Selective adsorption of protein on polymer surfaces studied by soft X-ray photoemission electron microscopy. *J. Electron Spectrosc.* **137–140**, 785–794, doi:10.1016/j.elspec.2004.02.158.
- Nepijko S A, Gloskovskii A, Sedov N N and Schönhense G (2003). Measurement of the electric field distribution and potentials on the object surface in an emission electron microscope without restriction of the electron beams. *J. Microsc.* **211**, 89–94, doi:10.1046/j.1365-2818.2003.01199.x.
- Nepijko S A, Marx G K L and Schönhense G (2007). Quantitative determination of magnetic fields on object surfaces via photoemission electron microscopy without restriction of the electron beam. *Nucl. Instr. and Meth. in Phys. Res. B* **264**, 194–200, doi:10.1016/j.nimb.2007.08.076.
- Nepijko S A and Schönhense G (2010). Measurement of potential distribution function on object surface by using an electron microscope in the mirror operation mode. *J. Microsc.* **238**, 90–94, doi:10.1111/j.1365-2818.2009.03340.x.
- Nepijko S A and Sedov N N (1997). Aspects of mirror electron microscopy. *Adv. Imag. Elect. Phys.* **102**, 273–323, doi:10.1016/S1076-5670(08)70125-3.
- Nepijko S A, Sedov N N, Schmidt O, Schönhense G, Bao X and Huang W (2001a). Imaging of three-dimensional objects in emission electron microscopy. *J. Microsc.* **202**, 480–487, doi:10.1046/j.1365-2818.2001.00846.x.
- Nepijko S A, Sedov N N and Schönhense G (2001b). Peculiarities of imaging one- and two-dimensional structures using an electron microscope in the mirror operation mode. *J. Microsc.* **203**, 269–276, doi:10.1046/j.1365-2818.2001.00895.x.
- Nepijko S A, Sedov N N, Schönhense G, Escher M, Bao X and Huang W (2000). Resolution determination in emission electron microscopy due to object roughness. *Ann. Phys. (Leipzig)* **9**, 441–451, doi:10.1002/1521-3889(200006)9:6<441::AID-ANDP441>3.0.CO;2-J.
- Nye J F (1999). *Natural focusing and fine structure of light: caustics and wave*

- dislocations*. pages 9–11, 46–48, Bristol: Institute of Physics Publishing.
- Op de Beeck M, Dyck D V and Coene W (1996). Wave function reconstruction in HRTEM: the parabola method. *Ultramicroscopy* **64**, 167–183, doi:10.1016/0304-3991(96)00058-7.
- Paganin D M (2006). *Coherent X-ray optics*. pages 278–284, 295–301, 395–396, New York: Oxford University Press.
- Paganin D M and Gureyev T E (2008). Phase contrast, phase retrieval and aberration balancing in shift-invariant linear imaging systems. *Opt. Commun.* **281**, 965–981, doi:10.1016/j.optcom.2007.10.097.
- Paganin D M and Nugent K A (1998). Noninterferometric phase imaging with partially coherent light. *Phys. Rev. Lett.* **80**, 2586–2589, doi:10.1103/PhysRevLett.80.2586.
- Pang A B, Müller T, Altman M S and Bauer E (2009). Fourier optics of image formation in LEEM. *J. Phys.: Condens. Matter* **21**, 314006, doi:10.1088/0953-8984/21/31/314006.
- Phaneuf R J and Schmid A K (2003). Low-energy electron microscopy: imaging surface dynamics. *Phys. Today* **March**, 50–55, doi:10.1063/1.1570772.
- Plass R, Last J A, Bartelt N C and Kellogg G L (2001). Nanostructures: Self-assembled domain patterns. *Nature* **412**, 875, doi:10.1038/35091143.
- Polozhiy G N (1967). *Equations of mathematical physics*. pages 62–64, 149, New York: Hayden Book Company.
- Poppa H, Tober E D and Schmid A K (2002). In situ observation of magnetic domain pattern evolution in applied fields by spin-polarized low energy electron microscopy. *J. Appl. Phys.* **91**, 6932–6934, doi:10.1063/1.1449435.
- Press W H, Teukolsky S A, Vetterling W T and Flannery B P (2007). *Numerical recipes, the art of scientific computing, 3rd edn*. pages 229–232, 600–604, 907–910, Cambridge: Cambridge University Press.
- Reimer L and Kohl H (2008). *Transmission electron microscopy, 5th edn*. Berlin: Springer-Verlag.
- Rempfer G F (1992). Methods of calculating resolution in electron microscopy: Scherzer's equation, circles of least confusion and the intensity distribution approach. *Ultramicroscopy* **47**, 241–255, doi:10.1016/0304-3991(92)90200-4.
- Rempfer G F, Desloge D M, Skoczylas W P and Griffith O H (1997). Simultaneous correction of spherical and chromatic aberrations with an electron mirror: an electron optical achromat. *Microsc. Microanal.* **3**, 14–27, doi:10.1017.S143192769797001X.
- Rempfer G F and Griffith O H (1992). Emission microscopy and related techniques: resolution in photoelectron microscopy, low energy electron microscopy and mirror electron microscopy. *Ultramicroscopy* **47**, 35–54, doi:10.1016/0304-3991(92)90184-L.

- Riesz F (2000). Geometrical optical model of the image formation in Makyoh (magic-mirror) topography. *J. Phys. D: Appl. Phys.* **33**, 3033–3040, doi:10.1088/0022-3727/33/23/305.
- Rockenberger J, Nolting F, Lüning J, Hu J and Alivisatos A P (2002). Soft X-ray imaging and spectroscopy of single nanocrystals. *J. Chem. Phys.* **116**, 6322–6328, doi:10.1063/1.1460856.
- Rodenburg J M, Hurst A C, Cullis A G, Dobson B R, Pfeiffer F, Bunk O, David C, Jefimovs K and Johnson I (2007). Hard-X-ray lensless imaging of extended objects. *Phys. Rev. Lett.* **98**, 034801, doi:10.1103/PhysRevLett.98.034801.
- Römer H (2005). *Theoretical optics*. pages 72, 156–158, Weinheim: Wiley-VCH.
- Rose H and Preikszas D (1992). Outline of a versatile corrected LEEM. *Optik* **92**, 31–44.
- Ross F M, Tromp R M and Reuter M C (1999). Transition states between pyramids and domes during Ge/Si island growth. *Science* **286**, 1931–1934, doi:10.1126/science.286.5446.1931.
- Rougemaille N and Schmid A K (2010). Magnetic imaging with spin-polarized low energy electron microscopy. *Eur. Phys. J. Appl. Phys.* **50**, 20101, doi:10.1051/epjap/2010048.
- Rubinowicz A (1938). On the anomalous propagation of phase in the focus. *Phys. Rev.* **54**, 931–936, doi:10.1103/PhysRev.54.931.
- Sadowski J T, Sazaki G, Nishikata S, Al-Mahboob A, Fujikawa Y, Nakajima K, Tromp R M and Sakurai T (2007). Single-nucleus polycrystallization in thin film epitaxial growth. *Phys. Rev. Lett.* **98**, 046104, doi:10.1103/PhysRevLett.98.046104.
- Sakurai J J (1994). *Modern quantum mechanics, revised edn.* pages 103–105, Reading MA: Addison-Wesley.
- Scherzer O (1947). Sphärische und chromatische korrektur von elektronenlinsen. *Optik* **2**, 114–132.
- Scherzer O (1948). The theoretical resolution limit of the electron microscope. *J. Appl. Phys.* **20**, 20–29, doi:10.1063/1.1698233.
- Schmidt T, Groh U, Fink R, Umbach E, Schaff O, Engel W, Richter B, Kuhlbeck H, Schlögl R, Freund H J, Bradshaw A M, Preikszas D, Hartel P, Spehr R, Rose H, Lilienkamp G, Bauer E and Benner G (2002). XPEEM with energy-filtering: advantages and first results from the SMART project. *Surf. Rev. Lett.* **9**, 223–232, doi:10.1142/S0218625X02001811.
- Schmidt T, Marchetto H, Lévesque P L, Groh U, Maier F, Preikszas D, Hartel P, Spehr R, Lilienkamp G, Engel W, Fink R, Bauer E, Rose H, Umbach E and Freund H J (2010). Double aberration correction in a low-energy electron microscope. *Ultramicroscopy* **110**, 1358–1361, doi:10.1016/j.ultramic.2010.07.007.

- Schönecker G, Spehr R and Rose H (1990). Fast charge-simulation procedure for planar and simple three-dimensional electrostatic fields. *Nucl. Instr. and Meth. A* **298**, 360–376, doi:10.1016/0168-9002(90)90638-M.
- Schönhense G and Spiecker H (2002). Correction of chromatic and spherical aberration in electron microscopy utilizing the time structure of pulsed excitation sources. *J. Vac. Sci. Technol. B* **20**, 2526–2535, doi:10.1116/1.1523373.
- Schramm S, Tromp R M, Pang A B and Altman M S (2010). to be published.
- Schrödinger E (1926). An undulatory theory of the mechanics of atoms and molecules. *Phys. Rev.* **28**, 1049–1070, doi:10.1103/PhysRev.28.1049.
- Sedov N N (1970). Théorie quantitative des systèmes en microscopie électronique à balayage, à miroir et à émission. *J. Microsc.-Paris* **9**, 1–26.
- Shao Z and Crewe A V (1989). On the resolution of the low-energy electron reflection microscope. *Ultramicroscopy* **31**, 199–204, doi:10.1016/0304-3991(89)90214-3.
- Shimakura T, Takahashi Y, Sugaya M, Ohnishi T, Hasegawa M and Ohta H (2008). Mirror electron microscope for inspecting nanometer-sized defects in magnetic media. *Microelectron. Eng.* **85**, 1811–1814, doi:10.1016/j.mee.2008.05.018.
- Slezák J, Ondřejček M, Chvoj Z, Cháb V, Conrad H, Heun S, Schmidt T, Ressel B and Prince K C (2000). Surface diffusion of Au on Si(111): a microscopic study. *Phys. Rev. B* **61**, 16121–16128, doi:10.1103/PhysRevB.61.16121.
- Smith A D, Schofield P F, Scholl A, Patrick R A D and Bridges J C (2003). XPEEM valence state imaging of mineral-intergrowths with a spatial resolution of 100nm. *J. Phys. IV* **104**, 373–376.
- Someya T and Kobayashi J (1974). Quantitative application of electron-mirror microscopy to the determination of pure shear of ferroelectric  $\text{Gd}_2(\text{MoO}_4)_3$ . *Phys. Stat. Sol. (a)* **26**, 325–336, doi:10.1002/pssa.2210260134.
- Sonnentag P and Hasselbach F (2005). Decoherence of electron waves due to induced charges moving through a nearby resistive material. *Braz. J. Phys.* **35**, 385–390.
- Speake C C and Trenkel C (2003). Forces between conducting surfaces due to spatial variations of surface potential. *Phys. Rev. Lett.* **90**, 160403, doi:10.1103/PhysRevLett.90.160403.
- Spence J C H (2003). *High-resolution electron microscopy, 3rd edn.* Ch. 2–4, Oxford: Oxford University Press.
- Spence J C H (2007). Diffractive (lensless) imaging. In P W Hawkes and J C H Spence, editors, *Science of microscopy*, volume IV, pages 1196–1227. New York: Springer, doi:10.1007/978-0-387-49762-4\_19.
- Stamp A P and McIntosh G C (1996). A time-dependent study of resonant tunnelling through a double barrier. *Am. J. Phys.* **64**, 264–276,

- doi:10.1119/1.18214.
- Świąch W and Bauer E (1991). The growth of Si on Si(100): a video-LEEM study. *Surf. Sci.* **255**, 219–228, doi:10.1016/0039-6028(91)90678-L.
- Świąch W, Rausenberger B, Engel W, Bradshaw A M and Zeitler E (1993). In-situ studies of heterogeneous reactions using mirror electron microscopy. *Surf. Sci.* **294**, 297–307, doi:10.1016/0039-6028(93)90116-2.
- Tanaka S, Bartelt N C, Umbach C C, Tromp R M and Blakely J M (1997). Step permeability and the relaxation of biperiodic gratings on Si(001). *Phys. Rev. Lett.* **78**, 3342–3345, doi:10.1103/PhysRevLett.78.3342.
- Tang W X, Jesson D E, Pavlov K M, Morgan M J and Usher B F (2009). Ga droplet morphology on GaAs(001) studied by Lloyd's mirror photoemission electron microscopy. *J. Phys.: Condens. Matter* **21**, 314022, doi:10.1088/0953-8984/21/31/314022.
- Tang W X, Man K L, Huang H, Woo C H and Altman M S (2002). Growth shapes of Ag crystallites on the Si(111) surface. *J. Vac. Sci. Technol. B* **20**, 2492–2495, doi:10.1116/1.1523372.
- Teague M R (1983). Deterministic phase retrieval: a Green's function solution. *J. Opt. Soc. Am.* **73**, 1434–1441, doi:10.1364/JOSA.73.001434.
- Telieps W and Bauer E (1985). An analytical reflection and emission UHV surface electron microscope. *Ultramicroscopy* **17**, 57–65, doi:10.1016/0304-3991(85)90177-9.
- Telieps W and Bauer E (1988). Low energy electron microscopy of surfaces. *Surf. Sci.* **200**, 512–513, doi:10.1016/0039-6028(88)90557-2.
- Telieps W, Mundschau M and Bauer E (1987). Dark field imaging with LEEM. *Optik* **77**, 93–97.
- Tersoff J, Jesson D E and Tang W X (2009). Running droplets of Ga from evaporation of GaAs. *Science* **324**, 236–238, doi:10.1126/science.1169546.
- Tersoff J, Jesson D E and Tang W X (2010). Decomposition controlled by surface morphology during Langmuir evaporation of GaAs. *Phys. Rev. Lett.* **105**, 035702, doi:10.1103/PhysRevLett.105.035702.
- Thayer G E, Sadowski J T, Meyer zu Heringdorf F, Sakurai T and Tromp R M (2005). Role of surface electronic structure in thin film molecular ordering. *Phys. Rev. Lett.* **95**, 256106, doi:10.1103/PhysRevLett.95.256106.
- Theis W, Bartelt N C and Tromp R M (1995). Chemical potential maps and spatial correlations in 2D-island ripening on Si(001). *Phys. Rev. Lett.* **75**, 3328–3331, doi:10.1103/PhysRevLett.75.3328.
- Toraldo Di Francia G (1955). Resolving power and information. *J. Opt. Soc. Am.* **45**, 497–499, doi:10.1364/JOSA.45.000497.
- Tromp R M and Hannon J B (2002). Thermodynamics of nucleation and growth. *Surf. Rev. Lett.* **9**, 1565–1593, doi:10.1142/S0218625X02003846.
- Tromp R M, Hannon J B, Ellis A W, Wan W, Berghaus A and Schaff O

- (2010). A new aberration-corrected, energy-filtered LEEM/PEEM instrument. I. Principles and design. *Ultramicroscopy* **110**, 852–861, doi:10.1016/j.ultramic.2010.03.005.
- Tromp R M, Mankos M, Reuter M C, Ellis A W and Copel M (1998). A new low energy electron microscope. *Surf. Rev. Lett.* **5**, 1189–1197, doi:10.1142/S0218625X98001523.
- Tromp R M and Reuter M (1991). Design of a new photo-emission/low-energy electron microscope for surface studies. *Ultramicroscopy* **36**, 99–106, doi:10.1016/0304-3991(91)90141-R.
- Tromp R M and Reuter M C (1993). Imaging with a low-energy electron microscope. *Ultramicroscopy* **50**, 171–178, doi:10.1016/0304-3991(93)90007-K.
- Turner G H and Bauer E (1966). An ultrahigh vacuum electron microscope and its application to work function studies. In R Ueda, editor, *Sixth international congress for electron microscopy, Kyoto*, volume 1, pages 163–164. Tokyo: Maruzen.
- Urban K W (2009). Is science prepared for atomic-resolution electron microscopy? *Nat. Mat.* **8**, 260–262, doi:10.1038/nmat2407.
- Veneklasen L H (1991). Design of a spectroscopic low-energy electron microscope. *Ultramicroscopy* **36**, 76–90, doi:10.1016/j.nima.2003.11.159.
- Wan W, Feng J, Padmore H A and Robin D S (2004). Simulation of a mirror corrector for PEEM3. *Nucl. Instr. and Meth. A* **519**, 222–229, doi:10.1016/j.nima.2003.11.159.
- Watanabe F, Kodambaka S, Swiech W, Greene J E and Cahill D G (2004). LEEM study of island decay on Si(110). *Surf. Sci.* **572**, 425–432, doi:10.1016/j.susc.2004.09.014.
- Wichtendahl R, Fink R, Kühlenbeck H, Preikszas D, Rose H, Spehr R, Hartel P, Engel W, Schlögl R, Freund H J, Bradshaw A, Lilienkamp G, Schmidt T, Bauer E, Brenner G and Umbach E (1998). SMART—an aberration-corrected XPEEM/LEEM with energy filter. *Surf. Rev. Lett.* **5**, 1249–1256, doi:10.1142/S0218625X98001584.
- Williams D B and Carter C B (1996). *Transmission electron microscopy*. pages 459–469, New York: Plenum Press.
- Wu Y Z, Won C, Scholl A, Doran A, Zhao H W, Jin X F and Qiu Z Q (2004). Magnetic stripe domains in coupled magnetic sandwiches. *Phys. Rev. Lett.* **93**, 117205, doi:10.1103/PhysRevLett.93.117205.
- Yasue T, Koshikawa T and Bauer E (2002). Low energy electron microscopy/diffraction study on growth of Ge on Si(113) surface. *J. Vac. Sci. Technol. B* **20**, 2496–2499, doi:10.1116/1.1523374.
- Yasue T, Koshikawa T, Jalochofski M and Bauer E (2001). Dynamic observations of the formation of thin Cu layers on clean and hydrogen-terminated Si(111) surfaces. *Surf. Sci.* **480**, 118–127, doi:10.1016/S0039-6028(01)00826-

3.

Yu R P, Kennedy S M, Paganin D M and Jesson D E (2010). Phase retrieval low energy electron microscopy. *Micron* **41**, 232–238, doi:10.1016/j.micron.2009.10.010.

Yu R P and Paganin D M (2010). Blind phase retrieval for aberrated linear shift-invariant imaging systems. *New Journal of Physics* **12**, 073040, doi:10.1088/1367-2630/12/7/073040.

Zernike F (1942). Phase contrast, a new method for the microscopic observation of transparent objects. *Physica* **9**, 686–698, doi:10.1016/S0031-8914(42)80035-X.